You'll never walk alone

When you walk through a storm
hold your head up high
And don't be afraid of the dark.
At the end of a storm is a golden sky
And the sweet silver song of a lark.

Walk on through the wind,
Walk on through the rain,
Tho' your dreams be tossed and blown.

Walk on, walk on with hope in your heart
And you'll never walk alone,
You'll never, ever walk alone.
Walk on, walk on with hope in your heart
And you'll never walk alone,
You'll never, ever walk alone.

Gerry & The Pacemakers

Acknowledgements

I would first like to express my gratitude to my supervisors, Prof. David Nicholson and Post.Doc. Karina Mathisen, for their support and guidance with the work of this thesis. Thank you both for taking the time to discuss the problems I have encountered over the last two years and for constantly reminding me that everything always works out at the end. A special thanks to Karina who I not only consider as my supervisor, but also as a good friend (although she is a Man. Utd. supporter). Your enthusiasm for science, combined with a good sense of humor and down to earth nature, are highly appreciated.

I acknowledge the Norwegian University of Science and Technology and the Norwegian Research Council for financing my stays at the Swiss-Norwegian Beamline (SNBL) at the European Synchrotron Radiation Facility (ESRF) in Grenoble, France, and at MaxLAB in Lund, Sweden.

I would also like to thank Prof. Magnus Rønning and Post.Doc Tiejun Zhao for their help with the carbon monoxide oxidation measurements. A big thanks to Syverin Lierhagen for doing the ICP-MS analysis for me and to Julian Tolchard for helping me with the Powder X-ray Diffraction experiments and BET surface area measurements. I am grateful for all the help I have gotten from Dr. Camilla Norhei in connection with the XAS analysis.

In addition, I would like to thank my fellow students Anlaug, Asimra, Katrine, Mari N., Mari T., Tina and Øyvind for their friendship and for the time we have studied together. They have made "Uni" a fun place to be, even at the end "då det brant på dass" (when we were all under a lot of stress). A special thanks to

Anlaug who studied with me in Australia last fall. I have no idea how I would have handled the problems we faced without you by my side. I am forever grateful to my dear friend and regular lunch partner Madeleine for sticking around through all the ups and downs, and for correcting misspellings, etc. in my thesis. Thanks to Helene and Alex for being the best flat mates ever, they always seem be able to cheer me up no matter how cranky I am.

My deepest gratitude goes to my parents, Turid and Trond, and my brothers, Tore and Espen, for their unflagging love and support throughout my life. Without their encouragement and positive energy it would have been impossible for me to finish this thesis. You are simply the best family one could ever wish for.

Trondheim, May 2009

Beate Valvik

List of symbols and abbreviations

Latin Symbols

A_j(k)	Total backscattering amplitude of the j^{th} coordination shell
d	Spacing of the crystal planes
d_c	Cluster size
E^0	Electrode potential
E_0	Energy threshold
F_j(k)	Backscattering amplitude from an atom in the j^{th} coordination shell
$\hbar$	Planck's constant
I_0	Incident radiation
I_t	Transmitted radiation
I_f	Fluorescence radiation
k	Full width half maximum
k^{n-1}	Weighting factor
L	Crystal size/ Å
N_j	Number of backscattered atoms in the j^{th} coordination shell (multiplicity)
$R_{A\cdots B}$	Nearest neighboring distance between the absorber (A) and the backscatter (B)/ Å
S_i(k)	Amplitude reduction factor on the absorber (i)
x	Thickness of sample
Z	Atomic mass
Å	Ångstrøm/ 10^{-10} meter

Greek Symbols

β	Line broadening/ radians
χ(E)	EXAFS fraction extracted from the XAS spectrum/ eV
χ(k)	EXAFS fraction converted to the photoelectron wave vector scale/ $Å^{-1}$
ΔH_f	Heat of formation/ $\frac{kJ}{mole}$
λ	Wavelength of X-ray/ Å
λ_e	Photoelectron wavelength/ Å
μ	Linear absorption coefficient
θ	Bragg angle of incident X-ray/ radians
σ^2	Debye- Waller factor/ $Å^2$
φ_{ij}(k)	The total phase shift experienced by the photon electron

Abbreviations

AFAC	Amplitude reduction factor
EXAFS	Extended X-ray Absorption Fine Structure
GNC	Gold nanocluster
GNP	Gold nanoparticle
Me:Z	Ion exchanged zeotypic systems
MeZ	Metal incorporated zeotypic systems
nm	Nanometer/ 10^{-9} meter
PRDF	Pseudo Radial Distribution Function
PROX	Preferential CO oxidation
PXRD	Powder X-ray Diffraction
SAPO	Silicoaluminophosphate
SEM	Scanning Electron Microscopy
SCR	Selective Catalytic Reduction
TGA	Thermogravimetric Analysis
TRP	Temperature-programmed reduction
XANES	X-ray Absorption Near Edge Spectroscopy
XAS	X-ray Absorption Spectroscopy
ZSM-5	Zeolite Socony Mobile No.5

Contents

Chapter 1

INTRODUCTION

Over the last two decades, there has been an astonishing growth of interest to supported gold catalysts since the work of Masatake Haruta *et al.* in 1987.[1,2] They discovered that small gold nanoparticles (GNPs) ($\leq$ 5 nm) supported on suitable oxides are active for carbon monoxide oxidation at temperatures below room temperature. Conversion of poisonous carbon monoxide into harmless carbon dioxide, using gold catalysts, could potentially improve the effectiveness of catalytic converters that clean automobile exhaust as well as breathing devices used by miners and firefighters. Over the last decade the term gold nanoclusters (GNCs) have partially replaced the term gold nanoparticles (GNPs) as several scientist claim that a cluster is defined as an agglomerate consiting of 2 to $\approx$20 atoms.[3,4,5,6] In addition to selective oxidation of carbon monoxide, selective reduction of NO in the presence of O_2 and epoxidation of propene are reactions where GNCs has been reported as a outstanding catalyst.[7,8] In previous studies, metal oxides such as TiO_2 and Fe_2O_3, as well as carbon nanostructures, has been investigated as supports for GNCs.[9,10,11,12] Recently, the interest on zeolites as support for GNC catalysts has grown. Wan *et al.*[13] reported how the the various conditions, such as temperature and pH of the solution, affected gold's catalytic performance. In the studies mentioned above, primarily characterization techniques such as Transmission Electron Microscopy (TEM) and X-ray Photoelectron Spectroscopy (XPS) operating under high vacuum have been used to investigate the Au/support samples. Due to the fact that gold has a strong tendency to sinter and form gold oxides, other charac-

terization techniques were applied in this work on Au/zeotypic samples.

Zeolites and zeotypes are microporous crystalline aluminosilicates which exhibit unique catalytic properties. In addition to their three-dimensional nanostructure, they have a high surface to volume ratio, and high adsorption capacity.[14] They have shown themselves to be excellent catalysts as well as suitable support materials for a variety of catalytical reactions, one example being the selective catalytic reduction (SCR) of NO_x.[15,16]

To investigate catalysts X-ray Absorption Spectroscopy (XAS) has proven itself to be an excellent characterization technique. The characterzation method gives detailed information about the local structure around the atoms of a specific element. For XAS measurements synchrotron radiation is generally used. Compared to conventional X-ray sources such as X-ray tubes and rotating anodes, synchrotron radiation are hundreds of thousands times higher in energy. The radiation is extremely intense and possesses a high flux which greatly improves the signal to noise ratio, thus reducing the acquisition time to 30 minutes compared with days as is the case with conventional X-ray sources. Due to the high flux even elements present in low concentrations are able to be investigated. XAS measurements under *in-situ* conditions allows the temperature and pressure during the experiment to be altered to simulate "real conditions" of a working catalyst. XAS has therefore shown itself to be a unique characterization technique for studying both crystalline and amorphous catalytic materials.[17]

1.1 Scope of this work

This thesis is concerned with the synthesis and characterization of gold incorporated silicoaluminophospahtes (SAPOs), and the gold ion-exchanged zeolites ZSM-5 and HY, and zeotype SAPO-34. The aim was to incorporate gold into the framework of SAPO-5, and to introduce gold as homogeneous distributed gold cations on the surfaces of the zeolites ZSM-5 and HY, and the zeotype SAPO-34. Further, a reduction of the gold cations to metallic gold atom was desired as metallic gold atoms tend to agglomerate into small gold nanoclusters (GNCs). It

is especially important that the gold cations are dispersed on the surface before the reduction occurs since an auto reduction of the gold cations during synthesis/ion-exchange leads to agglomeration of large GNCs ($>$ 10 nm). Small GNCs are known to be catalytic active in a variety of reactions, one being the oxidation of carbon monoxide to carbon dioxide.

SAPO-5 and SAPO-34 was chosen as support materials due to their interesting properties, which includes molecular sieving properties, shape selectivity and high thermal stability. In addition, the SAPOs have a net negative charge located on an oxygen atom, thus making it possible for gold cations to react with these acid sites. The microporous materials consist of large pores with a large internal surface area, hence making them highly interesting in terms of catalysis. The zeolites ZSM-5 (two dimensional framework) and HY (three dimensional framework) were chosen to investigate whether the structure of the support is a crucial factor for a homogeneous distribution of gold cations during both conventional and hydrothermal ion-exchange procedures. In addition, ZSM-5 and HY with high Si/Al ratios were chosen since zeolites with high Si/Al ratios have the strongest acid sites.

To be able to monitor the gold oxidation state X-ray Absorption Spectroscopy (XAS) has been used as the main characterization technique. At European Synchrotron Radiation Facility (ESRF) in Grenoble, France and at MAXLab in Lund, Sweden, synchrotron radiation was used to investigate the gold environments both *ex-situ* (at room temperature in air) and *in-situ*. The X-ray Absorption Near-Edge region (XANES) provides information regarding the oxidation state of gold. When the measurements are carried out *in-situ*, i.e. conditions which allows the temperature and pressure during the experiment to be altered, the oxidation state of gold can be monitored during the different stages of the reaction. Measurements in the Extended X-ray Absorption Fine Structure region (EXAFS) provides structural information about the local environment surrounding a gold atom. The multiplicity, i.e. the number of neighboring atoms surrounding the gold central atom, can be used to determine the GNC sizes at the different stages of the reaction.

In addition, characterization methods such as Powder X-ray Diffraction (PXRD),

Temperature-Programmed Reduction (TPR), Nitrogen adsorption analyses (BET) and Inductively Coupled Plasma Mass Spectrometry (ICP-MS) have been applied for phase determination, stability measurements, surface area measurements and elemental analysis, respectively. These techniques were preformed at the Norwegian University of Science and Technology (NTNU), Trondheim.

Activity measurements for the selective catalytic reduction (SCR) of NO_x were suppose to be carried out at The University of Newcastle in Australia. Due to technical complication this was not possible. Instead, activity measurements for the oxidation of carbon monoxide and preferential oxidation of carbon monoxide (PROX) were carried out to examine the catalytic performance of the samples. Note that the samples presented in this work are therefore prepared with respect to SCR of NO_x, and not with respect to CO oxidation and PROX, in terms of preparation methods, preparation conditions, ect. This is also the reason why the XAS in-situ studies presented in this thesis have been carried out with a nitric oxide/ helium gas mixture as the oxidizing atmosphere.

Chapter 2

THEORY

This chapter will present characteristics of the materials and metal used to prepare the potentially catalytic samples investigated in this thesis. It will also be given a description of the techniques applied to characterize the samples. The background to these subjects are essential for understanding the later results and discussions.

2.1 Microporous materials[18,19,20,21]

2.1.1 Zeolites and zeotypes; an introduction[18,19,21]

The term zeolite was coined in 1756 by Swedish Cronsted who observed that the mineral stilbite frothed and gave off steam when heated. This discovery gave rise to the name zeolite, which originates from Greek and means "boiling stone". In addition to the 56 naturally occuring zeolites, many zeolites are also manufactured synthetically and represents a large portion of the chemical industry. Zeolites and zeotypes are used as cation exchangers for water softening, and as molecular sieves for separating molecules of different shapes and sizes (e.g. as drying agents). Since the 1960s more research have been focused on their ability to act as catalysts in a wide variety of reactions. This quest for new catalysts have led to a development of over 150 synthetic zeolite and zeotype structures. Zeolite and zeotypes are three-dimensional, crystalline aluminosilicate minerals based on rigid anionic frameworks with well-defined pores which intersect at cages. These cages contain exchangeable metal cations (Na^+, K^+, etc.). The size of the cages are between 200 and 2000

ppm, thus zeolites and zeotypes are classified as microporous materials.

2.1.2 Composition and structure

Zeolites and zeotypes are constructed from TO_4 tetrahedra, where T is either Si or Al, linked together by bridging oxygen. The general formula for aluminosilicate zeolite is given in Equation 2.1.

$$xM_{\frac{2}{n}}O \cdot xAl_2O_3 \cdot ySiO_2 \cdot zH_2O \tag{2.1}$$

The framework carries a net negative charge equal to the number of tetrahedral aluminum ions, also known as an acid site. By introducing a corresponding number of non-framework cations, M, the net negative framework charge (n) is balanced. These non-framework cations are usually sited in, or have access to, the pores, and can easily be exchanged for other ions by treatment with a suitable salt solution. Zeotypes are referred to as other synthesized framework structures containing atoms such as aluminum and phosphorus tetrahedrally coordinated by oxygen. The pores of zeotypic materials also impart large internal surface areas to the structures. This characteristic makes them interesting for separation, ion-exchange (in the case of zeolites) and for emerging applications in catalysis. Perhaps the most commercially valuable and dynamic property of zeolite and zeotype is their cation exchange capacity (CEC). Cation exchange occurs when two or more positively charged compounds or elements exchange places on a negatively charged host. A classic example of cation exchange is the removal of ammonia. When a molecule of ammonia (NH_3) is hydrated, the reaction produces ammonium (NH_4^+), which is easily protonated to an acid site (H^+) during calcination.

2.1.3 Synthesis of zeolites and zeotypic samples

Zeolites and zeotypes are usually crystallized from gels containing silica and alumina sources and basic agents. Metal cations can be added to the synthesis mixture if metal incorporation is desired. The synthesis is carried out under hydrothermal conditions, at basic pH and in the temperature range 60-200 °C. Often, the presence of organic compounds is required during the synthesis, thus acting as

structure-directing agents (templates). The synthesis of zeolites and zeotypes involves several steps, as illustrated in Figure 2.1. The process is thermally activated and usually takes place at elevated temperatures and pressures to achieve a high yield of crystals. Among the process variables are temperature, alkalinity (pH) and chemical composition of the reactant mixture. Making the reactant mixture is a step-by-step procedure where the order of reactant put into the mixture can be crucial. It is therefore important to add the ingredients subsequently as described in the guidelines for the synthesis of interest, and make a note of the reactant amount used and measure the pH at all time.

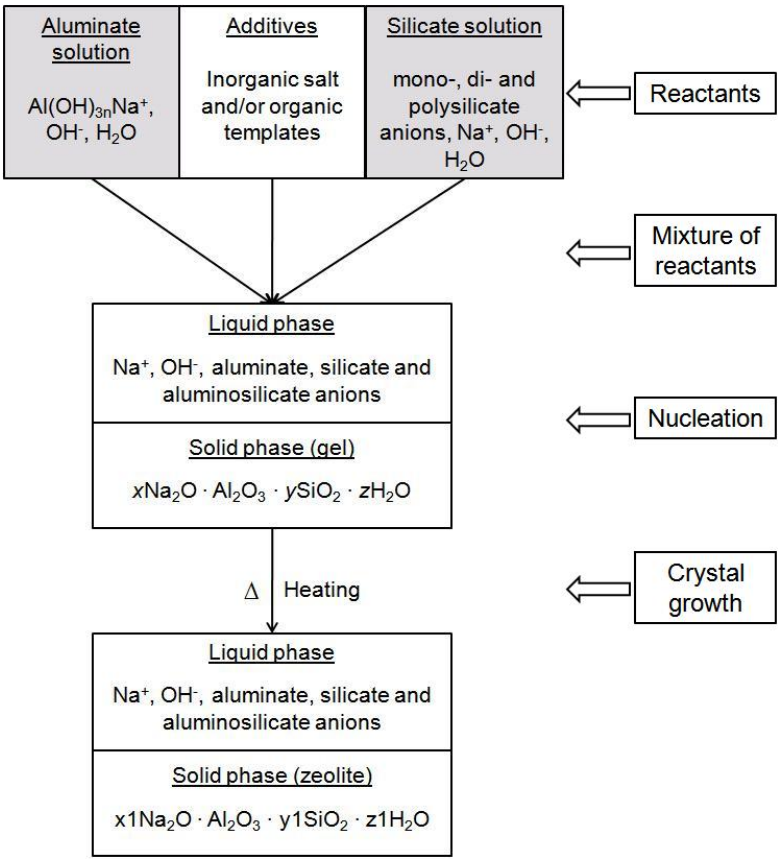

Figure 2.1: General scheme for zeolite and zeotype crystallization

After careful preparation of the precursor, a suitable reaction vessel has to be selected to provide the desirable hydrothermal conditions of elevated pressure and temperature for crystal growth. Usually an autoclave is used, making it possible to

heat the reaction mixture above its boiling point at normal atmospheric pressures. When the solution is heated in an autoclave, the pressure rises due to the constant volume of the container. The boiling point of the solution is raised as the amount of energy needed to form steam against the higher pressure is increased. After heating, the gel is released from the autoclave and typically washed with distilled water through a filter, followed by drying of the precipitate.

As the final step, the obtained powder undergoes a calcination process. The process involves heating of the powder up to a certain temperature, determined by the template decomposition, in an oxygen rich atmosphere. Calcination is done to free the pores and are subsequently converted into the active acid. The calination process is also done to investigate the thermal stability of the obtained powder. If the calcination process leads to a collapse of the zeotypic structure, the obtained material is not considered useful in terms of catalysis.[20]

2.1.4 Ion-exchange of zeolites and zeotypic samples

The properties of zeolites and zeotypes allow the replacement of cations held in their aluminosilicate anion framework by ions present in external solutions. Ion-exchange is often used to modify the catalytic or molecular sieving actions of the parent zeolite or zeotype. With the potential for such a modification virtually every cationic form in the Periodic Table can be introduced into the zeotypic framework. The ion-exchange properties for a zeotypic material is controlled by the zeotypic framework and its geometry (shape selectivity), hence the geometry of the pore opening will determine which ions that will diffuse into them. In addition, the reaction temperature and the ion-exchange method plays an important role. The temperature can influence the removal of water of hydration, and the accessibility of sites and exchange kinetics.

Ion-exchange of zeolites and zeotypes can be carried out either conventionally or hydrothermally. Conventional ion-exchange involves mixing the zeotypic material with the metal precursor to a slurry, which is kept stirring overnight. With respect to hydrothermal ion-exchange, the zeolite or zeotype and the metal precursor is

directly added to an autoclave and heated to ≈ 100-150 °C at standard pressure. The amount of metal ion which can be incorporated is up to ten times higher for hydrothermal ion-exchange than what for the conventional method, using the same metal precursor.

The work included in this thesis has been carried out using the zeolites H-ZSM-5 (calcined to ZSM-5) and HY; and the zeotypic systems SAPO-5 and SAPO-34. Ion-exchanged zeotypic samples (Z) are typically denoted Me:Z whereas a metal incorporated during the actual synthesis of the microporous support is denoted MeZ.

2.1.5 Catalytic properties

Zeolites and zeotype possess unique properties, which is not the case for their amorphous analogues, thus making them suitable as both catalysts and calaytic supports in a wide variety of industrial processes. Some of the properties of these three dimensional structures are:[14]

- High surface area
- Molecular dimensions of the pores
- Acid activity
- High absorption capacity
- Shape selectivity properties

The surface of zeolites and zeotypes can possess either a Brønsted or Lewis acid site depending on the preparation of the material. Brønsted acid sites are often converted to Lewis acid sites when temperature exceeds ca 500 °C and water is removed, as shown in Figure 2.2. The acid sites strength is directly related to the framework composition of the zeolitic material, and it is reported that zeolites with a high Si:Al ratio have the strongest acid sites.[18]

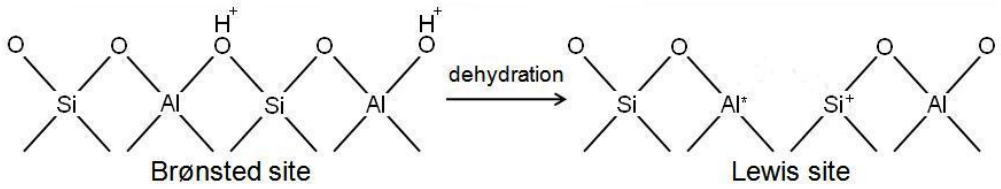

Figure 2.2: Brønsted and Lewis acid sites

In addition to their acid sites, zeotypic microporous materials exhibit unique pore structures with a wide range of diameters (0.3-2.0 nm). These pores give rise to the ability for molecular sieving. The fact that zeolite pores are similar in size to reactant molecules introduced the term "shape selectivity" in the 1960's, which refer to the selectivity achieved in heterogeneous catalytic reactions and depends on the pore width or framework architecture of the microporous material used. Today, shape selectivity is classified into three categories; *reactant shape selectivity*, *product shape selectivity* and *transition state selectivity*, as seen in Figure 2.3.[22,23,24,25]

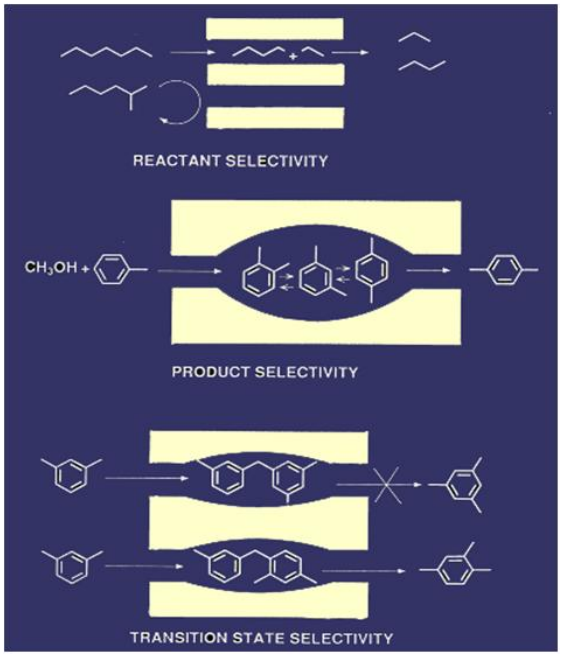

Figure 2.3: The three main categories of shape selectivity[25]

Reactant shape selectivity (RSS) refers to the case where two or more reactants of different sizes can reach the inner active site of a catalyst. The geometry of the pore opening will determine which reactant that will diffuse into them. When two or more products are formed in reactions at pore intersections, the pore structure will decide which product than can diffuse to the outside of the pore structure. This is called product shape selectivity (PSS). The last case, transition state selectivity (TSS), refers to the case where reaction intermediates or transition states are formed inside the zeolite, but the outgoing pore structure will only diffuse one of the transitions states, leaving the other trapped inside the zeolite.[22]

2.1.6 The zeolites ZSM-5 and HY

Zeolite ZSM-5 (Zeolite Socony Mobile No.5, International Zeolite Association structure type MFI) was first synthesized my Argauer and Landolt in 1972 (U.S Patent 3,702,886).[26] It is a aluminosilicate zeolite with a high silica and low aluminum content. ZSM-5 has a structure formed by tetrahedral [MO_4] primary units linked together through corners to form a three-dimensional framework characterized by two types of intersecting channels. However, the pore structure is considered to be two-dimensional. The two types of pores are both formed by 10- membered oxygen rings. The first type is straight and elliptical in cross section with diameters of about 0.54 x 0.56 nm. The second type of pores are sinusoidal intersecting the straight pores in a zig-zag pattern and are circular in cross section. These channels have a free diameter of 0.55 x 0.51 nm.[27] The structure is illustrated in Figure 2.4.

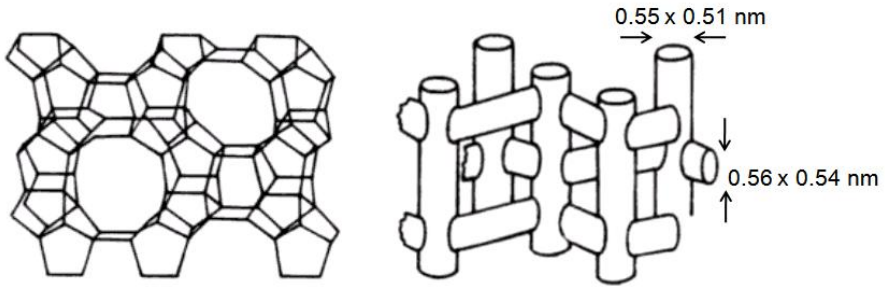

Figure 2.4: Structure of ZSM-5 zeolite[27]

Substitution of Al^{3+} in place of the tetrahedral Si^{4+} requires the presence of an

added positive charge. This additional positive charge (proton) gives the zeolite a high level of acidity, thus high activity. The standard formula for ZSM-5 is $(Na^+)_n(H_2O)_{16}[Al_nSi_{96-n}O_{192}]$. The fraction n can be calculated using the molecular weights (Mw) of Si and Al according to equation 2.2 when the the Si:Al ratio is known:

$$\frac{Mw_{Si} \cdot (96 - n)}{Mw_{Al} \cdot n} = Si : Al \tag{2.2}$$

In the case of Si:Al= 40, n equals ≈ 2 yielding the formula $(NH_4{}^+)_2(H_2O)_{16}[Al_2Si_{94}O_{192}]$. When calcined at 550 °C, the standard ammonium form yields it calcined form, shown in equation 2.3

$$(NH_4^+)_2(H_2O)_{16}[Al_2Si_{94}O_{192}] \overset{calcined}{\rightarrow} (H^+)_2(H_2O)_{16}Al_2Si_{94}O_{192} + 2NH_3 \tag{2.3}$$

The formula weight for protonated ZSM-5 is 6056 g/mole, which has 2 exchangeable sites. Thus, the cation exchange capacity (CSC) is 2 equivalents per 6056 gram. Recalculating yields 1 milliequivalents (meq) per gram of ZSM-5. The amount of cation that can be exchanged into 1 gram of zeolite is calculated by multiplying the number og milliequivalents of a given cation with the gram-equivalent weight. For trivalent cation, this has to be divided by three, as only one third of the amount can be exchanged. Taking trivalent gold as an example, the grams of equivalent weight is:

$$\frac{196.967eq}{3} = \frac{65.656eq}{1000} = 0.0657meq \tag{2.4}$$

100% exchange of gold in ZSM-5 will therefore correspond to 6.567 Au wt% according to Equation 2.5:

$$\frac{1meq}{g} \cdot 0.0657meq \cdot 100\% = 6.567Auwt\% \tag{2.5}$$

Zeolite HY (International Zeolite Association structure type faujasite, FAU)[26] have

192 tetrahedral sites per unit cell. It is formed from 24-tetrahedra cuboctahedral units (sodalite cages), joint through hexagonal prisms (double 6-rings). A characteristic feature for this zeolite is the supercages (diameter 1.2 nm) which are linked through pores about 0.8 nm in diameter composed by rings of 12 linked tetrahedra (12-rings). These cages and pores allow access of quite large molecules to the zeolite, making the structure useful for catalytic applications. In some applications incorporation of metal cations into a zeolite sieve is desirable to modify the number and nature of the acid sites. The metal cation normally occupy one of the five sites (I, I', II, II' or V) shown in Figure 2.5.

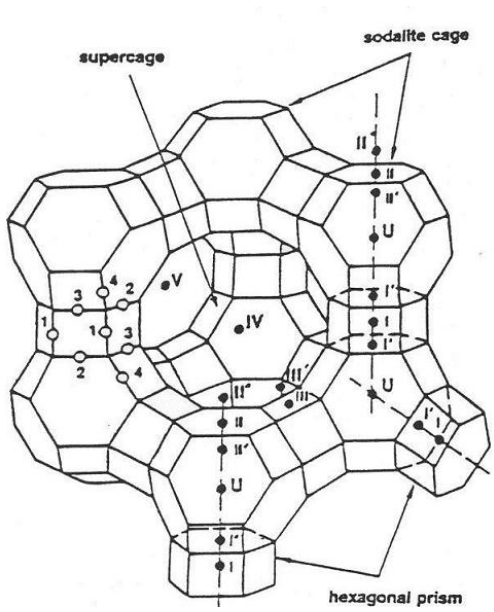

Figure 2.5: The faujasite structure, illustrating the oxygen positions and possible sites for ion-exchange[28]

I indicates occupation at the center of the double 6-rings, while I' is in the sodalite cages, adjacent to a hexagonal ring shared by the sodalite cage and a double 6-ring. An increase in Si:Al ratio (decrease in framework charge) depopulates the sites I and I' in the hydrated zeolite, i.e. the cation present prefer a water environment to the framework coordination positions. The absence of water causes an increase in the population of site I and I' regardless of framework charge. If the metal cation is incorporated in position II, it is trapped within the supercage. This is often

the case for ion exchange of large metal cations. Occupation in the sodalite cages, adjacent to an unshared hexagonal is the site labeled II', and V is occupation near the center of the 12-ring apertures between supercages. Zeolite HY has the formula $Na_pAl_pSi_{192-p}O_{384}{\cdot}qH_2O$, with $78 \leq p \leq 74$. q (the amount of water) drops from 270 to about 250 when Al decreases.[28,29]

Both ZSM-5 and HY are used as both catalysts and catalytic support materials in a variety of industrial processes worldwide. ZSM-5 is used in the petrochemical industry for hydrocarbon interconversion. The pores make it a perfect catalyst for the methanol-to-gasoline process (MTG). The 10-membered rings allow only the desirable hydrocarbons to penetrate pores, thus producing gasoline. HY is used as a catalyst in fluid catalytic cracking to convert heavy fractions of petroleum crude (vacuum and atmospheric residue) to more valuable products like gasoline, diesel and other products. Due to the high Si:Al ratio the zeolite maintain high stability and activity at high temperatures.[27]

2.1.7 Silicoaluminophosphates (SAPOs)

As mentioned in Section 2.1.1, the framework structures containing atoms such as aluminum and phosphorus tetrahedrally coordinated by oxygen are generally called zeotypes. Pure aluminum phosphate (commonly known as AlPO) and its derivatives are known to take the same structural forms as some of the zeolites. A partially replacement of aluminum or phosphorus by silicon gives rise to the zeotypes known as silicoaluminophosphate, SAPO. Replacing phosphorus with silicon introduces a net negative charge to the SAPO framework. The resulting bridged hydroxyls are Brønsted acid sites which can serve as catalytically active sites, and also makes it possible for ion-exchange. Metal ions can occupy sites in the SAPO framework, creating a MeSAPO, which may improve the catalytic behavior. The creation of acid sites and metal incorporation in SAPO is shown in Figure 2.6.[18]

The local structure of Brønsted acid sites in zeolites and SAPO are similar, both consisting of Si-O(H)-Al units. Although they are structurally similar samples, the acidity varies a lot. The acidity depends among others on bond angles, bond

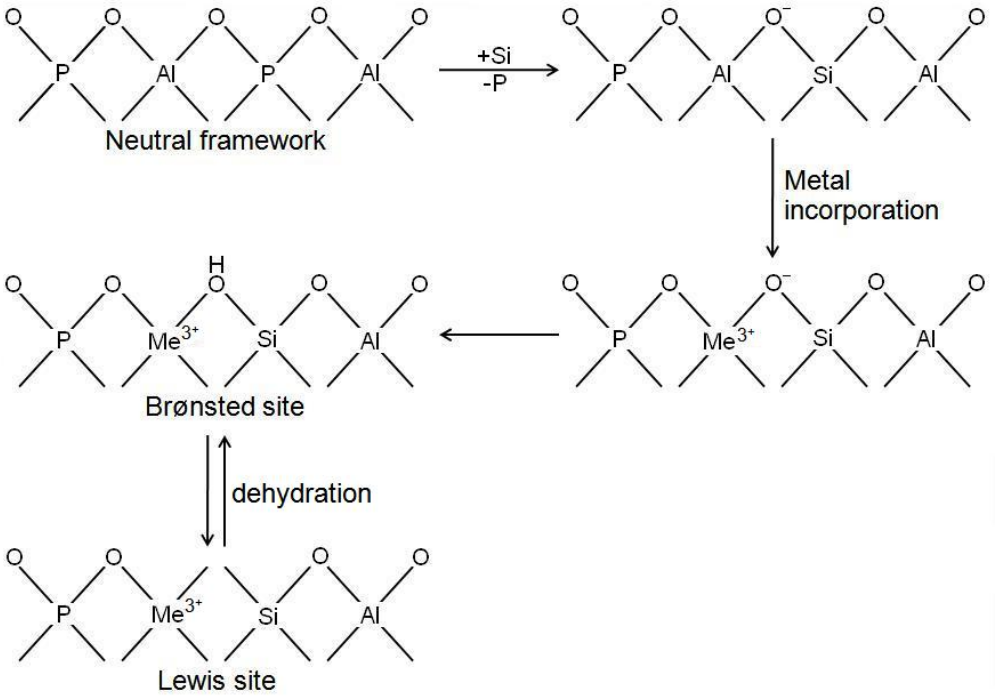

Figure 2.6: Creation of acid sites on framework incorporation of divalent metal cations into silicoaluminophosphates

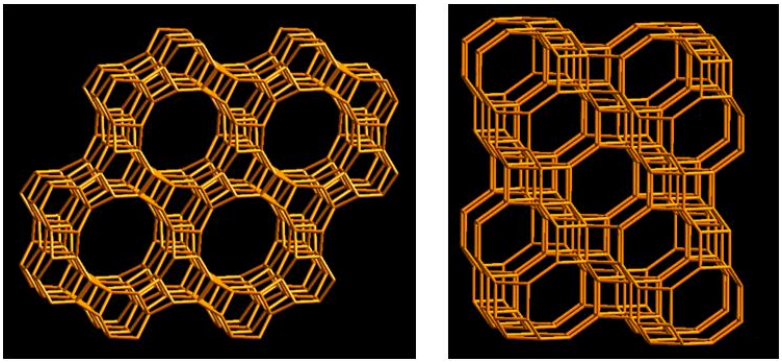

Figure 2.7: Structure of the zeotypic samples SAPO-5 (AFI, to the left) and SAPO-34 (CHA, to the right)[26]

lengths, and the electrostatic potential around the acid centers and within the zeolite cages. Especially the environment around the acid centers plays a important role. The first coordination sphere of T atoms around the aluminum is formed exclusively of Si in zeolites, whereas Si and P can be present in SAPOs. In addition, the formation of Si islands in SAPOs leads to an even higher number of acid site

environments. This makes SAPO's acidity more tunable than in zeolites, provided that the Si insertion can be controlled.[30] The first procedure for the synthesis of silicoaluminophosphates was reported by Lok *et al.*[31]. Today numerous of different SAPO structures are synthesized, separated from each other as SAPO-n, n being a number referring to the specific structure of the zeotype. These different silicoaluminophosphates possess a great number of various International Zeolite Association (IZA) structures; SAPO-11 has a AEL structure, SAPO-18 possesses a AEI structure, while SAPO-31 has a ATO structure, and so on.[26]

SAPO-5 (AFI structure)[26] is build up by one-dimensional 12 membered-rings with a relatively large pore diameter of 0.73 nm. SAPO-34 has a chabazite (CHA) structure consisting of 8 membered-rings with a diameter of 0.38 nm. The inner cage of the zeotype has a volume of 0.67 nm $\times$ 0.67nm $\times$ 1nm.[32] The two structures are illustrated in Figure 2.7. The great interest in SAPO molecular sieves is noted by numerous publications, a large part concerning the application of SAPO in catalysis.[30] An example is the use of SAPO-34 as a catalyst in the UOP/Hydro MTO process for conversion of methanol to light olefins (MTO).[32,33]

2.2 Catalysis by gold

2.2.1 Introduction[34]

For thousands of years, gold has been reckoned as the most noble metal. Gold is unique among the metallic elements for its resistance to oxidation and corrosion, and has therefore been used in jewelries for thousands of years. Until the 20^{th} century, gold had never been considered a good metal for catalysis due to its chemical inertness in bulk form. However, over the last decades scientists have made remarkable discoveries which conclude that gold can serve as a catalyst when it is present as small gold nanoparticles (GNPs) or small gold nanoclusters (GNCs). The inertness of bulk gold in mainly due its inability to chemisorb typical reactant molecules to any useful extent. The chemisorption occurs only when an adequate number of low-coordination surfaces are present, ideally on particles so small that they lack full metallic character. Selective and nonselective oxidation of hydro-

carbons, hydrochloration of ethylene and reduction of nitric oxide by hydrogen, propene, or carbon monoxide are some catalytic reactions where gold catalysts is reported to have a great potential.

Both GNPs and GNCs are terms used widely literature, yet there is not a distinct partition between the two expressions. Some scientist claim that GNPs are defined as a particle with a size smaller than 50 nm.[34] Others tend to use the term GNCs when more than two metallic gold atoms are agglomerated.[3,4,5,6,35,36] In this thesis the term GNPs will be used for mononuclear gold refined to have a first shell Au-Au multiplicity < 1.1 during EXAFS analysis. Gold agglomerates consisting of less than ≈ 30 Au atoms, i.e. a first shell Au-Au multiplicity < 9, will be termed small GNCs.

2.2.2 Physical and chemical properties of gold[34]

To understand the catalytic properties of small GNPs and GNCs knowledge about the bonding capabilities of gold surface atoms is essential. Gold (Z=79) has the electron configuration [Xe]$4f^{14}5d^{10}6s^1$, which places it in Group 11 in the periodic classification of elements, right next to platinum who is classified in Group 10. Platinum is already known as a versatile catalytic metal and is widely used in commercial processes, one example being the three-way-catalyst sample in automobiles. The physical properties of Pt and Au are listed in Table 2.1.

The chemical properties of Au and Pt are dominated by the relativistic stabilization of the $6s$ level, due to the $6s^2$ state's "inert pair effect". An important consequence is that the electrons in the $5d$ level are more easily mobilized for chemical reactions. This is why Pt has the electron configuration $5d^96s^1$. In the case for gold ($5d^{10}6s^1$), its chemistry is determined by *(i)* the easy activation of the $5d$ electron as a consequence of the "inert pair effect" and *(ii)* its desire to obtain a further electron to complete the $6s^2$ and not lose the one it already has. The first effect explains why Au^{3+} is the predominant oxidized state, which has the $5d^8$ configuration. Au^+ is also known to be a stable state, although somewhat harder to achieve than Au^{3+}. Au^{2+} is a rare state which only appears in a few

Table 2.1: Physical properties of Gold compared to those of Platinum

Property	**Pt**	**Au**
Atomic number	78	79
Atomic mass	195.08	196.9665
Electronic configuration	$[Xe]4f^{14}5d^{9}6s^{1}$	$[Xe]4f^{14}5d^{10}6s^{1}$
Structure	fcc	fcc
Lattice constant (nm)	0.392	0.408
Metallic radius (in 12-coordination) (nm)	0.1385	0.14420
Density (g cm^{-3})	21.41	19.32
Melting temp. (°C)	1769	1064
Boiling temp. (°C)	4170	2808
Sublimation enthalpy (kJ $mole^{-1}$)	469 ± 25	343 ± 11
First ionization energy (kJ $mole^{-1}$)	866	890

unusual complexes. The latter effect gives gold a much higher electron affinity and higher first ionization potential than those known for elements with lower Z, for example copper (Cu) or silver (Ag).

Gold's electro negativity (2.4) is equal to what for selenium and approaches that for sulfur and iodine (2.5). It is therefore often said to have some of the properties of a halogen. The electrode potential of Au, E^0, is +1.691 eV, i.e. very high for a metal. The nobility is determined by its electronic structure (fcc), and gold is unable to interact with oxygen and sulfur compounds in its bulk form. This is why gold oxides are very unstable. For example Au_2O_3 decomposes at ≈ 160 °C and has a weak negative to a positive heat of formation, ΔH_f, ranging from -3.7 and +160 kJ $mole^{-1}$.[34] An interesting point is that the electronic state of gold atoms in the bulk state is not exactly the same as for the free atoms. This is shown by a weak white line on the Au L_{III} X-ray absorption edge, that indicates a small number of holes in the *d*-band caused by *d*-*s* hybridization. This phenomenon will be discussed in greater detail in Section 2.7.1.

2.2.3 Physical and chemical properties of small gold particles and clusters[34]

The surface of bulk gold exhibits some modest catalytic properties, mainly because the large gold agglomerates (GNCs $>$ 50 nm) it obtains. An element's activity per unit mass will depend on the fraction of atoms on the surface, thus clearly increase when GNP size is made smaller. This fraction is called the *degree of dispersion*, and can easily be calculated assuming that unit mass is converted into spheres where all the spheres have the same size. The dispersion dependence on the mean particle size, is shown in Figure 2.8.

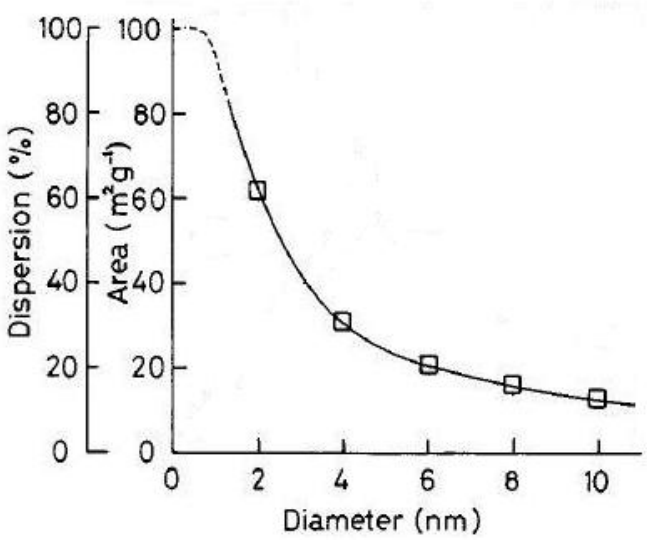

Figure 2.8: Dependence of dispersion on cluster diameter for uniform spheres of gold[34]

According to the figure, a 2 nm GNC has approximately 60% of its atoms on the surface. As the cluster size increase, the dispersion decrease, giving the GNCs lower activity, thus poorer catalytic ability. Note that this calculation on dispersion is based on perfect structures, i.e. to clusters having the exact same size through out the entire structure. This is of course not the case in reality since a real catalyst will contain particles and clusters of different sizes. Small GNCs are known to be very energy-rich, due to the excessive energy that is created when large gold bulk agglomorates are degraded. As size decreases, the proportion of

atoms at or close to the surface that are incompletely bounded to their neighbors, will increase. This gives a lower coordination number of atoms in a cluster, thus give rise to more unemployed orbitals that will have a great effect on the GNCs' properties. The physical property is therefore often said to be related to the inverse of the GNC size. The GNC shape also depends on its size. GNCs with a particle size of 1-10 nm are known to be spherical, but larger GNCs (20-50 nm) possess specific shapes and definite facets. For large ($>$ 50 nm) GNCs the shape can be tailored by varying the different ingredients, which can lead to formation of cubes, rods or even triangular shapes. Up until this date, these GNPs have not been used as catalysts.

In 1857, Michael Faraday delivered the Bakerian Lecture of the of Royal Society entitled "*Experimental Relations of Gold (and other Metals) to Light*". Regarding the action of light on what then was known as small gold particles he stated that a "*phenomena appeared to indicate that a mere variation in the size of its particles gave rise to a variety of resultant colors*".[37] Since that statement, the unique feature of gold in its microparticulate state, and the range of the color it can exhibit have been widely investigated. During citrate reduction, the color changes from gray through lavender to red. 1-3 nm GNPs and GNCs are known to have a brown or dark orange-brown color and 5 nm GNCs are purple-brown or purple-red. Large GNCs have a ruby red color and partially coagulated sols are blue. The optical absorption spectrum of larger GNCs ($<$ 40 nm) has a maximum at 520 nm, while blue colors arise from absorption at 680 nm. Intermediate color shades for the GNCs are therefore possible.

Figure 2.9 shows gold solutions containing GNCs of different sizes.[38] The colors of the different cluster sizes are due to *plasmon resonance.* An interaction between the electric field of visible lights and the confined electron gas within the clusters causes a collective oscillation of the conduction electrons with respect to the core. The resonance weakens and shifts towards higher energy as size decreases. Below 2 nm the resonance disappears completely.

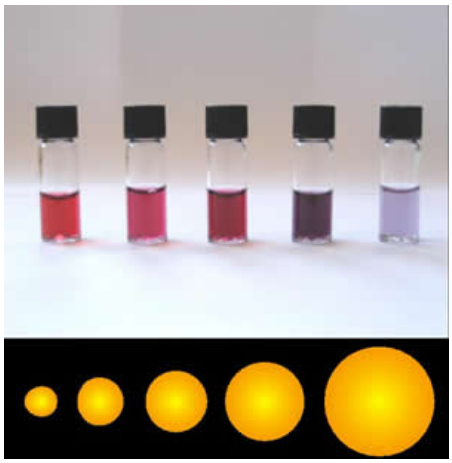

Figure 2.9: Colors of gold nanoclusters[38]

2.2.4 Techniques for studying small gold clusters

A variety of methods can be used to determine the structure of GNCs (size, size distribution, shape, composition etc.). Due to the chemical inertness of bulk gold, methods based on the chemisorption of simple molecules have so far failed to give acceptable quantitative results. *Scanning Electron Microscopy* (SEM) gives a low-resolution image of the GNCs. This technique reveals structures like shape and size of support particles. However, for diluted gold samples the GNCs are hard to detect due to high instrumental detection limit. Information about the size of metal GNCs, L, can be obtain from *Powder X-ray Diffraction* (PXRD), by using the Scherrer Equation:

$$L = \frac{0.9\lambda}{k\cos\theta} \tag{2.6}$$

λ denotes the wavelength of the X-ray, θ is the angle of incident and k is the full width half maximum of a diffraction peak for the component of interest. However, for small GNCs ($\leq$5 nm) the broadening of the peak is of such a character that it cannot be accurately estimated. For GNCs above 100 nm, the peak becomes too narrow. Another technique that is widely used for particle size and shape determination is *Small-Angle X-ray Scattering* (SAXS). This method looks at X-ray scattered within a few degrees of the primary beam, making it possible to determine GNC sizes as small as 1 nm. X-ray Absorption Spectroscopy (XAS) is an

excellent characterization technique for both crystalline and amorphous materials. Data analysis of the Extended X-ray Absorption Fine Structure (EXAFS) region of the XAS spectrum supplies an estimate of the GNCs' mean size. EXAFS will be discussed in greater detail in Section 2.7.2. To determine GNCs' size from EXAFS data Equation 2.7 can be used, assuming spherical agglomerates.[39] The equation is based on data for Pf (fcc) and can be adapted to other metals by correcting for the difference in interatomic distance between the Au and Pt.

$$N_{Pt-Pt} = \frac{MW_{Pt}}{N_{AV} \cdot Pt_{loading}} \int_{size=0}^{\infty} \frac{P}{g_{zeolite}}(size) \cdot A(size) \cdot N_{Pt-Pt}(size) dsize \quad (2.7)$$

where;

- $\frac{P}{g_{zeolite}}(size)$ is defined as the number of platinum particles per size per gram catalyst
- MW_{Pt-Pt} is the molecular weight of platinum (g/mole)
- N_{AV} is Avogadros number
- $\mathrm{Pt}_{loading}$ is the weight of platinum per weight of zeolite(g Pt/g zeolite)
- $\mathrm{A}(size)$ is the number of platinum atoms per particle size
- $\mathrm{N}_{Pt-Pt}(size)$ is the first-shell coordination number of platinum particles per size

To use Equation 2.7 information about $\mathrm{A}(size)$ and $\mathrm{N}_{Pt-Pt}(size)$ must be obtained. Figure 2.10 represents the modeling and calculations prepared by de Graaf *et al.*[39], and can be used directly to find the sizes for the GNCs present in the sample investigated in this thesis. However, the method has its disadvantages as GNCs with a multiplicity (N_{Au-Au}) lower than 4 cannot be measured. In addition, to detect the GNCs one has to manually determine the cluster size by sketching on the plot given in Figure 2.10.

GNCs having a high coordination number (>11) the slope of the plot decreases making it hard to determine the exact size of the GNCs. When the GNC size is

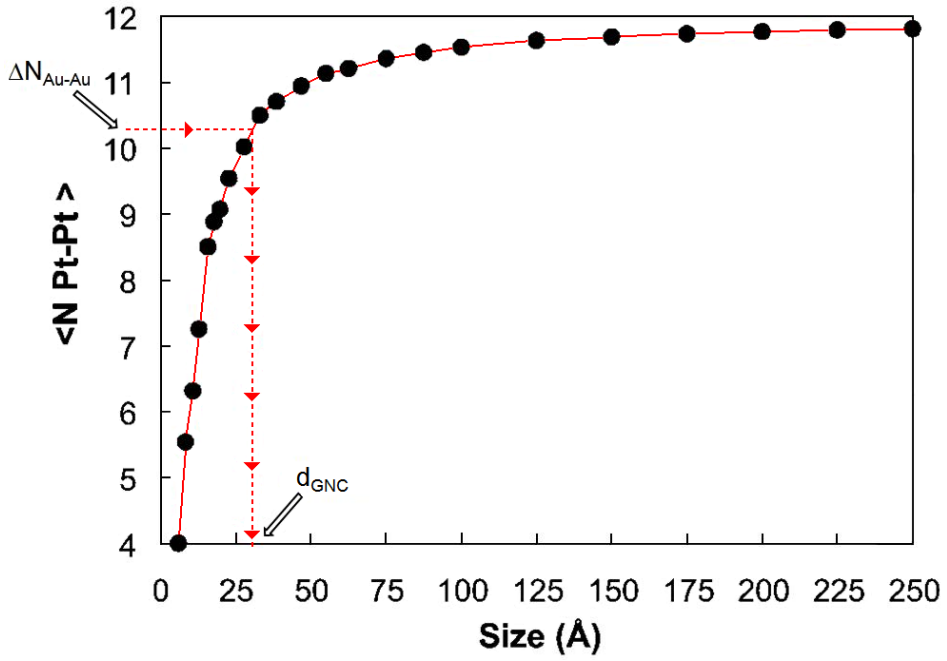

Figure 2.10: First-shell multiplicity N_{Pt-Pt} per modeled particle in the size range 0.5-25 nm[39]. The red line illustrates the particle size for a gold cluster with N_{Au-Au}=10 after correcting for the difference in interatomic distance between Au and Pt.

known it is possible to define the shape of the GNCs to some extent. Figure 2.11 sums up results reported by several scientists based on calculations of cluster sizes in accordance with de Graaf *et al.*[39]. Cunningham *et al.*[6] have reported that GNPs with a multiplicity of the first Au shell in EXAFS (N_{Au-Au}) < 1.1 possesses a icosahedral particle shape. van Bokhoven and his co-workers[4] have reported of GNCs consisting of 4 to 6 Au atoms when N_{Au-Au} equals 3.8, while Guzman *et al.*[35] have reported of Au_6 nanoclusters when N_{Au-Au} is refined to be 4.0. As the multiplicity reaches 9.4 the GNCs are suggested to consist of 80 Au atoms.[35]

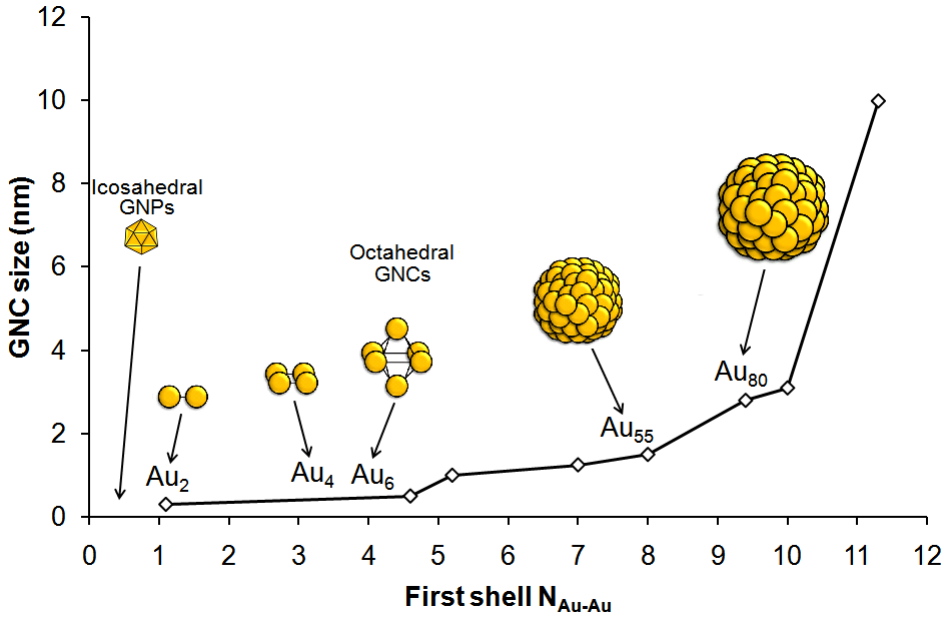

Figure 2.11: GNC sizes and shapes given as a function of the first-shell multiplicity N_{Au-Au}. The plot is based on values reported elsewhere[3, 4, 5, 6, 35, 39]

2.2.5 Oxidation of carbon monoxide catalyzed by gold[34]

Since the discovery made by Haruta *et al.*[1,2] on the catalytic activity of what he termed small gold particles ($\leq$ 5 nm) with respect to carbon monoxide (CO) oxidation, there has been an astonishing growth of interest for supported gold catalysts. Over the last decade the term "small gold particles" has more or less been exchanged with small gold nanoclusters as there is a general agreement that clusters are defined as gold agglomerates containing few (from 2 to $\approx$ 20) Au atoms. Today, the term small gold nanocluster is even used by Haruta himself.[40] The oxidation of CO at ambient temperature (Equation 2.8) is a important reaction for air purification samples and breathing devices. According to Hertiz *et al.*[41] conversion of poisonous carbon monoxide into harmless carbon dioxide, using gold catalysts, could potentially improve the effectiveness of catalytic converters that clean automobile exhaust as well as breathing devices used by miners and firefighters. Industrial catalyst currently used is hopacalite ($CuMn_2O_3$), a catalyst which deactivates quite rapidly.[42] In addition, applications within pollution control, fuel cells, gas sensing, chemical processing (CO oxidation in gas reforming) and air purification samples for long-term space travels have also been reported.[43]

Of all these areas of interest the low-temperature CO oxidation is the performance of car exhaust catalysts is still the area where most research has been devoted to. This is mainly due to the time required to heat the catalyst using the heat from the combustion reaction. The reaction alone is not very relevant for practical applications without other species such as hydrogen and/or water present simultaneously. Although this is a simple reaction considerable research has been performed to obtain information regarding the active sites, reaction mechanism and kinetic parameters.

$$CO + \frac{1}{2}O_2 \rightarrow CO_2 \tag{2.8}$$

In addition to conventional CO oxidation, gold catalysts have been found to oxidize CO in the presence of hydrogen; a reaction commonly known as preferential CO oxidation (PROX). The product from steam reforming contains about 8-10% carbon monoxide, less than 1% being detrimental to the conventially used platinum

based catalysts, thus leading to CO poisoning of the Pt catalysts. By introducing hydrogen to the feed, the CO concentration can be lowered from about 1% to 50 ppm. Several other reactions can occur when operating at PROX conditions, these being:

$$H_2 + \frac{1}{2}O_2 \rightleftharpoons H_2O \tag{2.9}$$

$$Co + 3H_2 \rightleftharpoons CH_4 + H_2O \tag{2.10}$$

$$CO + H_2O \rightleftharpoons CO_2 + H_2 \tag{2.11}$$

Reactions 2.8 and 2.11 are desired since they do not reduce the amount of hydrogen.

In terms of gold catalysts for conventional CO oxidation and PROX, the choice of preparation method of the gold catalyst, pre-treatment method and the selection of support are crucial to obtain small gold nanoparticles (GNPs). According to Chiang *et al.*[44] 3 nm is an optimum GNC size for CO oxidation reaction. In addition, residual impurities, especially chloride ion, can lower the catalytic activity.

Preparation and pre-treatment of gold catalysts

Small GNCs were first obtained by coprecipitation (COPPT) and later by deposition-precipitation (DP).[1,2,9,40,45] Today, DP and Incipient wetness impregnation (IWI) are the most common ways of prepare Au catalysts with respect to CO oxidation.[46] These techniques are often used on oxide supports (two-dimentional), however, Okumura *et al.*[36] have reported of conversion of CO for a Au/HY catalyst prepared with DP. Haruta *et al.*[40] reported that classical impregnation with $HAuCl_4$ as a precursor led to GNCs larger than 30 nm. These materials are proven to be catalytically inactive for CO oxidation. Gold compounds are photosensitive and a trivalent gold precursor may very well be reduced to metallic gold in daylight. Premature reduction can be avoided by performing preparations in the dark (or at least avoid direct daylight) and drying the obtained product at temperatures below 100 °C. It is also recommended to store gold precursor in cold surroundings,

i.e. refrigerators or freezers if possible.

Another variable to stress is the importance of chloride removal by washing. Residual chloride causes agglomeration of the precursor during thermal treatment in air resulting in large GNCs. $HAuCl_4$ is widely used as a precursor for gold catalysts, leaving a certain amount of chloride residue in the catalysts after preparation. Both experimental and theoretical studies have shown that chloride can poison the catalytic performance of gold catalysts for CO oxidation.[47] In addition, chloride can promote the agglomeration of GNCs during heat treatment, thus inhibit the catalytic activity by poisoning the active sites.[48] Chloride weakens the absorption of O_2 and lowers the stability of the CO-O_2 intermediate complex. Calculations show that Cl^- has a long-order character, reaching at least two gold sites away from the absorbed Cl^- atom.[49]

The effect of calcination temperature on the catalytic activity of gold colloids mechanically mixed with TiO_2 for CO oxidation was studied by Tsubota *et al.*[9]. It revealed that the as-synthesized sample showed poor catalytic activity. However, by calcination of the sample at temperatures up to 600 °C the activity increased, even though agglomeration of the metallic gold atoms had occurred. Based on this they suggested that a strong connection between metallic GNCs and the support was necessary to obtain high activity. On the other hand, Hodge *et al.*[10] reported higher activity on uncalcined than for calcined Au/Fe_2O_3. Their study showed high CO conversion for samples containing a mixture of $Au^{\delta+}$(partially charged gold atoms) and Au^0 GNCs, thus suggested that the $Au^{\delta+}/Au^0$ ratio may have an important effect with respect to the catalyst's activity. Daniells *et al.*[50] proposed that high temperature treatment prior to the CO oxidation measurements produced less active samples as a result of the removal of -OH groups and reduction of Au^{3+} to Au^0 nanoclusters.

Selection of support

The cluster size distribution and morphology of GNCs are determined by the choice of support. It mainly depends on the gold diffusion rate whereas the morphology

depends on the interface energy between the gold metal and the support.[51] Transition metal oxides such as ferric oxide and titanium oxide have shown themselves to be good supports, while more commonly used support such as silica and alumina are less efficient.[9,10,34] Zeolites have also been reported as suitable supports, the most used zeolite support being HY.[13,36] One paper has been published on ZSM-5 as a support for gold catalyzed CO oxidation,[52] while no publication has yet been reported on SAPOs as good supports for CO oxidation reactions.

It is strongly suggested that the support is in some manner involved in the reaction. Several reaction mechanisms have been suggested, depending on the manner and extent of the support's involvement. Four main reaction pathways have been suggested;

1. the reaction proceeds only on the metallic gold
2. it requires the simultaneous availability of metallic and cationic gold
3. it involves collaboration between metal and support, with the possible assistance of cationic species, or;
4. it proceeds solely via cationic species on the support.

Size effects

It is hard to distinguish between the effects of cluster size versus metal-support interactions since they are so closely related. Small GNCs have a large fraction of atoms in direct contact with the support surface. However, this increases the fraction of unsaturated surface atoms, thus changing the physical properties of the cluster. Studies have revealed that some of the most active gold catalysts in CO oxidation contain Au^0 clusters with diameters from 2 to 5 nm.[34,53] It is suggested that the optimum GNC size is dependent on the type of support, as illustrated in Figure 2.12.[34]

Supports consisting of $3d$ transition metal oxides allow the GNC size to be larger than 2 nm, while alkaline earth metal hydroxide supports requires GNC sizes

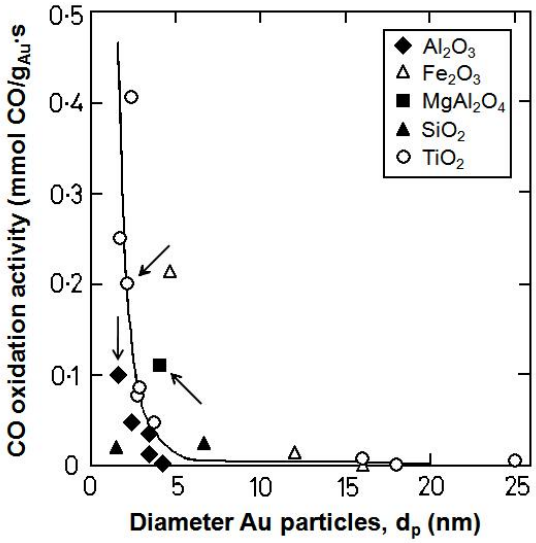

Figure 2.12: Relation between activity and the mean GNC size for CO oxidation[34]

smaller than 2 nm.[34] However, Lopez *et al.*[54,55] suggest that the GNC size alone is the main reason for the conversion of CO to CO_2. Based on density function calculations, they have reported that the CO oxidation rate for GNCs within the size range of 2-4 nm is more than two orders of magnitude larger than what measured for large GNCs (20-30 nm), independent on the support.

The size effects has also been explained by the presence of GNCs with low multiplicities.[54] Lopez *et al.*[54,55] have reported that the multiplicity of the GNCs seems to have considerably more influence on the catalytic activity of CO oxidation than effects due to the support. Based on density calculations they have demonstrated that oxygen and carbon monoxide can adsorb on gold atoms with a multiplicity lower than 8. The fraction of low-coordinated Au atoms depend both on the size and shape of the clusters, hence explains why GNCs of the same size can have different activity on various supports. The adsorption energies for both the O and CO are found to be lowered (stronger bonding) by almost ≈ 1 eV going from Au^{3+} where Au atoms have a multiplicity of 9 to the Au_{10} nanocluster where the most reactive Au atoms have a coordination number of 4. Figure 2.13 illustrates this assumption.[55]

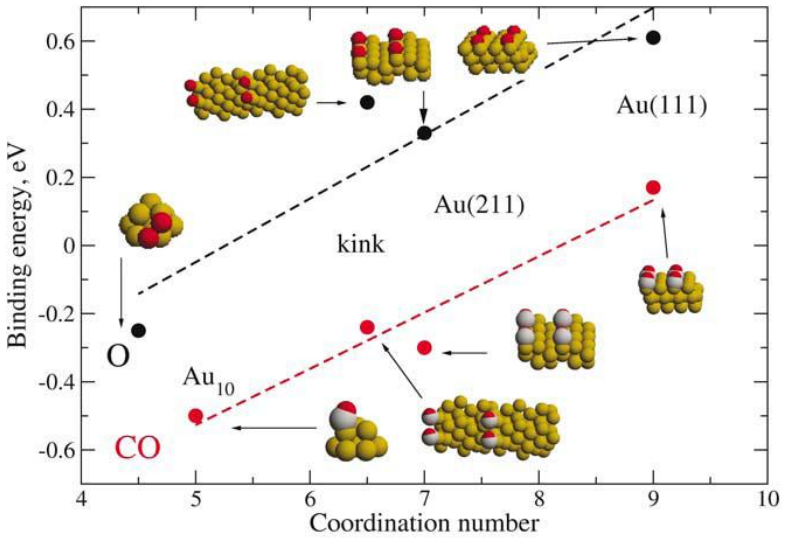

Figure 2.13: The correlation between the binding energies, for CO molecules and O atoms, with respect to the coordination number of Au atoms in a series of environments. Binding energies, in eV, reported are referred to gas-phase CO and O_2, for O_2 the energies are given per O atom[55]

The differences in binding energies for O and CO between Au^{3+} and Au_{10} nanoclusters determine the possible coverage of CO at the support surface, which is important for the ability of the catalyst to oxidize CO. The activation barriers for the surface reactions follows the trend for the bonding energies, i.e. the catalytic activity for small GNPs increases when they are low-coordinated. According to Lopez *et al.*[55] this statement is independent of the support.

2.3 Element analysis[56]

For element analysis Inductively Coupled Plasma Mass Spectrometry (ICP-MS) was used. ICP-MS is a fast and accurate multi-element analytical technique for the determination of elements in liquid and solid samples. The elemental or isotopic ratios are determined by the mass spectrometry (MS) of ions generated in an inductive coupled argon plasma which serves as a source of positively charged analyte ions. The ions are extracted from the environment of the plasma into a high-vacuum enclosure via an interface region containing apertures. The analyte isotopes are separated according to their mass/charge ratio by a mass spectrometer

and are detected and measured by a detector. The sample's elements are detected in μg/g. The content of one specific element (in weight per cent, wt%) can be calculated according to Equation 2.12:

$$wt\% = \left(\frac{\mu g}{g} \cdot 10^{-6}\right) \times 100\% \tag{2.12}$$

2.4 Temperature-Programmed Reduction (TPR)[21]

Temperature-Programmed Reduction (TPR) is an analytical technique used to determine a materials thermal stability and its fraction of volatile components by monitoring the weight change that occurs as a specimen is heated. Measurements carried out in air or in an inert atmosphere, such as helium or argon are referred to as thermogravimetric analysis (TGA). However, the analysis can also be performed in a reducing atmosphere, e.g. a mixture of hydrogen and argon. Measurement performed under these conditions are commonly known as Temperature-programmed reduction (TPR). The weight is recorded as a function of increasing temperature both for TGA and TPR. The loss of water of crystallization or volatiles such as oxygen and templates appears as weight loss, as does decomposition. The weight loss curve gives information about the temperatures where the weight loss is most apparent, i.e. when the main decompositions occur.

TPR is commonly employed in research to determine characteristics of materials, degradation temperatures, absorbed moisture content of materials and their decomposition points. In addition, information regarding the reduction of cationic species can be obtained. During a TPR analysis the hydrogen will reduce the cationic species and hence appear as a peak in the gas chromatography (GC) plot. A mass spectrometer (MS) can also be connected to the exhaust gas of the TPR equipment. A reduction of cationic species will then appear as a drop in the exhaust gas concentration for hydrogen since hydrogen is adsorbed on the support surface.

2.5 Surface area measurements (BET)[57]

The best known method for determination of surface areas of porous solids is the so-called BET method grounded by Brunauer, Emmett and Teller. The method is based on the experimental establishment of the relationship between the pressure of a gas that is in equilibrium with a solid surface and the volume of the gas absorbed at the particular pressure at the surface, i.e. the Langmuir theory based on the kinetic theory of gases. The method assumes that the adsorbent molecules have access to the pore walls within the sample under investigation and that the distance between the walls of a pore is large when compared to the molecular dimensions of the adsorbate. To enable the generalization of the Langmuir theory to multilayer absorption, the BET theory make two assumption with respect to the heat of absorption:

1. It is constant throughout the formation of the first layer of absorbed gas
2. In the second and higher layers is it equal to the heat of liquidation

The BET equation can therefor be given as:

$$\frac{kx}{\nu(1-kx)} = \frac{1}{\nu_c c} + \left[\frac{(c-1)}{\nu_m c}\right] kx \tag{2.13}$$

x is the relative pressure (usually denoted p/p_0), ν is the standard temperature and pressure (STP) volume of the adsorbed adsorbate, while ν_m is the STP volume of the amount of adsorbate required to form a monolayer. c is known as the BET "adsorption coefficient" constant and k is a number smaller than 1. The Langmuir isotherm is usually better for chemisorption and the BET isotherm works better for physical adsorption than for non-microporous surfaces.

2.6 Powder X-ray Diffraction (PXRD)[58]

2.6.1 Theory

X-ray diffraction (XRD) is an analytical technique primarily used for phase and composition identification of a crystalline material and can provide information about unit cell dimensions. The technique is based on constructive interference of monochromatic X-rays with a crystalline sample. The X-rays are generated by a cathode X-ray tube, filtered to produce monochromatic radiation, and directed toward the sample. The interaction of the incident rays with the sample produces a constructive interference only when conditions satisfy Bragg's Law (Equation 2.14).[59]

$$n\lambda = 2dsin\theta \tag{2.14}$$

When a monochromatic X-ray beam with wavelength lambda, λ, is projected onto a crystalline material at an angle theta, θ, diffraction occurs only when the distance traveled by the rays reflected from the successive planes differs by a complete number n of wavelengths, as shown in Figure 2.14. By varying the angle θ, the conditions of Bragg's Law are satisfied by different d-spacing in crystalline materials. Plotting the angular positions and intensities of the resultant diffracted peaks of radiation produces a pattern, which is characteristic for the sample. If a mixture of different phases is present in the material, the resultant diffractogram is formed by addition of the individual patterns.

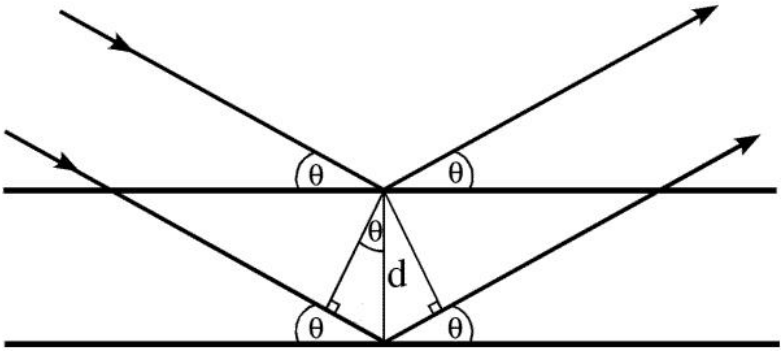

Figure 2.14: Bragg's law

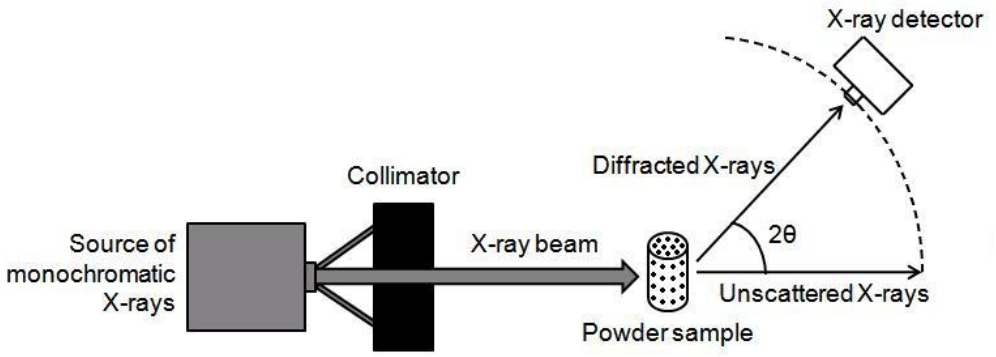

Figure 2.15: Experimental PXRD set-up

A finely grounded crystalline powder contains a very large number of small crystallites oriented at random. When a monochromatic X-ray beam strikes a polycrystalline sample it is scattered in all possible directions. As a result, each plane of atoms separated by different lattice spacing in the crystal, give rise to a cone of diffraction intensity. These cones consist of a set closely spaced dots, representing diffraction of a single crystallite within the powder sample. With a large number of crystallites represented in the sample, these dots join together and form the diffraction cone. The positions of the various diffraction cones need to be determined in order to obtain powder diffraction data. For this a powder diffractometer is used which measures the positions of diffracted beams. By scanning the detector around the sample along the circumference of a circle it cuts the diffraction cones at the various diffraction maxima, thus detecting the intensity of the X-ray as a function of the detector angle, 2θ. The experimental Powder X-ray Diffraction set-up is shown in Figure 2.15.

2.6.2 Data analysis

Data obtained by the XRD experiments are compared with standard line patterns that are available for almost every compound in the *Powder Diffraction File* (PDF), which is provided by the International Center for Diffraction Data (ICDD). The file is annually updated and contains more than 60,000 different crystallographic phases. Experimental data from an unknown sample is therefore compared to the already known standard PDF line patterns. An overlap between

the three most intense characteristic lines from the standard PDF line patterns and those in the unknown sample is sufficiently convincing evidence of the existence of a crystalline phase in the sample.[57]

2.7 X-ray absorption spectroscopy (XAS)[17,60,61]

2.7.1 Introduction

X-ray absorption spectroscopy (XAS) is an element-specific method which gives detailed information about the local structure around the atoms of a specific element. The method is based on absorption of X-rays and the creation of photoelectrons which are scattered by nearby atoms. This gives rise to interference effects that are visible in the XAS spectrum. These effects can provide information about the distance, number and type of neighbors of the absorbing atom. An important feature with this characterization technique is that the method is not limited to the presence of a long-range order in the material, as is the case for other characterization techniques such as PXRD. XAS is therefore a valuable tool for characterization of catalysts since the technique can be used on amorphous materials, small particles, liquid and gases, as well as crystalline materials. A XAS spectrum can be divided into two regions; X-ray Absorption Near Edge Spectroscopy (XANES) and Extended X-ray Absorption Fine Structure (EXAFS).

The XANES region extends from a few eV below the absorption edge to 60 eV above the edge. This region can contain pre-edge peaks which are results of dipole-forbidden $1s \rightarrow 3d$ transitions that are still allowed due to d/p orbital mixing. Since L_{III}-edge XAS spectra of gold compounds do not show any sign of pre-edges, the phenomenon will not be discussed any further in this thesis.

On the other hand, another striking phenomenon called a white line is observed in the XANES region for oxidized gold. The white line is a large peak in the absorption coefficient occurring near the absorption edge. It got its name as it was first detected by X-ray film as a very strong exposure. The intensity of the white line correlated to the number of unoccupied $5d$ orbitals and originated from

the $2p_{3/2} \rightarrow 5d$ transition. The electrons in the L_{III} shell ($p_{3/2}$ state) are allowed to both the $d_{3/2}$ and $d_{5/2}$ states. As the latter is not fully occupied, a white line can be observed in the L_{III}-edge XANES spectrum. For gold foil, with an electron configuration $[Xe]4f^{14}5d^{10}6s^1$, a white line will not be observed due to the complete $5d$ orbital. Trivalent gold, on the other hand, has the electron configuration $[Xe]4f^{14}5d^{8}6s^0$, thus incomplete $5d$ orbital, and a white line will be visible near the absorption edge. The intensity of the white line can be used as a fingerprint for the degree of trivalent gold present in the sample under investigation; the more unoccupied the $5d$ orbital is, the higher the intensity of the white line. L_{III}-edge XAS studies of gold compounds, the white line will have its peak at $\approx$ 11923 eV in the XANES spectra.[4,34,36,62,63]

The EXAFS region starts approximately from 60 eV and continues up to 1000 eV above the edge. A more detailed description of the EXAFS region is given in Section 2.7.2. The XANES and EXAFS regions are illustrated in Figure 2.16.

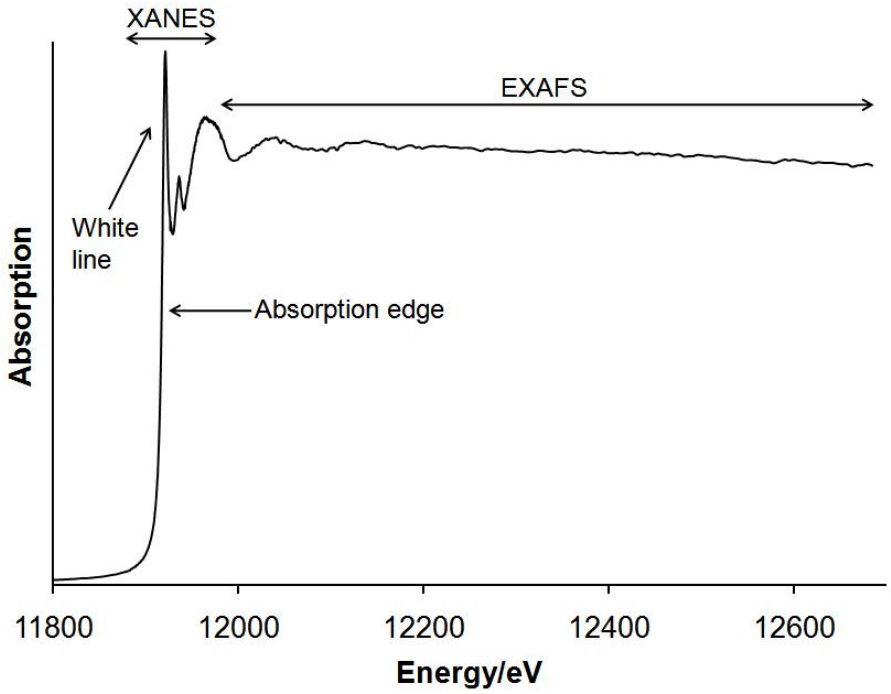

Figure 2.16: Gold L_{III}-edge XAS spectrum for tetraamminegold(III) nitrate

When X-rays hit a sample, an oscillating electric field of electromagnetic radiation is created and interacts with the electrons bonded in an atom. The radiation can either be scattered by these electrons, or absorbed thus excite the electrons. As a monochromatic X-ray beam with intensity I_0 passes through a sample of thickness x, it loses its intensity due to interactions with the sample. The intensity loss depends on which mode the XAS measurement is detected in. The two modes used in this thesis are transmission and fluorescence mode, shown in Figure 2.17.

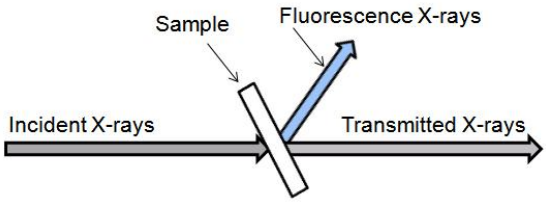

Figure 2.17: Transmission and fluorescence mode used for XAS detection

Transmission measurements are most useful when the absorber in the sample is not diluted, due to the fact that the signal is significantly greater than the background absorption. For diluted samples the signal to noise ratio for transmission mode is low and fluorescence detection is more desirable. The intensity loss leads to the following connection between the incident (I_0) and transmitted (I_t) radiation, and the incident (I_0) radiation and the intensity of the monitored fluorescence line (I_f):

$$ln\frac{I_0}{I_t} = \mu \cdot x \tag{2.15}$$

$$\frac{I_f}{I_0} = \mu \cdot x \tag{2.16}$$

The linear absorption coefficient, μ, depends on the types of atoms and the density, ρ, of the material. At certain energies, where the absorption increases significantly, absorption edges will appear in the spectrum. Each edge occurs when the energy of the incident photons is just sufficient to cause excitation of a core electron of the absorbing atom to a continuum state, i.e. to produce a photoelectron. The energies of the absorbed radiation at these edges correspond to the binding energies of electrons in the K, L, M, etc, shells of the absorbing elements. The absorbing edges are labeled in the order of increasing energy, K, L_I, L_{II}, L_{III},...,

corresponding to the excitation of an electron from the $1s$, $2s$, $2p_{1/2}$ and $2p_{3/2}$ orbitals (states) respectively.

2.7.2 EXAFS theory[17,60,61]

EXAFS is a unique characterization technique for a various number of both crystalline and amorphous materials, e.g. solids, liquids and gases. The EXAFS region provides structural information about neighboring atoms (B) in the three dimensional environment surrounding the central atom (A). By analyzing the oscillating fine structure that occurs beyond the absorption edge, information such as the number of neighbors (multiplicity) and their bonding distances to the central atom can be obtained. The sudden large increase in absorption is commonly known as the absorption edge. The absorption occurs when the energy of the incident X-ray photon (E=$h\nu$) is greater than threshold energy (E_0) of the absorbing atom required to photoeject the absorbing atom's $1s$ electron. With respect to gold, the threshold energy for the L_{III}-edge is $\approx$ 11919 eV.

After absorption, a photoelectron with kinetic energy E_k=(E-E_0) is emitted from the core and can be represented a by spherical wave spreading from the absorber (A). When the spherical wave collides with the neighboring atoms (B), the wave is backscattered and produces incoming waves that interfere with the outgoing wave creating constructive or destructive interference depending on the photoelectron wave length, λ_e, and the nearest neighboring distance between (A) and (B), denoted $R_{A\cdots B}$. The process is illustrated in Figure 2.18. The absorbing and backscattering atom do not have to be elements with different atomic masses (Z), and in metals were $Z_A \approx Z_B$, the absorbing atom (A) can also act as a backscattering atom.

The interference produces a corresponding modulation in the absorption cross section, recognized as the ripples in EXAFS region. The amplitude and frequency of the interfering individual sine waves, and the factors that affect them, define the EXAFS. Thus, the modulation of μ and E depends on type of neighboring atoms and their bonding distances to the absorber. Constructive interference increases

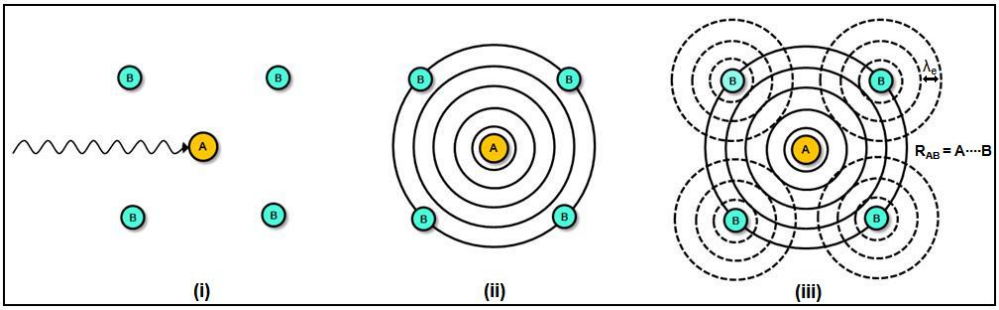

Figure 2.18: *(i)* An incident X-ray photon with energy (E=hν) greater than the threshold energy of the absorbing atom (A) is absorbed; *(ii)* A photoelectron with kinetic energy E_k=(E-E_0) is emitted and can be represented by a spherical wave spreading out from the absorber; *(iii)* The outgoing photoelectron wave is backscattered by the neighboring atoms (B) and produces incoming waves that interfere with the outgoing wave creating constructive and destructive interference

the absorption coefficient while destructive interference decreases it. The EXAFS signal also contains information regarding thermal and structural disorder as these factors have a dampening effect on the amplitudes of the oscillation.

Extraction of structural information

Extraction of structural information from EXAFS is a multistep procedure that involves considerable data refinement. The first step involves extracting the EXAFS fraction of the XAS spectrum. This extraction is termed χ. Further, the energy scale (eV) used in the XAS spectrum is usually converted to the photoelectron wave vector scale (Å^{-1}) and $\chi(k)$ is weighted by k^{n-1} (n= 2, 3, 4) to offset the rapid decaying EXAFS oscillations. $\chi(k)$, known as *chi*, is defined as the sum of individual sinusoidal components created by the backscattering from different coordination shells. The frequency of these components depends primarily on $R_{A\cdots B}$. Fourier Transform of *chi* produces a spectrum called Pseudo Radial Distribution Function (PRDF). The peaks in the PRDF correspond to the radial coordination shells. The radial positions are shifted slightly to lower R from the actual $R_{A\cdots B}$, thus named pseudo distances. Information regarding the local environment surrounding the central atom can be obtained from the PRDF, yet another analysis step is required to obtain quantitative structural information. This step is known as Fourier Filtering, which transforms the PDRF back into k space producing a

single shell $k^{n-1}\chi(k)$. The main data refinement steps are illustrated in Figure 2.19.

The data reduction and analysis of the EXAFS are essentially the same whether $\mu(E)$ is collected in transmission or fluorescence mode. At energies ≥ 60 eV above the absorption edge and at moderate thermal or static disorders the EXAFS signal has to be normalized to the background absorption, μ_0. This normalized fraction of the absorption spectrum, $\chi(E)$ is given by

$$\chi(E) = \frac{\mu(E) - \mu_0(E)}{\mu_0(E)} \tag{2.17}$$

where $\mu(E)$ is the measured absorption at a given X-ray wave length and $\mu_0(E)$ is the smooth absorption that would be observed at the same wave length is no EXAFS structure was present, i.e. an isolated atom. $\mu_0(E)$ cannot be measured experimentally since it is physically impossible to isolate the sample atom in space. It is therefore numerically approximated by a smooth line during background removal procedures. Equation 2.18 is applied to convert $\chi(k)$ from the energy scale (eV) into a function of the photoelectron wave vector k (Å^{-1}):

$$k = \sqrt{\frac{2m}{\hbar^2}(E - E_0)} \tag{2.18}$$

m is defined as the mass of the electron, $\hbar$ is the reduced Plack's constant and E-E_0 is the ejected electron's kinetic energy. Converting $\chi(E)$ to $\chi(k)$ using Equation 2.18 requires that E_0 is know. Usually, it is impossible to determine the exact position of E_0 in the spectrum, but small errors are not catastrophic and an arbitrary choice near the edge can be corrected during data refinements. A more detailed description of data analysis is given in Section 2.7.4.

The EXAFS equation

The EXAFS equation (Eq. 2.19) is a theoretical expression describing $\chi(k)$ in terms of structural parameters and allows structural information to be derived from the experimental $\chi(k)$. Derivation of the EXAFS equation is based on a plane wave single scattering approximation and was formulated in the 1970s by Sayers, Stern and Lytle.[64,65] The plane wave theory assumes the atomic radii to

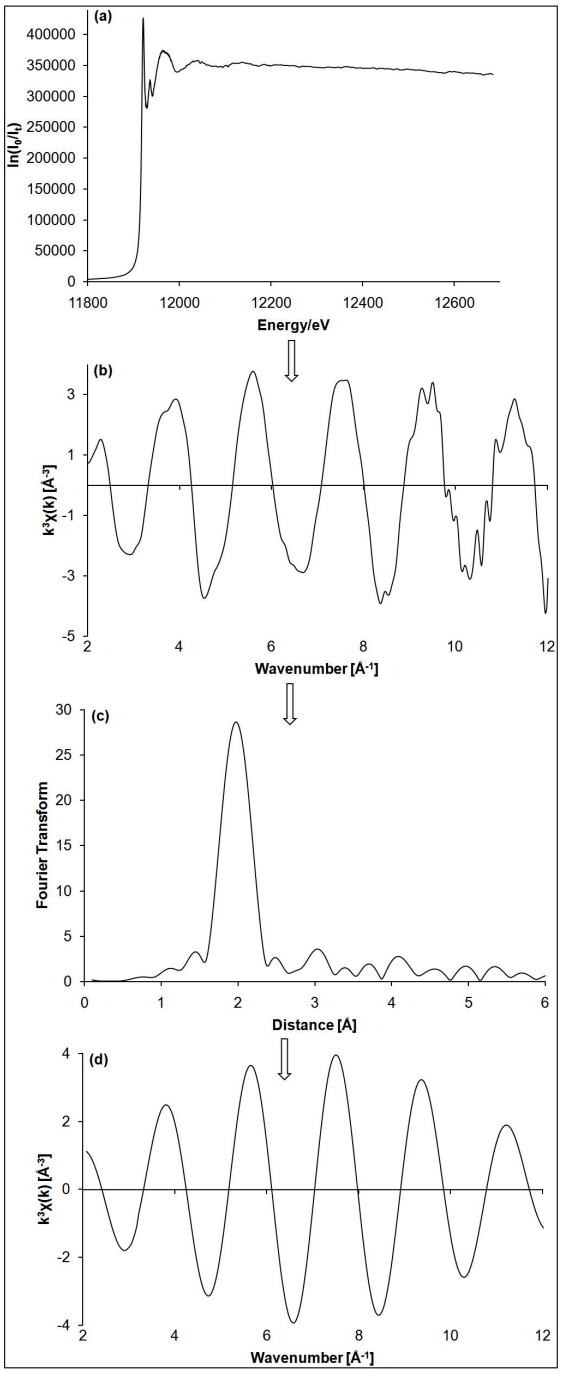

Figure 2.19: Major stages of EXAFS analysis of tetraamminegold(III) nitrate; (a) Au L_{III}-edge XAS: (b) extracted $k^3\chi(k)$ spectrum; (c) Fourier Transform spectrum (PRDF) and (d) Fourier Filtering of the first Au-N shell

be much smaller than the interatomic distance, i.e. that the incoming or backscattered photoelectron waves can be approximated by plane waves. By ignoring the curvature of the photoelectron wave the EXAFS equation is greatly simplified. The single scattering approximation assumes the outgoing wave function to only be backscattered once from the neighboring atoms before interfering with the unscattered wave. The approximation is valid when the scattering is small, but for some geometries additional scattering between the neighboring atoms have to be considered. This is why the EXAFS equation is commonly known to be valid only for K-edges. However Teo *et al.*[66] state that it adequately describes L_{III}-edges within experimental errors.

$$\chi(k) = \sum_{j}^{shell} N_j \underbrace{S_i(k)}_{\text{Red.fac.}} \times \underbrace{F_j(k)}_{\text{Backsc.amp.}} \times \underbrace{e^{-2\sigma_j^2 k^2}}_{\text{Th./st.damping}} \times \underbrace{e^{\frac{-2r_j}{\lambda_j(k)}}}_{\text{Inel.scatt.}} \times \underbrace{\frac{sin(2kr_j + \phi_{ij}(k))}{krj^2}}_{\text{Total phase}} \tag{2.19}$$

i and j refers to the absorber and the backscatter, respectively. N_j denotes the number of backscattered atoms in the j^{th} coordination shell, i.e. the multiplicity. $S_i(k)$ defined as the amplitude reduction factor due to many body effects on the absorber i, $F_j(k)$ is the backscattering amplitude from an atom in the j^{th} coordination shell, while σ_j^2 is the Debye-Waller factor that accounts for the thermal vibration and static disorder for the j^{th} backscatter. $e^{\frac{-2r_j}{\lambda_j(k)}}$ denotes the inelastic loss due to the scattering process of neighbor atoms or the medium between. λ is the photoelectron mean free path. The last variable, ϕ_{ij}, is the total phase shift experienced by the photoelectron. These variables will be discussed in more detail below. To simplify, the EXAFS equation is in essence the sum of modulated sine waves of varying frequencies originating from each backscattering coordination shell. By combining the numerous variables in Equation 2.19 the general form of the EXAFS equation is obtained:

$$\chi(k) = \sum_{j}^{shell} A_j(k) \times sin\left(2kr_j + \varphi_{ij}(k)\right) \tag{2.20}$$

where $A_j(k)$ is the total backscattering amplitude of the j^{th} coordination shell and

$sin(2kr_j+\varphi_{ij}(k))$ is the corresponding total phase.

Weighting

When *chi*, $k^n\chi(k)$, is obtained through data refinements of the EXAFS region it is often weighted to offset the rapidly decaying EXAFS oscillation. The weighting factor, k^{n-1} where $n = 1, 2, 3, 4$, roughly compensates for the combined damping effect of the total backscattering amplitude, $A_j(k)$, at high k-values. Thus, helps to prevent the first shell backscatters from higher dominating ones. The choice of n is a crucial step in the data refinement. Normally, k^2 or k^3 weighting is preferred due the higher contribution from the metal present in the investigated sample. Figure 2.20 represents weighted $k^1\chi(k)$, $k^2\chi(k)$ and $k^3\chi(k)$ of tetraamminegold(III) nitrate. The figure clearly illustrates that k^3 weighting gives the highest amplitude for the sinusoidal curve, thus makes it easier to refine.

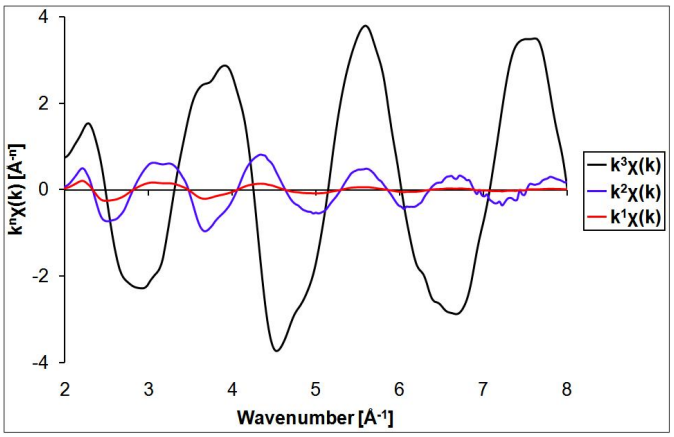

Figure 2.20: $k^1\chi(k)$, $k^2\chi(k)$ and $k^3\chi(k)$ of tetraamminegold(III) nitrate

Phase

The total phase of the backscattered photoelectron wave at the core, $2kr_j+\varphi_{ij}(k)$, can be considered as consisting of two parts. The first part is a result of the photoelectron traveling a distance $2r_j$ from the absorber to the backscatter and back to the absorber again. The number of wave lengths this distance correspond to is $\frac{2r_j}{\lambda_e}$, where the photoelectron wavelength corresponds to its kinetic energy, E_k.

The phase is therefore given by:

$$2\pi \times \frac{2r_j}{\lambda_e} \Longrightarrow 2kr_j \tag{2.21}$$

where $k = \frac{2\pi}{\lambda_e}$.
The second contribution, $\varphi_{ij}(k)$, arises as a result of interactions between the backscattering photoelectron and the potential of the scattering pair. This results in additional phase changes when the photoelectron wave is emitted from the central atom, backscattered from the backscatter and when it arrives back at the central atom. $\varphi_{ij}(k)$ generally accounts for $\approx 10\%$ of the total phase. However, it is still necessary that $\varphi_{ij}(k)$ is known to determine the nearest neighboring distance with a better accuracy than ± 0.1 Å. When $\varphi_{ij}(k)$ is determined either experimentally or theoretically, it is substracted from the total phase of the sample under investigation to obtain the exact nearest neighbor distances from the $2kr_j$ fraction of the total phase;

$$\underbrace{(2kr_j + \varphi_{ij}(k))}_{\text{Total phase}} - \underbrace{\varphi_{ij}(k)}_{\text{2nd contribution}} = \underbrace{2kr_j}_{\text{1st contribution}} \tag{2.22}$$

As mentioned above, the peaks in the PRDF experiences a shift away from their true values, thus named pseudo distances. This is due to the influence of the additional $\varphi_{ij}(k)$ phase term to $2kr_j$.

Amplitude

The total amplitude, denoted $A_j(k)$ in Equation 2.20 is a function of the backscattering amplitude, $N_j F_j(k)$ from all the neighboring atoms in the j^{th} coordination shell. The total phase is reduced by the Debye-Waller factor, σ_j^2, the amplitude reduction factor, $S_i(k$, and inelastic losses, $e^{\frac{-2r_j}{\lambda_j(k)}}$, in the scattering process. It is a function of the interatomic distance, $\frac{1}{r^2}$, thus the EXAFS signals are drastically reduced the longer $2r_j$ is. As a result, EXAFS only yield structural information about the nearest coordination shells located $\approx$ 1-5 Å from the central atom. The backscattering amplitude function, $F_j(k)$, is only a function of the backscatter and

not the absorber. The amplitude of $F_j(k)$ at high k-values is generally increasing with increasing atomic number (Z). Thus, the position of the amplitude moves to higher k-values as the atomic number of the backscatter increases. However, only atoms with sufficiently different Z can be distinguished, hence differentiating between neighboring atoms in the periodic table is hard with EXAFS.

The other variables that constitute $A_j(k)$ account for the physical effects that influences the backscattering amplitude, $F_j(k)$. The reduction factor, $S_i(k)$, represents the losses in $F_j(k)$ caused by multiple excitation of the absorber from processes known as *shake-up* and *shake-down*. Multiple excitations originate at the absorbing atom, where excitation of other electrons occur during the photoelectron excitation process. These electrons are excited to either bond states (*shake-up*) or to continuum states (*shake-down*). The latter case occurs when the propagating photoelectrons have a lower kinetic energy, E-E_0, than in Equation 2.18. The multiple excitations absorb energy, thus reduces the intensity of the primary photoelectron excitation. According to Stern *et al.* the amplitude backscattering factor can be reduced by a factor of two as a consequence of the multiple scattering[67]. $S_i(k)$ can be hard to estimate and is usually ignored when standard compounds closely similar to the sample under investigation are used as references in the analysis. This assumes that $S_i(k)$ is similar for both the standard compound and the sample under investigation, thus cancel each other out in the data analysis.

The factor for inelastic scattering, $e^{\frac{-2r_j}{\lambda_j(k)}}$, also reduces $A_j(k)$. The term is related to the finite lifetime of the excited state and approximated by the photoelectron mean free path. Inelastic scattering is dominated by loosely bound electrons and is sensitive to the chemical environment. As for $S_i(k)$, the effect is assumed to cancel when standard compounds closely similar to the sample under investigation are used for analysis.

Debye-Waller factor

The Debye-Waller factor, σ_j^2, accounts for the variations in the interatomic distance, r_j, due to thermal (vibrational) and static disorder. The vibrational motions

and static disorder from the backscatter cause an additional damping of the EXAFS amplitude. This is especially the case at high k-values. Assuming that the vibrational motion is harmonic and the static disorder is a Gaussian distribution of r_j, the Debye-Waller factor is given by Equation 2.23. These assumptions are valid for samples with low disorder.

$$\sigma^2 = \sigma^2_{vib} + \sigma^2_{stat} \tag{2.23}$$

where σ^2_{vib} and σ^2_{stat} is the thermal and static disorder contribution, respectively. Only σ^2_{vib} is temperature dependent, thus the two contributing factors in the Debye-Waller factor can only be separated by studying σ^2_j as a function of temperature. For sample with high degree of disorder or nonharmonic vibration, the Debye-Waller approximation is not valid and can lead to an incorrect structural result.

2.7.3 Experimental set-up[61,68,69]

Synchrotron radiation has been used to obtain the the XAS data included in this thesis. Synchrotron radiation is generated when charged particles are accelerated in a curved path or orbit. Compared to conventional X-ray sources such as X-ray tubes and rotating anodes, synchrotron radiation are hundreds of thousands times higher in energy. It is extremely intense, highly collimated and it is emitted with a wide range of energies allowing a beam of any energy to be produced. The high flux greatly improves the signal to noise ratio which reduces the acquisition time to 30 minutes compared with days as is the case with conventional X-ray sources. The high flux is important when the element of interest is present in low concentrations in the investigated sample. Since a typical XAS spectrum covers 1000 eV a broad spectral range at uniform flux is required. An XAS experiment requires not only an intense and uniform flux, but also high stability in the flux, energy and beam position. To accelerate the charged particles normally a synchrotron ring with bending magnets is used. Wigglers can be used instead of bending magnets, which results in higher X-ray intensities, yet, over a much smaller energy scale. As the electron passes through the bending magnets/wigglers and insertion devices they emit photons tangentially to the source. A set of horizontal and vertical beam collimators define the synchrotron radiation beam cross section, as illustrated in

Figure 2.21. The beam collimators narrows the beam cross section down to 10× 1 mm^2.

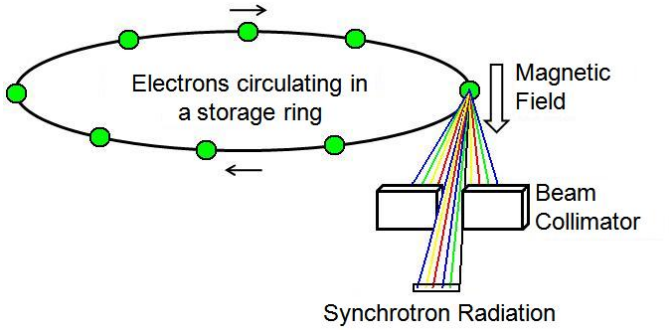

Figure 2.21: Optimization of the synchrotron radiation using beam collimators

Further, the polychromatic X-rays are sent through a crystal monochromator to select a wavelength as it is stepwise moved to scan the desired energies. The monochromator usually consists of silicon single crystal cuts and selects a distinct and narrow wavelength interval following Bragg's law (Equation 2.14). To reject higher harmonics a focusing mirror is used before the monochromatic X-ray beam is sent to the experimental section where the absorption by the sample under investigation is measured as a function of photon energy. The experimental stations (hutches) are usually placed on bending magnets as the photon fan produced supply a high and uniform flux over a large energy range. Figure 2.22 illustrates the process.

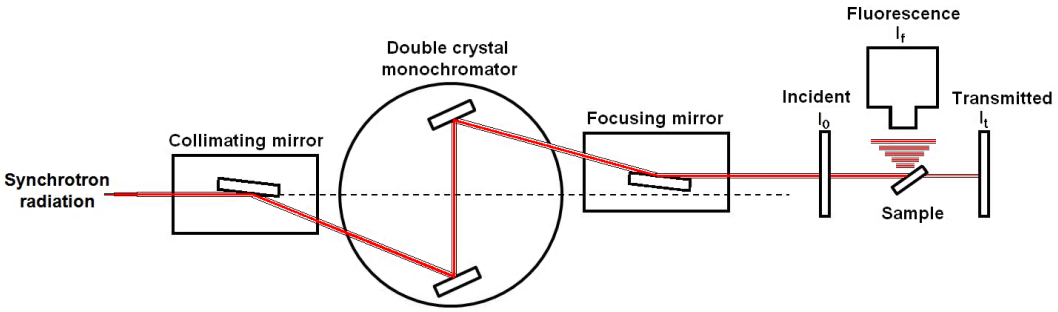

Figure 2.22: Experimental XAS set-up

To detect X-ray photons ionization chambers are often used. They are filled with

gas mixtures where the incoming X-rays will ionize the gas molecules, thus producing electrons caused by a drop in voltage upon hitting the ion chambers' anode. The voltage drop is used to monitor the photo-ion current and can be correlated to the intensity. EXAFS can be measured in both transmission and fluorescence mode (Eq. 2.15 and Eq. 2.16). In transmission mode the linear absorption coefficient (μ) is measured by monitoring the incident (I_0) and transmitted (I_t) radiation. For fluorescence mode the incident (I_0) radiation and the intensity of the monitored fluorescence line (I_f) are measured. As illustrated in Figure 2.22, the cell containing the sample under investigation is penetrated by the X-ray beam at an angle of 0° when transmission mode is used. For fluorescence detection, the cell is located at 45° to the incoming X-ray beam. Fluorescent radiation is measured by an electrode as photoelectron current. The fluorescent radiation from the sample surface is sent upon a Z-1 filter; Z being the atomic number of the absorber, to remove scattered radiation.

2.7.4 Data reduction and data analysis[70,71]

Extraction of structural information from EXAFS is a time-consuming procedure which involves a great deal of data refining. The EXAFS data in this thesis has been refined using the data programs IFEFFIT (Athena)[70] and Excurve software developed by the Daresbury laboratory.[71] Athena is a background removal program, also used for E_0 settings, pre- and post-edge fitting, linear combination and peak fitting.

Athena[70] uses the Autobk algoritm[72] to determine the background absorption and normalize the raw μ(E) data from XAS data collection. The procedure is shown in Figure 2.23. The Autobk equation subtracts the background absorption (μ_0 in Eq. 2.17) by determining an empirical background spline based on a distinction between data and background in terms of Fourier components. For edge step normalization, the difference between μ(E) and μ_0(E) is divided by an estimation of $\mu_0(E_0)$. A line is regressed to the data in some regions below the edge and subtracted from the data. Further, a quadratic polynomial is regressed to the data in some regions above the edge and extrapolated back to E_0. The extrapolated value

of the post-edge polynomial at E_0 is used as a normalization constant. These two regressions are controlled by the pre-edge range and normalization range parameters in Athena[70]. The edge value, E_0, is determined manually as the first large peak in the first derivative spectrum.

Spurious points (glitches) that lie far above or far below surrounding points can be removed manually from the data by plotting χ^n(k) in Athena[70]. Glitches normally arise from the monochromator due to crystal defects or bad tuning. It is often found at the same place in different scans. At high k-values the amplitude of the EXAFS ripples decreases, resulting in noisy and distorted signal. Athena[70] allows truncation of data point after a set values, hence making it easy to remove noisy ranges of the XAS data.

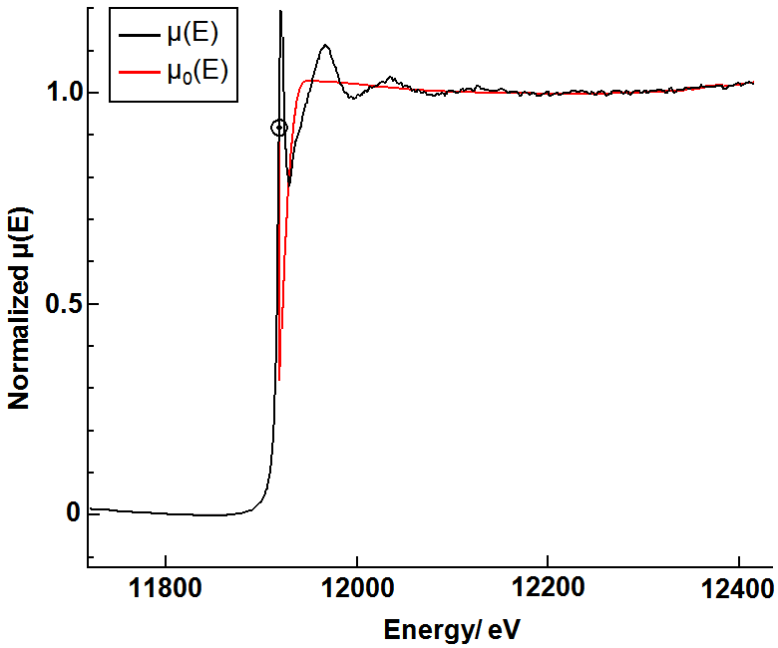

Figure 2.23: Background removal in Athena[70] where μ_0(E) is illustated as a smooth line

Linear combination involves fitting of standard XANES spectra to unknown XANES spectra. These fits can be carried out using normalized μ(E) spectra or k$^n\chi$(k) spectra. Each standard spectrum is interpolated onto the energy grid of the unknown when the fit is performed as normalized χ(E). Normally, the fit is performed over a data range starting at $\approx$ 20 eV below the absorption edge and ending $\approx$

20-50 eV above the edge. The quantity of fit is given by the R-factor;

$$R = \frac{sum\left((data - fit)^2\right)}{sum\left(data^2\right)} \tag{2.24}$$

where sums are over the data points in the fitting region. An example of a linear combination analysis is given in Figure 2.24.

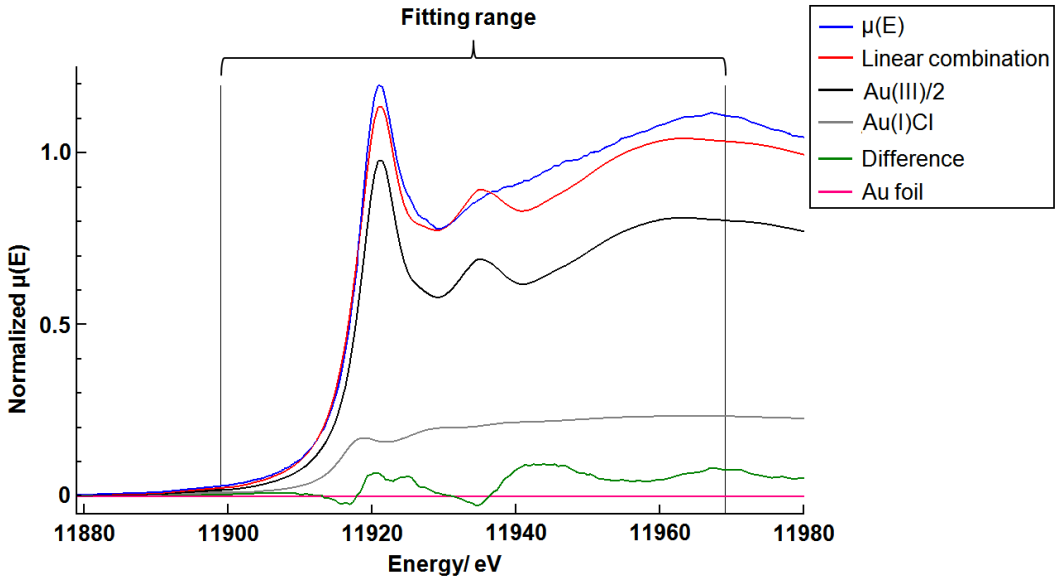

Figure 2.24: Linear combination of Au(III)/2:SAPO-34 with trivalent, monovalent and metallic gold reference compounds

Fitting of peaks (e.g. pre-edges or white lines) to standard XANES spectra is possible in Athena[70]. An arctangent function is used to model the step portion of the data and Gaussians are used to model the features of the XANES spectra. The step function is centered at the absorption edge (E_0) for the data group. The energy value for the centroid is picked manually in the normalized spectrum. Commonly, fitting an interval ranging from $\approx$ 20 eV below the absorption edge to $\approx$ 20 eV above the edge is chosen. The fitting result returns the area under the peak given by the amplitude and width of the area, in addition to the quantity of fit (R-factor, calculated as described in Eq. 2.24). All values are given in eV. Figure 2.25 illustrates a peak fitting procedure performed in Athena[70].

Athena[70] is used to convert χ(E) to the photoelectron wave scale ($\chi(k)$, $Å^{-1}$) by

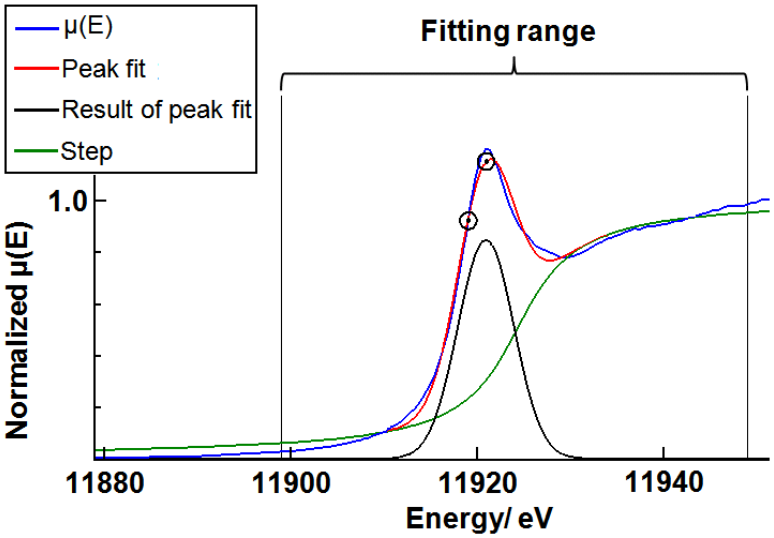

Figure 2.25: Peak fitting of Au(III)/2:SAPO-34's white line

Equation 2.18. $\chi(k)$ is defined as the sum of individual sine waves arising from the backscattering from different coordination shells surrounding the central atom. The frequency of the sine waves depends on the nearest neighbor distance for the coordination shells, $R_{A...B}$. Fourier Transform makes it possible to separate the different frequencies of the sine waves. The signal is transformed into a FT modulus peak, resulting in Gaussian distributed peaks in r-space where the center of the peaks correspond to the distance between the absorbing central atom and the coordination shell.

The phase shift has to be accounted for to make the Fourier Transformation possible. Quantitative structural information such as interatomic distances, Debye-Waller factors and the type of nearest neighboring atoms can be obtained. The heights of the FT peaks depend on the amplitude parameters while their positions depend on phase parameters. To obtain a good resolution of the FT peaks the selection of the k-range is essential. By choosing a too narrow k range one can experience a partial or total overlapping of peaks, resulting in errors in the structural information that is obtained during data refinement. The k-range is selected by the $W(k)$ factor in Equation 2.25. By setting the data to zero at k_{min} and k_{max} the window function, $W(k)$, minimizes distortions and avoids ripples in the FT

modulus.

$$W(K) = \frac{1}{2}\,(1 - cos2\pi)\,\frac{k - k_{min}}{k_{max} - k_{min}} \tag{2.25}$$

The purpose of the EXAFS analysis is to extract structural information such as interatomic distances, number of neighboring atoms (mulitiplicity) and thermal vibration (Debye-Waller factor) for each coordination shell surrounding the central atom. Excurve[71], developed by the Daresbury laboratory, has been used to obtain the desired parameters. The program involves least square fitting of a theoretical model ($\chi_{th}(k)$) to the experimental spectrum ($\chi_{exp}(k)$). The theoretical model is based on a plane wave single scattering approximation, described by the EXAFS equation (Eq. 2.19). The plane wave scattering approximation assumes that the wave in front of the photoelectron is plane, i.e. the interatomic distance being much larger than the atom radius of the backscatter. In order to extract structural information, the parameters in the EXAFS equation (Eq. 2.19) have to be known.

The phase, φ, and backscattering amplitude, $F_j(k)$, can be calculated using the Hedin-Lundqvist formalisn, known as the variable for inelastic scattering, $e^{\frac{-2r_j}{\lambda_j(k)}}$, in the EXAFS equation (Eq. 2.19). The amplitude reduction factor, $S_i(k$, known as AFAC in Excurve[71] is approximated by the Hedin-Lundqvist potential. The total phase is represented by three correlated functions; the multiplicity, N, the Debye-Waller factor, $2\sigma^2$, and AFAC. Thus, the three variables cannot be refined simultaneously. AFAC is determined using a model with known structure (i.e. N is known) and transferred to the analysis of the sample under investigation.

To offset the rapidly decaying EXAFS oscillation at high k-values, $\chi(k)$ is weighted with a weighing factor k^{n-1}, where n= 1, 2, 3, 4. The weighing can result in oscillations with large amplitudes dominating over small ones, thus affecting the interatomic distances. The power of the weighting, n, depends on the atomic number of the backscatters. All gold spectra in this thesis is k^3 weighted, i.e. n= 4. The EXAFS sine waves can be separated by Fourier transforming the $k^n\chi(k)$ from k-space to r-space. Each peak in the Fourier Transform (PRDF) represents

a coordination shell, thus giving a representation of the local environment surrounding the central atom. The Fourier Transform can be analyzed qualitatively by Fourier Filtering. Fourier filtered spectra should not be refined, however, it can act as guidance in the identification of the backscatter atom. The EXAFS analysis in this thesis involves Fourier Filtering of all the gold data from 1.5-25 Å to remove the low frequency below 1 Å. This does not remove any noise or smooth the spectra.

The fit factor, R, given in per cent, represents the goodness of fit between experimental data and the theoretical refinement. It is given by;

$$R_{exafs} = \sum_{i}^{N} \frac{1}{\sigma} \left(\left| \chi_i^{exp}(k) - \chi_i^{th}(k) \right| \right) \times 100 \tag{2.26}$$

By increasing the parameters in the refinement, the fit factor can be improved. However, the model has to be chemically valid and not just mathematically; i.e. the number of refined parameters has to be less than the number of independent parameters, N_{ind}:

$$N_{ind} = \frac{2\Delta r \Delta k}{\pi} + 2 \tag{2.27}$$

Δk represents the k range while Δr is the distance to the coordination shell that is being refined.

Some of the parameters are highly correlated and have to be considered during data analysis. This is the case for: *(i)* the multiplicity, N, and Debye-Waller factor, $2\sigma^2$, and *(ii)* the interatomic distance, r, and E_0 correction, recognized as E_r in Excurve[71]. These combinations of correlated parameters, describing the amplitude and frequency of the EXAFS sine wave, depend on the weighting scheme.

2.7.5 Limitations to EXAFS

Although XAS is reckoned as a brilliant characterization technique for a large range of samples it has its disadvantages. Unlike powder X-ray diffraction (PXRD) XAS does not provide information on long range order in crystalline solids. XAS has a limited resolution, thus making it difficult to separate bonds with lengths. It also has a higher sensitivity to disorder. In principle, all elements can be characterized by XAS, but limitations within the experimental energy ranges can cause some problems. These depend on the flux distribution of the particular synchrotron source and type of monochromator used in the experiment. Soft X-rays at 2500 eV and lower energies are absorbed by air, i.e. elements with K- and L-absorption edges below 2500 eV, are often hard to characterize using XAS. This limitation includes elements such as carbon, nitrogen, oxygen, aluminum and phosphorous.

As mentioned in Section 2.7.2, EXAFS only yield structural information about the nearest coordination shells located 1-5 Å from the central atom. As a consequence, atoms in coordination shells located at longer bonding distances from the core can be hard to determine. In addition, peaks located within the desired r-values (1-5 Å) tend to overlap if their bonding distances are too similar, hence come into view as one peak in the Fourier Transform. It is also difficult to separate elements with similar atomic mass (Z). The EXAFS data are normally refined over a wide k-range to detect as much structural information as possible. At high k-values the amplitude of the EXAFS sine waves decreases resulting in a noisy signal. This affects the refinement result by decreasing the fit factor, R, which represent the goodness of fit between the theoretical model ($\chi_{th}(k)$) and the experimental spectrum ($\chi_{exp}(k)$). The standard derivation of bonding distances are ± 0.01 Å for small r-values and ± 0.04 Å for r-values exceeding 3 Å. The derivation of $2\sigma^2$ is $\pm 20\%$.

Another important limitation to stress is the multiplicities, N, detected with EXAFS. The multiplicities are often used to determine the size of the particles and/or clusters present in a sample. The result obtained from EXAFS does not give an exact size distribution of the particles or clusters, but an average of all single sites

probed by EXAFS. Small particles and clusters are identified by having a lower multiplicity than what known for the bulk, due to a high fraction of surface atoms.

2.7.6 Applications in catalysis; in-situ measurements

Today, most catalysts used for a wide variety of industrial processes are metal on support systems (denoted metal/support). As mentioned in Section 2.1 and Section 2.2.5 zeolites, zeotypes and different metal oxides are known as suitable supports. One of the biggest challenges in the field of catalysis is to determine the roles of both the metal and the support. In some systems the metal is known to activate the catalytic reaction, whereas the support or the metal-support interaction is known to be crucial for the activation of other catalytic systems.

X-ray absorption spectroscopy (XAS) is considered a well suited technique for studying catalytic systems. XAS is extremely versatile in terms of the nature of the sample and the experimental set-up allows for the use of in-situ cells in which both temperature and gaseous environments can be altered to simulate "real working conditions" of a catalyst. The conditions for the in-situ measurements carried out in this thesis is described in Section 3.7.2.

Chapter 3

EXPERIMENTAL

This chapter will describe the synthesizes of the zeotypes SAPO-34, gold incorporated AuSAPO-5, and the gold complex tetraamminegold(III) nitrate, in addition to the ion-exchange methods used to introduce gold cations to the zeolites ZSM-5 and HY, and the zeotype SAPO-34. Further, the various experimental aspects of the characterization techniques applied to investigate the samples will be described.

3.1 Synthesized samples

3.1.1 AuSAPO-5

AuSAPO-5 was synthesized by modifying the method of Lok *et al.*[31]. Ortho phosphoric acid (H_3PO_4, 85%, 19.55 g, Merck) was mixed with deionized water (H_2O, 97 g) and stirred for 10 minutes before gold(III)chloride hydrate ($HAuCl_4$, 0.2279 g, Sigma-Aldrich) was added to the mixture. The mixture obtained a yellowish color and the pH was measured to 0-1. Pseud (Boehmite) (AlOOH, 10.25 g, Sasol) was added and the mixture was set for stirring for 2.5 hours, before adding tetraethylammonium hydroxide, TEAOH ($(C_2H_5)_4NOH$, 35%, 50.49 g, Sigma-Aldrich). After another half hour of stirring Ludox AS-40 (40% SiO_2, 6.0 g, Sigma-Aldrich) was added as the final ingredient. pH was measured to 3- 4 and the color was still yellowish. The molar composition was 0.033 Au : 0.3 Si : Al : P : 0.6 TEAOH : 30 H_2O. The mixture was transferred to autoclaves, and heated in oven for 24 hours

at 150 °C. After heating the mixture was washed and centrifuged with deionized water. The obtained product was dried in oven for 24 hours at 100 °C. The obtained powder had a purple color.

A part of the sample was calcined to remove water and template from the pores. The calcined procedure was carried out by heating the sample in air from room temperature to 550 °C at a heating rate of 1 °C/min, followed by an isothermal step at 550 °C for 17 hours. The calcined sample withheld its purple color.

3.1.2 SAPO-34

The zeolite SAPO-34 was prepared by modifying the method of Lok *et al.*[31]. Ortho phosphoric acid (H_3PO_4, 85%, 15.41 g, Sigma-Aldrich) was mixed with deionized water (H_2O, 36.7 g) and stirred for about 10 minutes after which Al- isopropoxid ($C_9H_{21}AlO_3$, >97%, 27.212 g, Sigma-Aldrich) was added to the mixture. The resulting gel was very viscous and had to be stirred by hand for about 15 minutes before the stirring could be done by a magnetic bar again. The white gel was stirred for another hour until it appeard homogeneous. Ludox-LS (colloidal SiO_2, 30 wt%, 4.00 g, Sigma-Aldrich) was added to the mixture, and the pH was measured to be 3. Tetraethylammonium hydroxide, TEAOH ($(C_2H_5)_4NOH$, 35%, 49.21 g, Sigma-Aldrich) was added, giving a rise in the pH from 3 to 11. The mixture kept stirring for another 30 minutes before being transferred to an autoclave, and heated for 24 hours at 150 °C. The crystalline product was washed with deionized water, centrifuged and dried at 100 °C for 24 hours.

3.1.3 Tetraamminegold(III) nitrate, $[Au(NH_3)_4](NO_3)_3$

Two batches (from now on labeled Au(III)/1 and Au(III)/2) of tetraamminegold(III) nitrate, $[Au(NH_3)_4](NO_3)_3$, was prepared according to Skibsted and Bjerrum[73]. Gold(III)chloride hydrate ($HAuCl_4$, corresponding to 0.5 g of gold, Sigma-Aldrich) was dissolved in a supersaturated ammonium nitrate solution of ammonium nitrate (NH_4NO_3, 95 g, Merck) and cold deionized water (H_2O, 70 mL). The pH was $\approx$ 1. 25 % NH_3 solution (Merck) was heated using boiling water, creating gaseous NH_3, which was passed through the supersaturated ammonium

nitrate solution until pH reached 7. The mixture was left overnight in a stopped flask and a white-yellowish precipitate of tetramminegold(III) nitrate was formed. The actual compound ratios, filtering methods and drying conditions for the two batches can be seen in Table 3.1. Experimental set-up is shown in Figure 3.1.

Table 3.1: Experimental conditions for Au(III)/1 and Au(III)/2

Sample	**Amount of NH_4NO_3**	**Amount of H_2O**	**Amount of $HAuCl_4$**	**Filtering method**	**Drying cond.**	**Color of product**
Au(III)/1	23.77 g	17.5 mL	0.225 g	Method 1	100 °C for 24 hrs	White-yellowish
Au(III)/2	82.79 g	59.9 mL	0.7497 g	Method 2	40 °C for 24 hrs	White

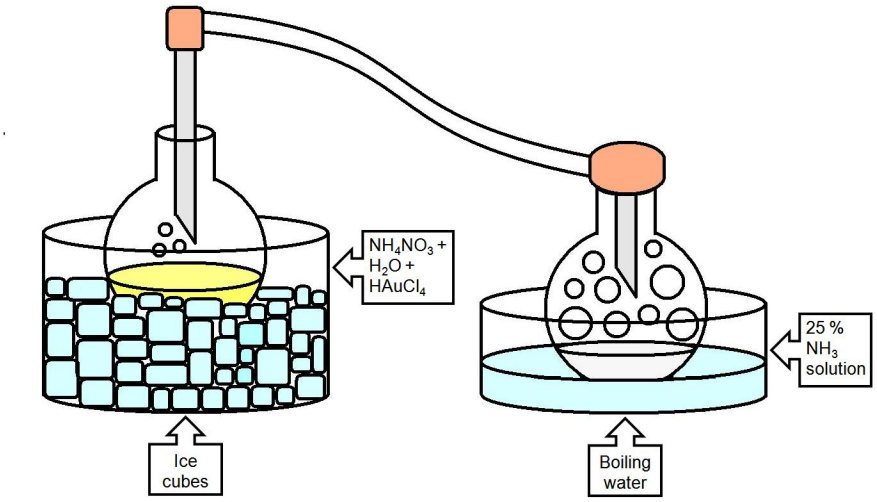

Figure 3.1: Experimental set-up for preparation of $[Au(NH_3)_4](NO_3)_3$

Different filtering methods were used for the two batches.

Method 1

The Au(III)/1 product was carefully filtered from the ammonium nitrate solution and dried at 100 °C for 24 hours. The powder obtained a slightly yellowish color.

Method 2

The ammonium nitrate solution was carefully removed from the flask using a droplet counter. A few drops of silver nitrate solution ($AgNO_3$, Sigma-Aldrich and deionized water, H_2O) was added to this solution resulting in formation of a white residue of silver chloride, AgCl, thus indicating the presence of chlorine. The obtained white-yellowish precipitate of tetraamminegold(III) nitrate, still present in the flask, was thoroughly washed with a supersaturated ammonium nitrate solution (Merck, ammonium nitrate, NH_4NO_3, 95 g and cold deionized water, H_2O, 70 mL) and ethanol (C_2H_5OH). The flask was placed over ice cubes to recrystallize tetraamminegold(III) nitrate. After recrystallization, the ammonium nitrate and ethanol solution was removed from the product and checked for chloride using a few drops of silver nitrate solution. The washing procedure and recrystallization of the product were carried out several times until formation of silver chloride residue was no longer observed. The white Au(III)/2 product was dried at 40 °C for 24 hours.

3.2 Ion-exchanged samples

3.2.1 Preperation of Au solutions for ion-exchange

$1.16{\cdot}10^{-3}$ M Au solution

A $1.16{\cdot}10^{-3}$ M Au-solution was prepared by adding gold(III)chloride hydrate ($HAuCl_4{\cdot}H_2O$, 0.2 g, Sigma-Aldrich) to 500 mL deionized water prepared according to equations 3.1, 3.2 and 3.3:

$$m_{Au} = 0.2g \tag{3.1}$$

$$Mw_{HAuCl_4} = 339.79\frac{g}{mole} \tag{3.2}$$

0.1976 g $HAuCl_4{\cdot}H_2O$ was added to 500 mL water, giving the solutions a concentration of $1.16{\cdot}10^{-3}$ M:

$$C = \frac{n}{V} = 1.16 \cdot 10^{-3} M \tag{3.3}$$

Au(III) solutions

Au(III)/1 powder ($[Au(NH_3)_4](NO_3)_3$, 2.1312 g) and deionized water (H_2O, 94.5 g) was mixed to make a 0.05 M Au(III) solution. pH of the solution was ≈ 4-5. In addition, another solution with higher concentration (0.1 M) was prepared by mixing Au(III)/2 powder ($[Au(NH_3)_4](NO_3)_3$, 5.76 g) with deionized water (H_2O, 127.5 mL). The two solutions were named Au(III)/1 solution and Au(III)/2 solution, respectively. The Au(III)/1 solution had a pale yellowish color, while the Au(III)/2 solution withheld a slightly white, almost clear color.

3.2.2 Ion-exchange of the zeolites ZSM-5 and HY, and the zeotype SAPO-34

The zeolites H-ZSM-5 (Zeolyst International-CVB 8014, SiO_2:Al_2O_3 mole ratio = 80, calcined to ZSM-5), HY (Zeolyst International-CVB 780, SiO_2:Al_2O_3 mole ratio = 80), and the zeotype SAPO-34 (prepared as described above) were each mixed with the three gold solutions (approximately 1- 2 gram zeolite/zeotype per 30 mL solution). The ion exchanges were carried out either hydrothermally in separate autoclaves at 150 °C for 24 hours or by stirring the slurries in separate Erlenmeyer flasks at room temperature for 24 hours (conventional ion-exchange). The reaction products were obtained by washing and centrifuging the slurries with deionized water. An overview of all ion exchanged samples is shown in Table 3.2.

Table 3.2: Preparation conditions for the Au ion-exchanged zeotypic samples

Zeolite/ zeotype	**Amount of zeotypic material**	**Type of Au solution**	**Amount of Au solution**	**Ion-exchange method**	**pH**	**Drying cond.**	**Color of product**	**Sample name**
ZSM-5	1.0085 g	$1.16{\cdot}10^{-3}$ M Au	30 mL	HT	2	24 hrs @ 100 °C	Pale purple	Au:ZSM-5
HY	1.0068 g	$1.16{\cdot}10^{-3}$ M Au	30 mL	HT	2-3	24 hrs @ 100 °C	Pale purple	Au:HY
SAPO-34	1.0074 g	$1.16{\cdot}10^{-3}$ M Au	30 mL	HT	3-4	24 hrs @ 100 °C	Pale purple	Au:SAPO-34
ZSM-5	2.0043 g	0.05 M Au(III)/1	30 mL	Conv.	6	24 hrs @ 100 °C	White-yellowish	Au(III)/1:ZSM-5
HY	2.0066 g	0.05 M Au(III)/1	30 mL	Conv.	6	24 hrs @ 100 °C	White-yellowish	Au(III)/1:HY
SAPO-34	2.0049 g	0.05 M Au(III)/1	30 mL	Conv.	6	24 hrs @ 100 °C	White-yellowish	Au(III)/1:SAPO-34
ZSM-5	2.0068 g	0.1 M Au(III)/2	30 mL	Conv.	5	24 hrs @ 40 °C	White	Au(III)/2:ZSM-5
HY	2.0059 g	0.1 M Au(III)/2	30 mL	Conv.	5	24 hrs @ 40 °C	White	Au(III)/2:HY
SAPO-34	2.0036 g	0.1 M Au(III)/2	30 mL	Conv.	5	24 hrs @ 40 °C	White	Au(III)/2:SAPO-34

3.3 Element analysis

Treatment of zeotypic material prior to the digestion process is normally carried out using either Agua Regia (Method 1) or a HF + HNO_3 mixture (Method 2). For silicoaluminophosphates (SAPOs) and zeolites the HF + HNO_3 mixture is normally preferred. However, the fluoride ions tend to form indissoluble Al-F complexes, thus unables the detection of accurate alumina content in the samples. In addition, the fluoride ions are known to form indissoluble Au-F complexes (most likely AuF_5). The alumina, phosphorous and gold content in the samples are therefore detected using Method 1. Silicon, on the other hand, is not fully dissolved in Agua Regia, hence the element content in the samples are detected using Method 2. Approximately 10-40 mg of zeotypic material was added to a 18 mL vessel of Teflon and pre-treated according to either Method 1 or 2, described under;

Method 1

0.70 ± 0.05 g concentrated HNO_3 Supra pure (40%) and 1.65 ± 0.1 g concentrated HCl was added to the sample in the 18 mL vessel. The digesting process were preformed using the same UltraClave from Milestone. The samples were heated to ≈ 250 °C and kept at this temperature for ≈ 40 minutes to ensore complete dissolution. The total pressure in the UltraClave was 100-110 bar during the isotermic digestion process. Figure 3.2 illustrates the temperature profile. The samples were further diluted with deionized water to give a final volume of 220 ± 0.5 mL/g.

Method 2

0.68 ± 0.04 g concentrated HF Supra pure (40%) and 1.8 ± 0.04 g concentrated HNO_3 was added to the 18 mL vessel and digested using a UltraClave as for Method 1, with the same temperature og pressure. The samples were kept at 250 °C for 10 minutes. The temperature profile is given in Figure 3.3. The samples were further diluted with deionized water go give a final volume of 187 ± 0.5 mL/g.

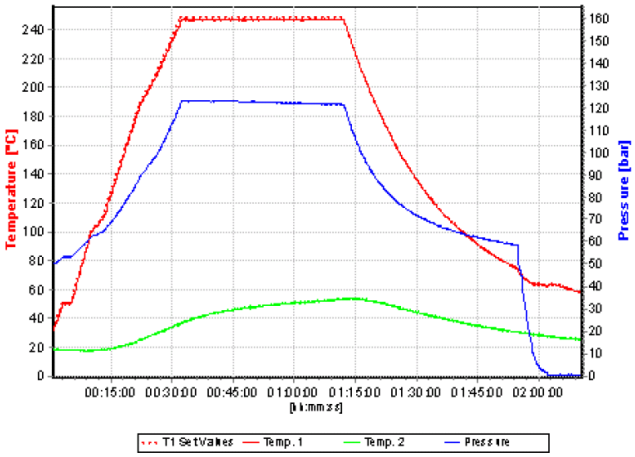

Figure 3.2: Temperature profile for the digesting process of samples pre-treated with Agua Regia

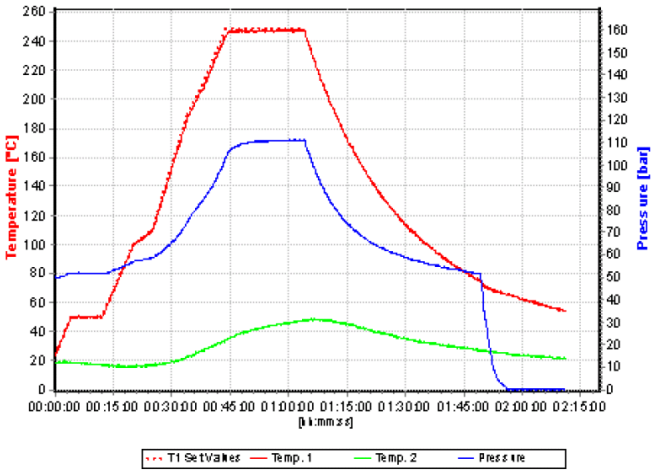

Figure 3.3: Temperature profile for the digesting process of samples pre-treated with 18% HF + 42% HNO_3

The digested samples were analyzed using a ELEMENT2 ICP-MS detector. The detector is equipped with three resolution modes; low, medium and high. The low resolution mode can detect 5 billion ions per second before reaching its saturation limit. If a sample contains abundance of elements exceeding this limit, either medium or high resolution mode are required. After detection of the elements (in μg/g), the weight per cent (wt%, Eq. 2.12) and mole ratios of the elemets of

interest were calcultated.

3.4 Temperature-Programmed Reduction (TPR)

Temperature-programmed reduction was used to determine the reducibility and stability of the Au(III)/2:Z samples. The analyses were performed using a Perkin-Elmer Thermogravimetric Analyzer (TGA7). Approximately 20- 30 mg of sample were heated from room temperature to 600 °C at a heating rate of 3 °C/min in argon-hydrogen mixture (11 ml/min). Further, an isothermal step were carried out at 600 °C for 30 minutes before cooling the samples down to room temperature at a cooling rate of 15 °C/min. In addition, a 403C Aëolos Mass Spectrometer from Netzsch was used with the same temperature conditions as mentioned above. 20 ml/min argon was used as protective gas for the weighing house and fed through the sample compartment.

3.5 Surface area measurements (BET)

A Micromeritics Tristar3000 surface Area and Porosity Analyzer was used to determine the internal surface area of calcined AuSAPO-5, calcined SAPO-34, and the Au(III)/1 and Au(III)/2 ion-exchanged zeotypic samples. The zeotypic sample were degassed using a Vac-Prep 061 Sample Degas at 250 °C and 0.12 mbar (85 mTorr). The degassing was performed 24 hours prior to the BET measurements. Approximately 0.1-1.0 gram of material was used for the measurements. Normally, a larger amount of sample is preferred for each measurements, but due to a low amount of sample obtained from the synthesis and ion-exchange procedures it was not possible to do the surface area measurements with a higher amount of sample.

3.6 Powder X-ray diffraction (PXRD)

X-ray powder diffraction was used for phase determination of the samples. X-ray powder diffractograms were measured using a Siemens D-5005 diffractometer with $Cu_{K\alpha}$ radiation. The diffractometer operated at 50 keV and 40 mA with a constant

slit opening and a step size of 0.02° converting a range of 10-60° 2θ with a counting time of 5 seconds per step. The instrumental broadening is 0.090. The parameter file used was specially designed to detect small particles. The samples (0.40- 0.42 g) were packed into plastic sample holders. For samples where less than 0.40 gram of product was available, smaller sample holders (containing approximately 0.10 g of sample) were used. After analysis, the diffractograms were compared to already known diffraction patterns from the database to confirm phase equality with the desired product.

3.7 X-ray absorption spectroscopy (XAS)[68,69]

3.7.1 XAS studies on Au zeotypic materials

The XAS experiments have been preformed using two different synchrotron facilities; The Swiss-Norwegian beamlines (SNBL, BM01b) at European Synchrotron Radiation Facility (ESRF) and the Material Science Beamline I811 at the MAXII ring at MAX-lab. At SNBL, the gold L_{III}-edge data were collected using a 13-element Germanium Detector. Both transmission and fluorescence mode were collected. A Si(111) double crystal was used as a monochromator and higher harmonics were rejected by chromium mirrors. The electron beam line energy at ESRF was 6.04 GeV with a maximum current of 200 mA. The first and second ionization chambers were filled with 100% N_2 and 65% N_2 + 35% Ar, respectively. Both XANES and EXAFS scans were collected. XANES spectra were measured with 10 eV steps below the edge, 0.8 eV in the edge region, and steps equivalent to 0.05 $Å^{-1}$ increments above the edge (region borders were 11800, 11900, and 12000 eV). For measurements of EXAFS spectra 5 eV steps was used below the edge, 0.3 eV steps in the edge region, and steps equivalent to 0.05 $Å^{-1}$ increments above the edge (region borders were 11720, 11890, and 11998 eV. All XANES and EXAFS spectra were energy corrected against a Au foil calibration (11919 eV).

At the Material Science Beamline I811 at MAX-lab, the gold L_{III}-edge data were collected only in fluorescence mode. The beamline (MAXII) was equipped with two focusing mirrors (silicon and zerodur) and a Si(111)/Si(311) double-crystal

monochromator. The operating energy for the MAXII ring was 1.5 GeV with a maximum current of 280 mA. The first and second ionization chambers were filled with 0.2 bar Ar + 1.1 bar He and 2 bar Ar, respectively. A liquid nitrogen cooled 7-element Si(Li) detector was used to collect the data. In addition, a piezo-electric motor was used for stabilization of the beam intensity and detuning, controlled by a PID sample in Mostab (Struck GmbH). Both XANES and EXAFS spectra were measured with 1.0 eV steps below the edge, 0.5 eV in the edge region, and steps equivalent to 0.05 $Å^{-1}$ increments above the edge (region borders were 11720, 11900, and 11970 eV). All XANES and EXAFS spectra were energy corrected against a Au foil calibration (11919 eV).

The samples (100-125 mg) were packed in aluminum samples holders with a thickness of 1 mm and a total cross section of 1.2 cm^2, and sealed using Kapton tape windows.

3.7.2 In-situ measurements

For in-situ studies, samples (125 mg) were packed in the in-situ cell. Quartz wool was packed on both sides of the samples to maintain a uniform temperature during heating. A sketch of the cell is given in Figure 3.4.

The reaction gases were passed directly through the sample with the flow rate being regulated by flow controllers. The samples were heated by placing two heating cartridges in the cell just below and under the sample. The temperature was controlled by a thermocouple inserted in the cell. The cell was placed between the two ion chambers, as illustrated in Figure 3.5.

The in-situ EXAFS was preformed as illustrated in Figure 3.6. A EXAFS scan was preformed at room temperature in air, before switching to 100% He and raising the temperature with a heating rate of ≈ 4.5 °C/min. While raising the temperature, several XANES scans were collected. At 150 °C two EXAFS scans were collected; the first one in 100% He and the second one after switching to 5% H_2 in He. Two more EXAFS scans were preformed at 350 °C and 450 °C, in addition to several

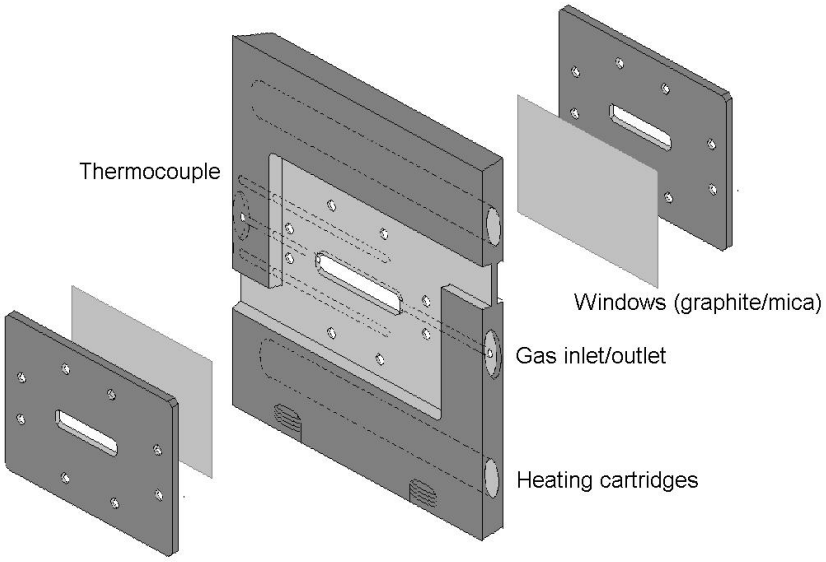

Figure 3.4: In-situ cell for XAS experiments (illustration by Karina Mathisen)

XANES scans before switching from 5% H_2 in He to 0.6% NO in He. The sample were cooled down to room temperature at a rate of ≈ 4.5 °C/min, where one final EXAFS scan was collected. All the flow rates during the in-situ measurements were 15 mL/min.

During the in-situ experiment of Au(III)/2:SAPO-34 the outlet of the cell was connected to a Pfeiffer Vacuum OmniStar mass spectrometer. The mass spectrometer measured the variation in the exhaust gas component concentrations during the experiment.

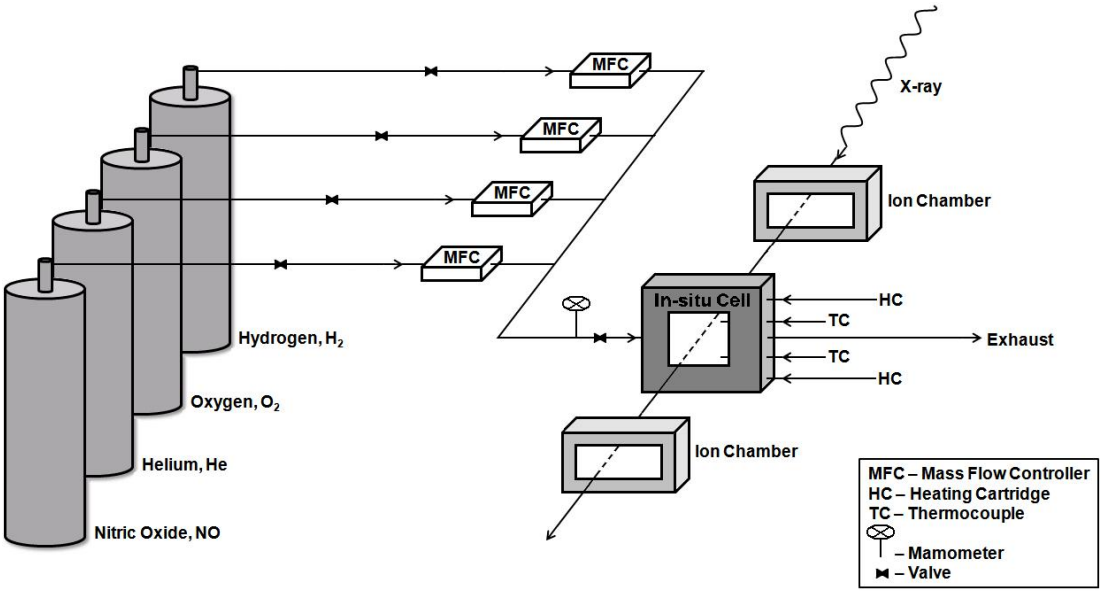

Figure 3.5: Experimental in-situ set-up

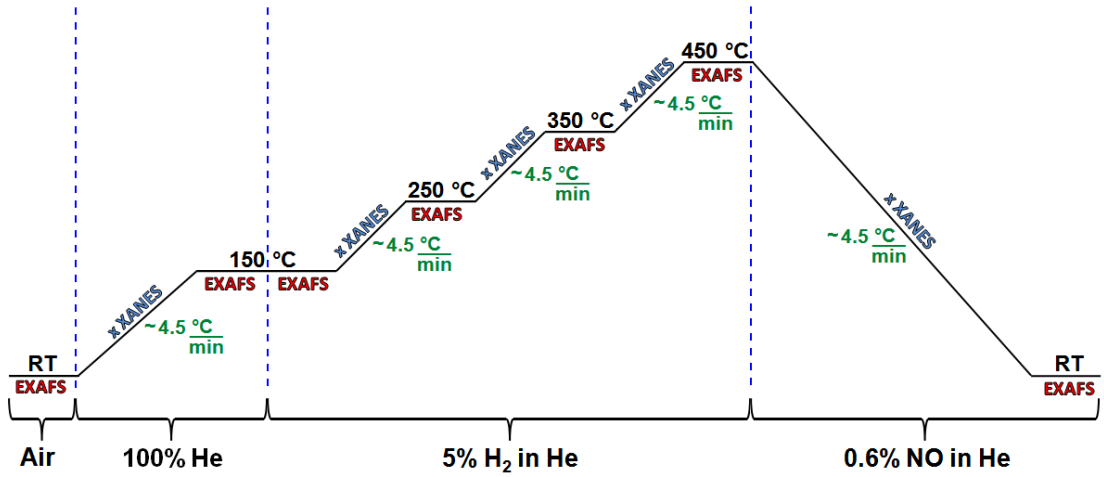

Figure 3.6: Conditions during the EXAFS in-situ experiment

3.7.3 Data analysis

The background of the XAS data were substracted using the Autobk algoritm[72] in Athena[70]. The Au L_{III}-edge value, E_0, was determined manually as the first large peak in the normalized first derivative spectrum. Spurious points (glitches) were removed manually from the data. Linear combination and peak fitting procedures were used to calculate the area under the white line and to fit the XANES to reference compounds. The linear combination fitting was preformed on normalized μ(E) spectra over a range from 20 eV below the absorption edge to 50 eV above the edge for all the spectra investigated. For pre-edge fitting an arctangent function was used to model the step portion of the data with the centroid set to the white line ($\approx$ 11923 eV) before refinement. An Gaussian function was used, and as this function is normalized the amplitudes directly gave the area under the white line. The fitting range used for determination of the area under the white lines reaches 20 eV below the Au L_{III}-edge to 30 eV above the edge. The same normalization range (30 eV below the Au L_{III}-edge to 150 eV above the edge) was applied to all the spectra prior to the linear combination and peak fitting operations.

The EXAFS part of the spectra were extracted to yield $\chi_i^{exp}(k)$ using Excurve[71]. Fitting of $\chi_i^{exp}(k)$ to $\chi_i^{th}(k)$ was carried out using the curved wave theory which calculated the phase shifts. The final data were Fourier filtered over a wide range (1.5-25 Å) to remove low-frequency contributions to the EXAFS below 1.5 Å. This procedure do not smooth the spectra or reduce any noise. The EXAFS refinements give information about multiplicity, N, bonding distance, R (Å), and thermal vibration, Debye Waller factor ($2\sigma^2$). EF is the refined correction of Fermi energy in vacuum, compared to E_0 in Excurve[71]. The fit factor, R, given in per cent, represents the goodness of fit between experimental data ($\chi_i^{exp}(k)$) and the theoretical refinement ($\chi_i^{th}(k)$). The statistical R-factor is according to Equation 3.4 and gives indication of the quality of fit in k-space.

$$R = \sum_i^N \left[\frac{1}{\sigma_i} \left(\left| \chi_i^{exp}(k) - \chi_i^{th}(k) \right| \right) \right] \times 100\% \tag{3.4}$$

The standard deviation in the last significant digit as calculated by Excurve is

given in parentheses in the tables presenting the EXAFS refinement results (see Chapter 4). These estimates, however, will in cases of high correlation between parameters lead to an overestimation of accuracy as the standard deviations for bonding distances are ±0.01 Å for small r-values and ±0.04 Å for r-values exceeding 3 Å. The deviation for $2\sigma^2$ is ±20%. The data were fitted with different k-values, depending on the signal to noise ratio for the data. The r-values are the same for all refinements, ranging from 0.1 to 6.0 Å.

3.8 Activity measurement for CO oxidation and PROX

Activity measurements of the samples Au(III)/2:HY and Au(III)/2:SAPO-34 were performed using a test rig provided by the Department of Chemical Engineering at NTNU. The rig is illustrated in Figure 3.7. 0.1 g of Au(III)/2:Z was used per measurement. The fixed-bed reactor (Figure 3.8) was packed with quartz on both sides of the Au(III)/2:Z sample to make sure that the temperature was uniform in the catalyst bed.

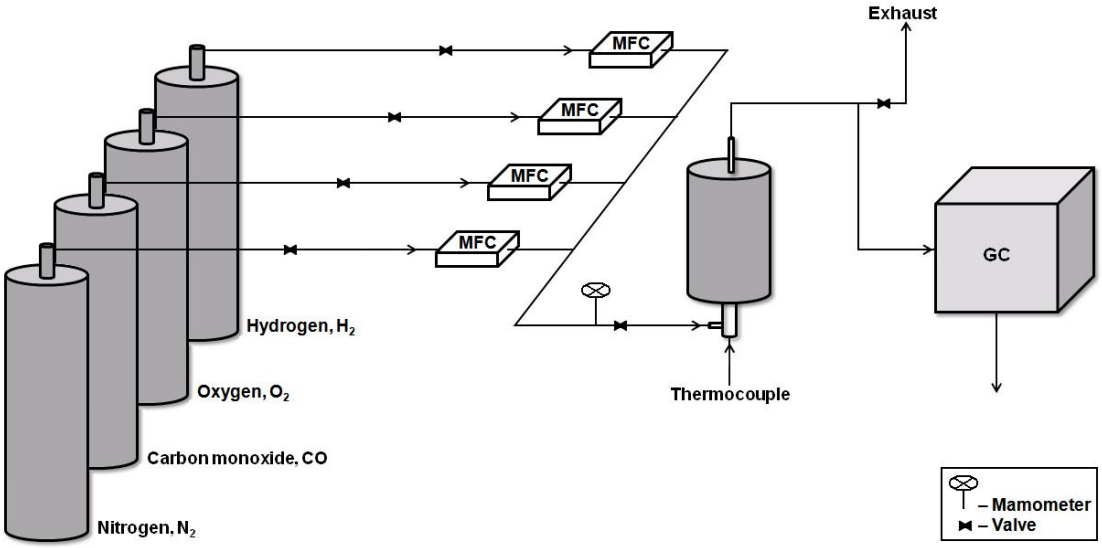

Figure 3.7: Activity measurement set-up for CO oxidation and PROX with external heating

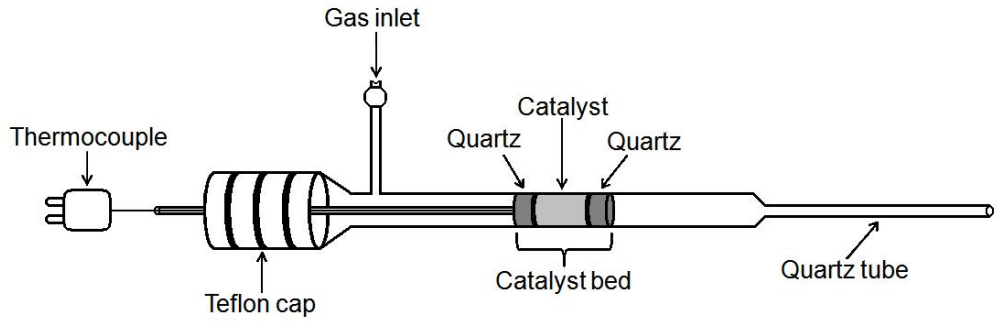

Figure 3.8: Illustration of the fixed-bed reactor used for CO oxidation and PROX activity measurement

The catalyst were heated using an external heating jacket. Temperature controllers was placed right beneath the Au(III)/2:Z pieces in the reactor and along the reactor wall next to the catalyst bed. The temperature was raised and lowered by programming the heating jacket with the desired temperature profile, as illustrated in Figure 3.9.

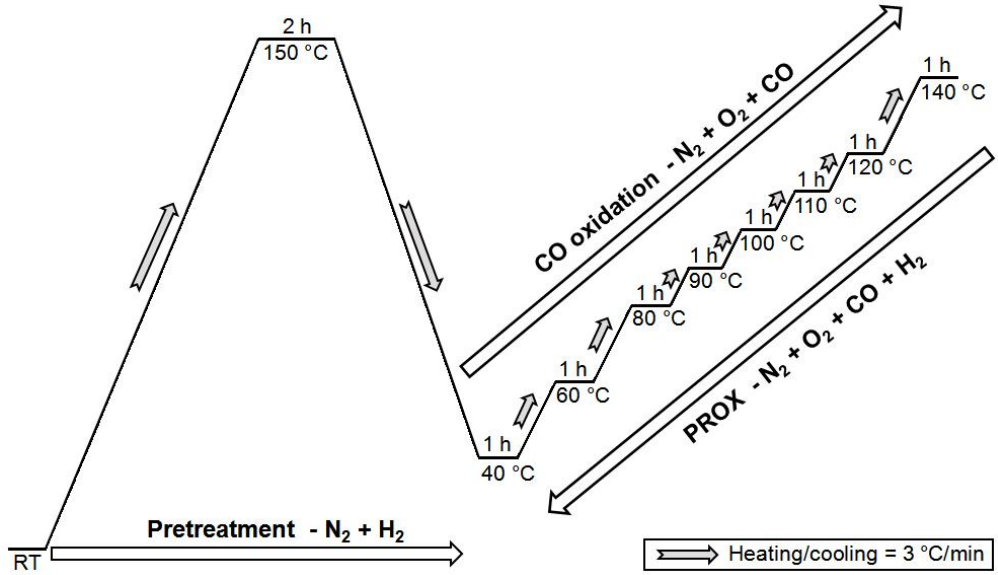

Figure 3.9: Temperature profile for activity measurement for CO oxidation and PROX

The catalyst samples were pretreated in N_2 (80 mL/min) and H_2 (20 mL/min) for 2 hours prior to the reaction to reduce the gold particles present in the samples.

Table 3.3: Gas flow conditions for activity measurements in the presence and absence of hydrogen

Mixture (mL/min)	**CO oxidation**	**PROX**
CO	1	1
O_2	1	1
N_2	98	28
H_2	0	70

The activity measurements were performed with a total gas flow of 100 mL/min in the temperature range 40- 140 °C. Specific flow conditions for the CO oxidation and PROX are listed in Table 3.3. The conversion of CO has been calculated from the CO and CO_2 concentration in the outlet gas and is obtained as follows:

$$X_{CO} = \frac{x_{CO_2}}{x_{CO_2} + x_{CO}} \cdot 100\% \tag{3.5}$$

Chapter 4

RESULTS AND DISCUSSION

In this chapter results from the various characterization techniques, applied to study the gold samples, will be presented. All the results will be interpreted and discussed in detail. The findings will be compared with results reported in literature, papers, etc., and possible explanations for the findings will be given.

4.1 Element analysis

Element analyses confirmed gold incorporation in AuSAPO-5 during synthesis. As listed in Table 4.1 the molar composition for AuSAPO-5 differ somewhat from that expected from synthesis (0.033 Au : 0.3 Si : Al : P). Lower gold and phosphorous contents are detected in the as-prepared AuSAPO-5 than what would be expected. This indicates that some of the gold and phosphorous may have been lost during some of the synthesis steps (washing, centrifugal treatment, drying etc.). However, the desired amount of gold incorporated into the framework is detected for the calcined sample. Since the amount of phosphorous detected is still low, it is reasonable to believe that the gold has incorporated on some of the phosphorous sites in the framework during heat treatment. For the ion-exchanged SAPO-34 samples, a larger amount of Au has been introduced when the hydrothermal ion-exchange method was used compared with the conventional method. As mentioned in Section 2.1.4, the amount of metal ion which can be exchanged with the hydrothermal method is up to ten times higher than the conventional method,

using the same metal precursor.

Table 4.1: Results of elemental analyses of gold containing zeotypic samples

Molar composition						
Sample	**Au** (g)[a]	**Si** (g)[a]	**Al** (g)[b]	**P** (g)[a]	**wt%** Au	**Molar Composition**
AuSAPO-5 as-prep.	$3.64 \cdot 10^{-3}$	$7.0 \cdot 10^{-3}$	0.210	0.218	0.36	$Au_{0.002}Si_{0.03}AlP_{0.90}O_4$
AuSAPO-5 calc.	$4.55 \cdot 10^{-3}$	0.010	0.195	0.200	0.45	$Au_{0.003}Si_{0.05}AlP_{0.89}O_4$
Au:SAPO-34 as-prep.	$3.38 \cdot 10^{-3}$	0.028	0.200	0.200	0.34	$Au_{0.002}$:$Si_{0.13}AlP_{0.87}O_4$
Au(III)/1:SAPO-34 as-prep.	$7.34 \cdot 10^{-4}$	0.024	0.171	0.177	0.07	$Au_{0.0006}$:$Si_{0.11}AlP_{0.86}O_4$
Au(III)/2:SAPO-34 as-prep.	$6.18 \cdot 10^{-4}$	0.022	0.204	0.201	0.06	$Au_{0.0004}$:$Si_{0.10}AlP_{0.86}O_4$

[a] Element detected in sample diluted using Method 1 described in Section 3.3

[b] Element detected in sample diluted using Method 2 described in Section 3.3

As mentioned in Section 2.1.6, 100% exchange of gold in ZSM-5 will correspond to incorporation of 6.567 Au wt% in the samples. As seen in Table 4.2, there is far from 100% cation exchange of gold in the samples. For Au:ZSM-5 0.33 wt% gold is detected, yielding a CEC of 0.05 %. The cation exchange capacities (CECs) for Au(III)/1:ZSM-5 and Au(III)/2:ZSM-5 are calculated to be 0.01% and 0.008%, repectively. One of the main reasons why less gold has been introduced into these sample than what detected for Au:ZSM-5 is probably the choice of ion-exchange method. Au:ZSM-5 was prepared by hydrothermal ion-exchange, while Au(III)/1:ZSM-5 and Au(III)/2: ZSM-5 were prepared with the conventional ion-exchange method. As mentioned above the amount of metal introduced to the zeotype is often much higher when the hydrothermal ion-exchange method is used compared to the conventional ion-exchange method.

In addition, Si/Al ratios differ from that given by the supplier. The standard ZSM-5 (Zeolyst International, CBV 8014) used for the ion-exchange reactions should have a Si/Al ratio of 40, according to the manufacturer[74]. The Si/Al ratios detected in the Au:ZSM-5, Au(III)/1:ZSM-5 and Au(III)/2:ZSM-5 are 26.28, 32.26 and 31.42, respectively. The aberration is most likely due to formation of unsolv-

able alumina compounds formed during the digestion process with hydrofluoric acid and Agua Regia.

Table 4.2: Results of element analyses of gold ion-exchanged ZSM-5 samples

Sample	**Au** (g)[a]	**Si** (g)[b]	**Al** (g)[a]	**wt% Au**	*Si/Al* **ratio**
Au:ZSM-5	$3.30 \cdot 10^{-3}$	0.314	0.012	0.33	26.28
Au(III)/1:ZSM-5	$7.39 \cdot 10^{-4}$	0.325	0.010	0.07	32.26
Au(III)/2:ZSM-5	$4.59 \cdot 10^{-4}$	0.292	$9.66 \cdot 10^{-3}$	0.05	31.42

[a] Element detected in sample diluted using Method 1 described in Section 3.3

[b] Element detected in sample diluted using Method 2 described in Section 3.3

The Si/Al ratios for the gold ion-exchanged HY samples were hard to determine. The alumina content in the samples reacted with both HF and Agua Regia, thus making it impossible to determine the correct alumina content in the samples due to formation of unsolvable alumina compound during the digestion process. However, the gold content was determined by following Method 1 (described in Section 3.3), as listed in Table 4.3.

Table 4.3: Gold content in the ion-exchanged HY samples

Sample	**wt% Au**
Au:HY	0.24
Au(III)/1:HY	0.17
Au(III)/2:HY	0.09

Due to the high gold content ($>$ 5 billion ions per second) in tetraamminegold(III) nitrate (Au(III)/2) a medium resolution mode was applied. The analysis concluded a gold content of 2.4 wt% Au in the complex.

4.2 Temperature-Programmed Reduction (TPR)

Heating in a reducing atmosphere (hydrogen and argon mixture) led to a weight loss for the Au(III)/2 samples, illustrated in Figure 4.1. Au(III)/2:ZSM-5 has a weight loss of 11.48%, the smallest weight loss of the three samples. Au(III)/2:HY and Au(III)/2:SAPO-34 experienced a weight loss of 17.68% and 25.68%, respectively. The main weight loss takes place before the temperature has reached 250

°C. Since the samples were not calcined prior to the analysis it is likely that the compounds responsable for the mass loss are mainly water and easily oxidizable hydrocarbon species.

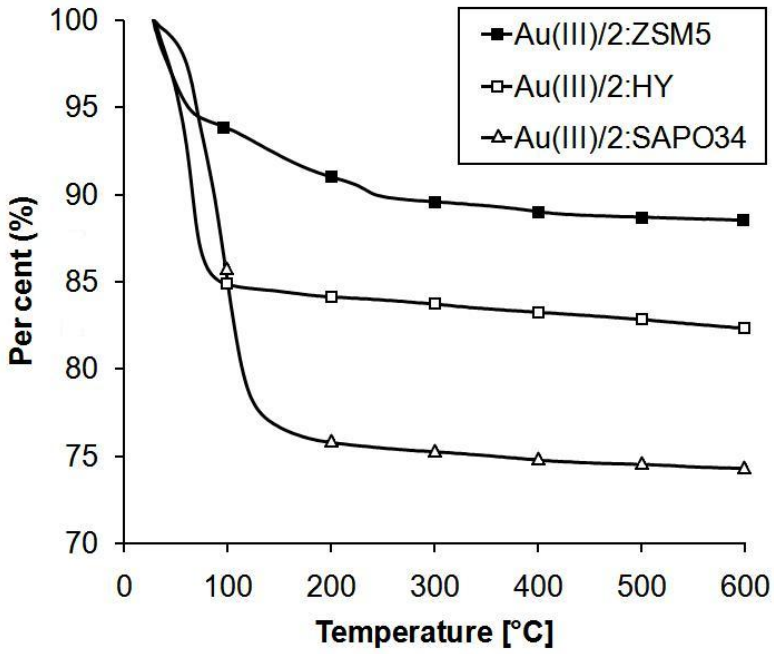

Figure 4.1: Weight loss (in per cent) for the Au(III)/2 due to heating in a reducing atmosphere

By connecting the exhaust gas to a mass spectrometer information regarding the variation of concentration of the different gas components can be obtained. Figure 4.2 (displayed on next page) illustrates the variances in H_2 and H_2O as a function of temperature for the ion-exchanged Au(III)/2 samples. As expected both Au(III)/2:SAPO-34 and Au(III)/2:HY adsorb H_2 from $\approx$ 50 °C while water evaporates at 100 °C. The adsorption of H_2 confirms a reduction of the Au present in the samples. The uniform adsorption of H_2 indicates that Au is gradually reduced as the temperature increases.

Au(III)/2:ZSM-5, on the other hand, does not show the same trend as the two other Au(III)/2 samples. This incongruous behavior can be explained by the agglomeration of GNCs with rising temperature. H_2 is assumed to be both dissociatively and associatively adsorbed on the ZSM-5 surface at $\approx$ 70 °C. When the temperature

increases, the GNCs agglomerate, hence occupy more of the ZSM-5 surface. The associatively adsorbed will therefore desorb from the surface as a consequence of the low surface area available after agglomeration of the GNCs. The dissociatively adsorbed hydrogen is assumed to react with oxygen and be desorbed as water. As seen in Figure 4.2, both hydrogen and water evaporate from the sample at ≈ 200 °C.

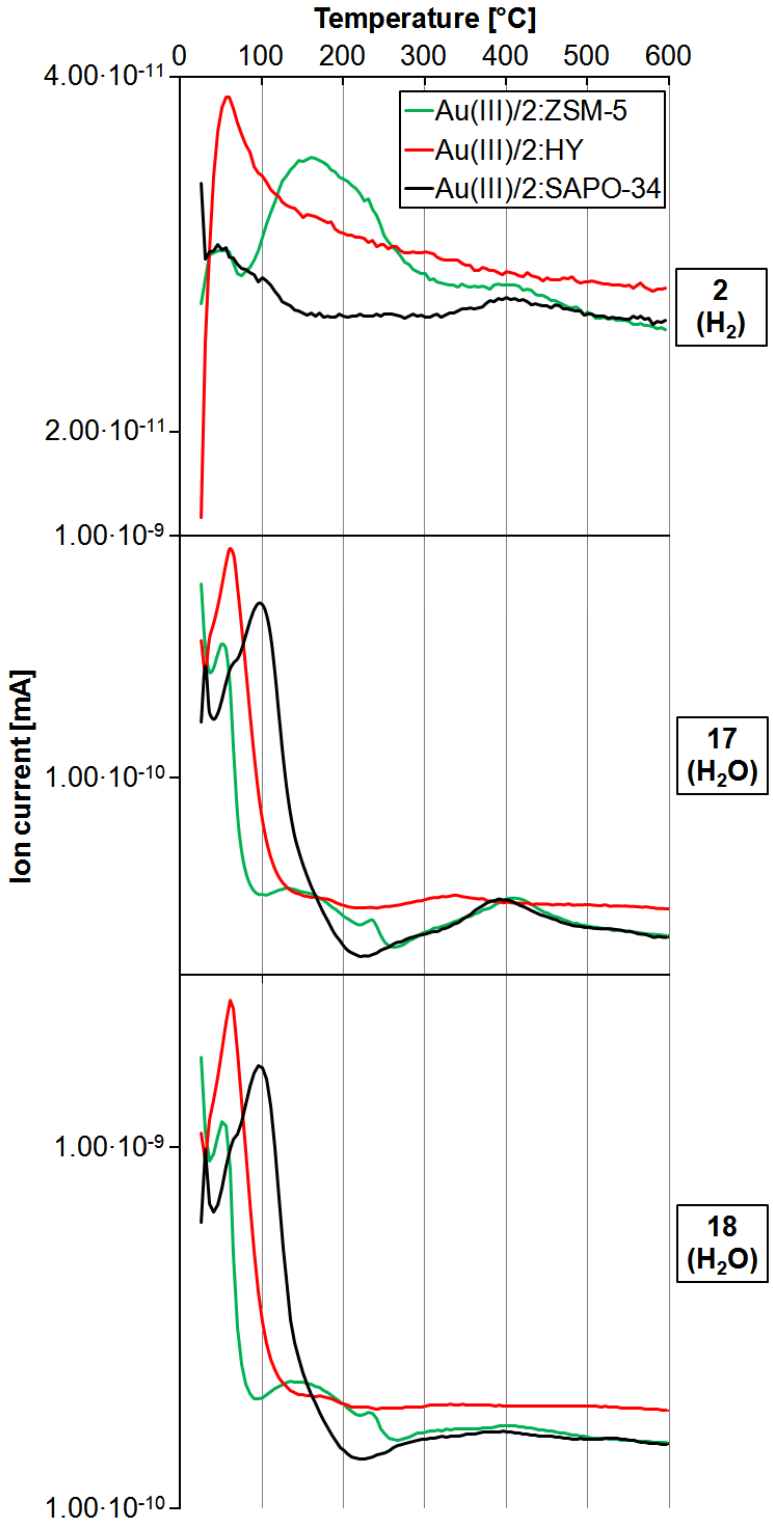

Figure 4.2: Consumption/release of H_2 as a function of temperature for the Au(III)/2 zeotypic samples

4.3 Surface area measurements (BET)

Results from internal surface area measurements are given in Table 4.4. Note that the somewhat high standard deviations for the measurements are due to low amount of sample used for the measurements.

Table 4.4: Internal surface areas of zeotypic samples

Zeotypic sample	**Internal surface area** (m^2/g)
SAPO-34 calc.	578 ± 15
AuSAPO-5 calc.	315 ± 7
Au(III)/1:ZSM-5 as-prep.	402 ± 9
Au(III)/1:HY as-prep.	744 ± 14
Au(III)/1:SAPO-34 as-prep.	417 ± 11
Au(III)/2:ZSM-5 as-prep.	333 ± 6
Au(III)/2:HY as-prep.	714 ± 13
Au(III)/2:SAPO-34 as-prep.	427 ± 11

The BET measurement confirmed a surface area of ≈ 315 m^2/g for the synthesized sample AuSAPO-5 (calc.). Yoon *et al.*[75] have reported a surface area of 300 m^2/g for the same zeotype, while Kumar *et al.*[76] found the surface area to be 354 m^2/g for their synthesized SAPO-5. It is therefore reasonable to conclude that incorporation of Au during the synthesis of SAPO-5 did not lower the surface area to any extent.

Synthesized SAPO-34 was found to have a surface area of ≈ 578 m^2/g. Reported surface area values for this zeotype have ranged from 310 m^2/g to 650 m^2/g, hence placing the surface area value detected well within the range.[32,75] Conventional ion-exchange of the zeotype with the Au(III)/1 and Au(III)/2 complexes lowered the surface area to ≈ 417 m^2/g and ≈ 427 m^2/g, respectively. The introduction of Au can therefore have led to some blockage of the zeotype pores. Since Au(III)/2 has a higher gold content than Au(III)/1 it would be expected a higher degree of pore blockage for Au(III)/2:SAPO-34 than for Au(III)/1:SAPO-34. As seen in Table 4.4 the opposite has been detected. Still, the values are within each others the standard derivation thus indicating that the introduction of Au via ion-exchange

with both Au(III)/1 and Au(III)/2 have led to the more or less same degree of pore blockage of the zeotype.

ZSM-5 (Zeolyst International, CBV 8014) has a initial surface area of 425 m^2/g according to the manufacturer.[74] The introduction of Au into the zeolite led to a decrease in surface area as the BET measurements concluded with a surface area of $\approx$ 402 m^2/g for Au(III)/1:ZSM-5, and $\approx$ 333 m^2/g for Au(III)/2:ZSM-5. Hence, pore blockage may have occurred during both the conventional ion-exchange processes. Since Au(III)/2 has a higher Au content than Au(III)/1 it is reasonable to believe that ion-exchange with this complex has led to a higher degree of pore blockage than what detected when the ion-exchanged was performed with the Au(III)/1 complex as the precursor. This is assumed to be the main reason to why the surface area for Au(III)/1:ZSM-5 is found to be 69 m^2/g higher than the surface area for Au(III)/2:ZSM-5.

The same trend is observed for the ion-exchanged HY samples. The initial surface area for HY (Zeolyst International, CBV 780) is 780 m^2/g according to the manufacturer.[74] The introduction of Au by conventional ion-exchange with the Au(III)/1 led to a decrease in the surface area as the BET measurements retuned a detected surface area of $\approx$ 744 m^2/g for this sample. When the zeolite is ion-exchanged with the Au(III)/2 complex an introduction of more Au has occurred, thus leading to a higher degree of pore blockage. This is probably why the BET measurements retuned a lower surface area for Au(III)/2:HY (714 m^2/g).

The introduction of Au by the conventional ion-exchange method led to an decrease in the surface area for all the samples. Chiang *et al.*[77] reported that excessive alumina may collapse the ordered microporous structure to some extent, thus lowering the BET surface area. The obvious consequence of the collapse is blockage of the pores. According to Chiang *et al.*[44] zeotypes with a Si/Al ratio $>$ 20 tend to block the pores of the zeotypic material, thus decreasing the catalytic activity. The introduction of Au to the zeotypic materials may therefore very well have led to some collapse of the structure, hence lowering the samples catalytic performance.

4.4 X-ray diffraction (XRD)

4.4.1 Synthesized gold samples

SAPO-34

Diffraction pattern for calcined SAPO-34 is shown in Figure 4.3. The pattern shows no collapse of the structure after calcination at 550 °C. Comparison with a SAPO-34 pattern available from the database confirms that the synthesis led to a pure SAPO-34 product. The characteristic features for the CHA structure are illustrated as triangular shapes in the diffractogram.

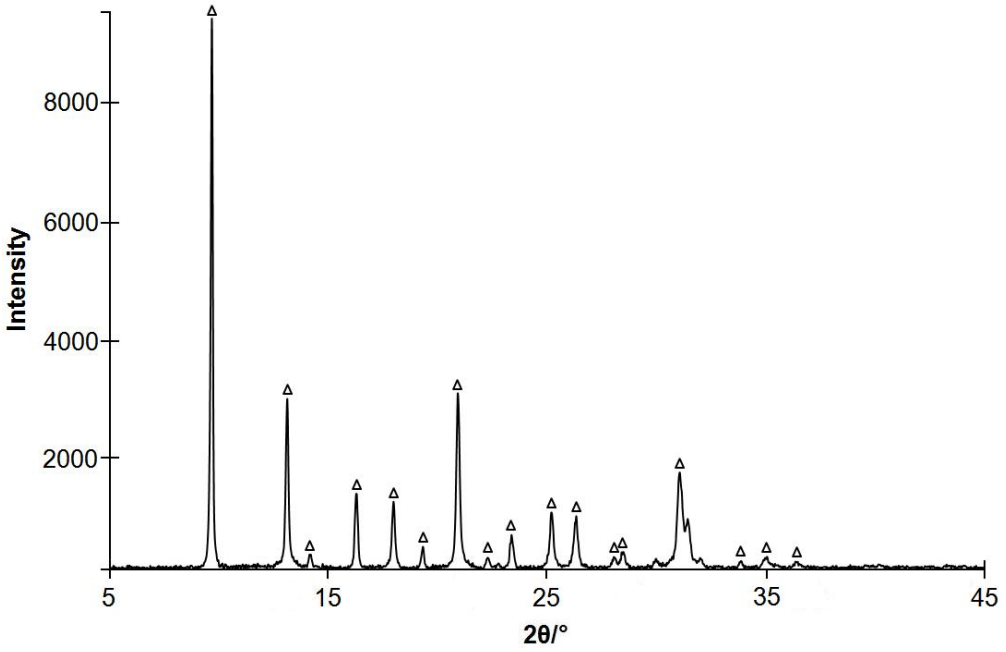

Figure 4.3: Diffraction pattern for calcined SAPO-34

AuSAPO-5

Figure 4.4 illustrates the diffraction patterns for the as-synthesized and calcined AuSAPO-5. Characteristic features for the AFI structure, confirmed by the database, are shown as triangular shapes.

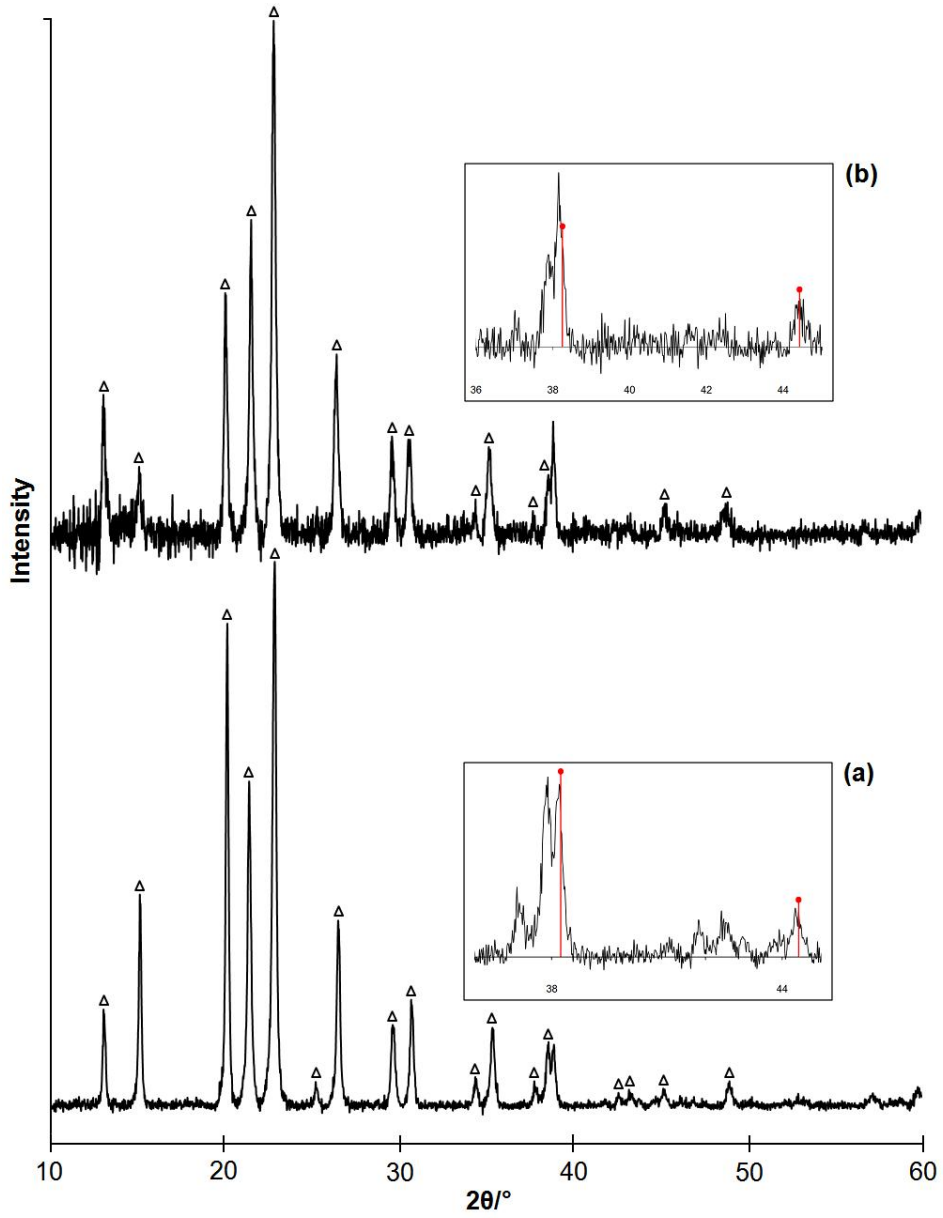

Figure 4.4: Diffraction patterns for (a) as-synthesized 0.36 wt% AuSAPO-5 and (b) calcined 0.44 wt% AuSAPO-5

Powder X-ray diffraction confirms a pure SAPO-5 structure for the as-prepared sample. Some of the characteristic peaks were not detected for the calcined samples, thus indicating some amorphous phases in the structure. Comparison with

the database confirms Au metal in both the samples (illustrated with red lines in Figure 4.4), thus confirming reduction of Au^{3+} to Au^0 during the crystallization procedure. Using Equation 2.6 the following GNC sizes were calculated (Table 4.5). Calculations are shown in Appendix A.

Table 4.5: Calculating of cluster sizes using the Scherrer equation

Sample	**GNC size (nm) calculated with Eq. 2.6**
As-synthesized AuSAPO-5	5.426
Calcined AuSAPO-5	8.815

The GNC sizes obtained are clearly too large with respect to catalysis. The Au incorporated samples are therefore not investigated any further in terms of activation measurement for carbon monoxide oxidation.

Tetraamminegold(III) nitrate

Comparison of the diffractogram for as-synthesized 2.4 wt% tetraamminegold(III) nitrate (Au(III)/2) with the database indicates a crystalline structure. However, some of the peaks present in the diffractogram are not in phase with peaks returned from the database. Peaks that are in phase are illustrated with triangular shapes in Figure 4.5.

Especially the four peaks at 11, 15.5, 18, 20.5 and 22.5 2θ values are clearly not suppose to be in a pure tetraamminegold(III) nitrate structure. By comparing the pattern to other Au complexes, two of the peaks (at 11 and 22.5 2θ) show similarities with the Au complex thiourea gold chlorate (illustrated with rectangular shapes), while the peaks at 15.5 and 20.5 2θ are in agreement with the ammonium gold chloride hydrate structure (illustrated with circular shapes). However, the peak at 18 2θ is not in agreement with any of the three Au complexes. Since both thiourea gold chlorate and ammonium gold chloride hyrdrate contains chloride, it is likely to believe that the synthesized tetraamminegold(III) nitrate still contains some chloride, despite the thorough washing procedure performed during synthe-

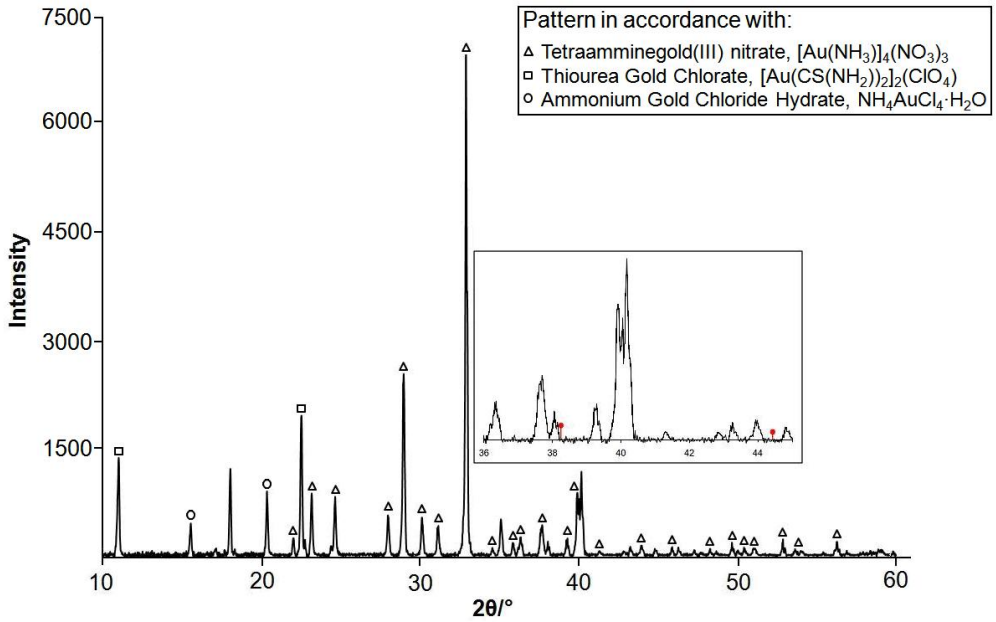

Figure 4.5: Powder X-ray Diffractogram for as-synthesized 2.4 wt% tetraamminegold(III) nitrate (Au(III)/2)

sis. Still, the structure does not contain any metallic Au particles, as indicated in Figure 4.5.

4.4.2 Ion-exchanged Au samples

Diffractograms of as-synthesized Au(III)/1 and Au(III)/2 samples are shown in Figure 4.6 and Figure 4.7, respectively. Due to low amounts of powder obtained from the conventional ion-exchange procedures, small sample holders had to be used for the experiments. The use of these sample holders decreases the signal to noise ratio as the X-ray beam has a smaller area to detect the structural information from. This often result in a noisy diffractogram with lower intensity than what would be the case if a larger sample holder was used. The diffractograms clearly illustrate that the use of small sample holders have influenced the results, especially for 0.06 wt% Au(III)/2:SAPO-34. Although, the PXRD patterns confirms no considerable collapse of the zeotypic framework as a concequence of the conventional ion-exchange with Au(III)/1 and Au(III)/2.

As indicated with red lines in the figures, it seems that non of the zeotypic samples contains large gold nanoclusters (GNCs). This indicates that the use of tetraamminegold(III) nitrate (Au(III)/1 and Au(III)/2) as Au precursors for the ion-exchange led to agglomeration of smaller GNCs than what was the case when gold(III)chloride hydrate ($HAuCl_4$) was used as the precursor. As the diffractograms indicate ion-exchange with Au(III)/1 and Au(III)/2 did not lead to an auto reduction and an agglomeration of large GNCs as was the case with gold(III)chloride hydrate as a precursor. Still, due to low signal to noise ratios it is not possible to conclude whether GNCs are present in their metallic character or not. In addition, further analyses are necessary to determine the exact oxidation state of the GNCs in the ion-exchanged Au zeotypic samples.

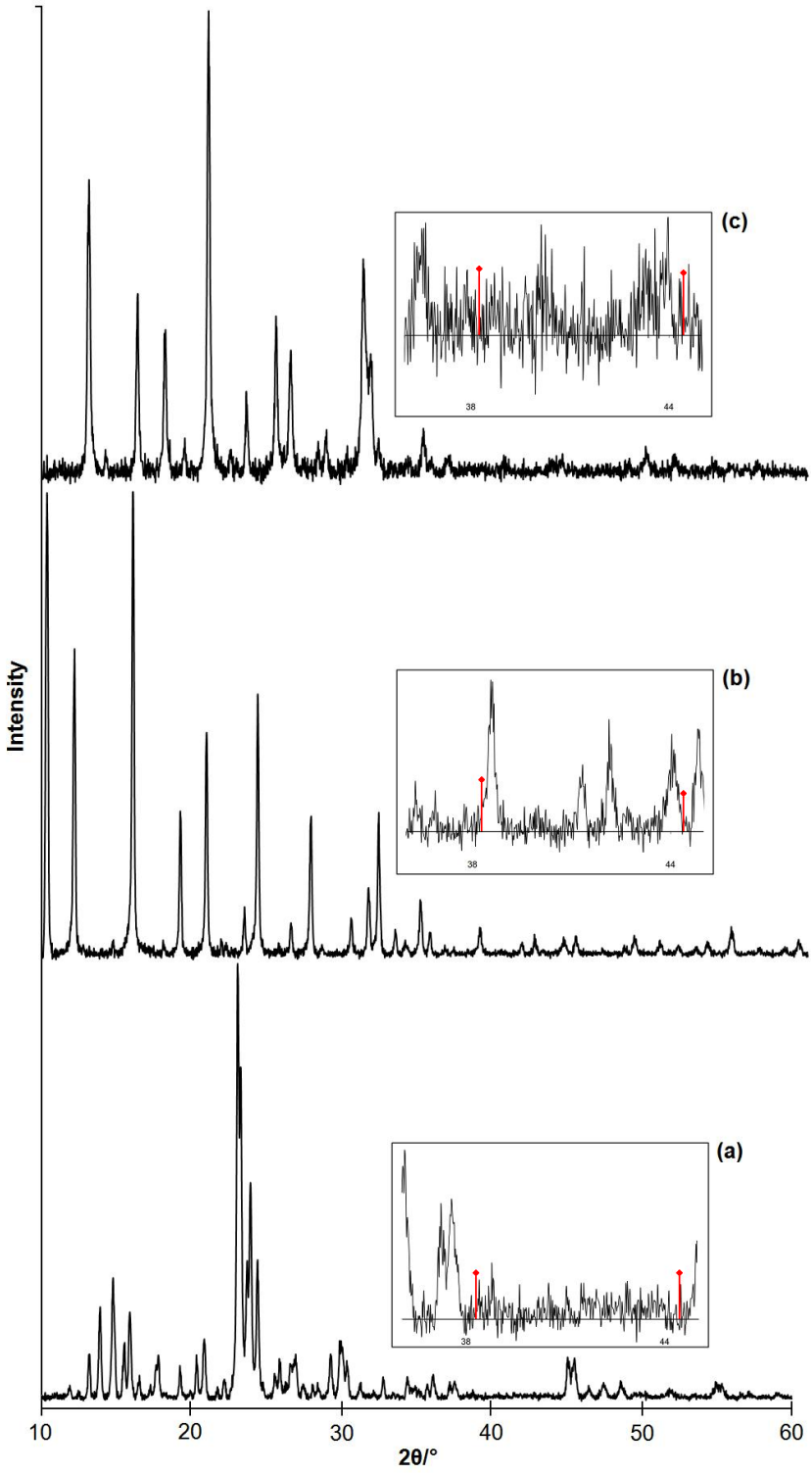

Figure 4.6: Diffraction pattern for (a) as-synthesized 0.07 wt% Au(III)/1:ZSM-5; (b) as-synthesized 0.17 wt% Au(III)/1:HY and (c) as-synthesized 0.07 wt% Au(III)/1:SAPO-34

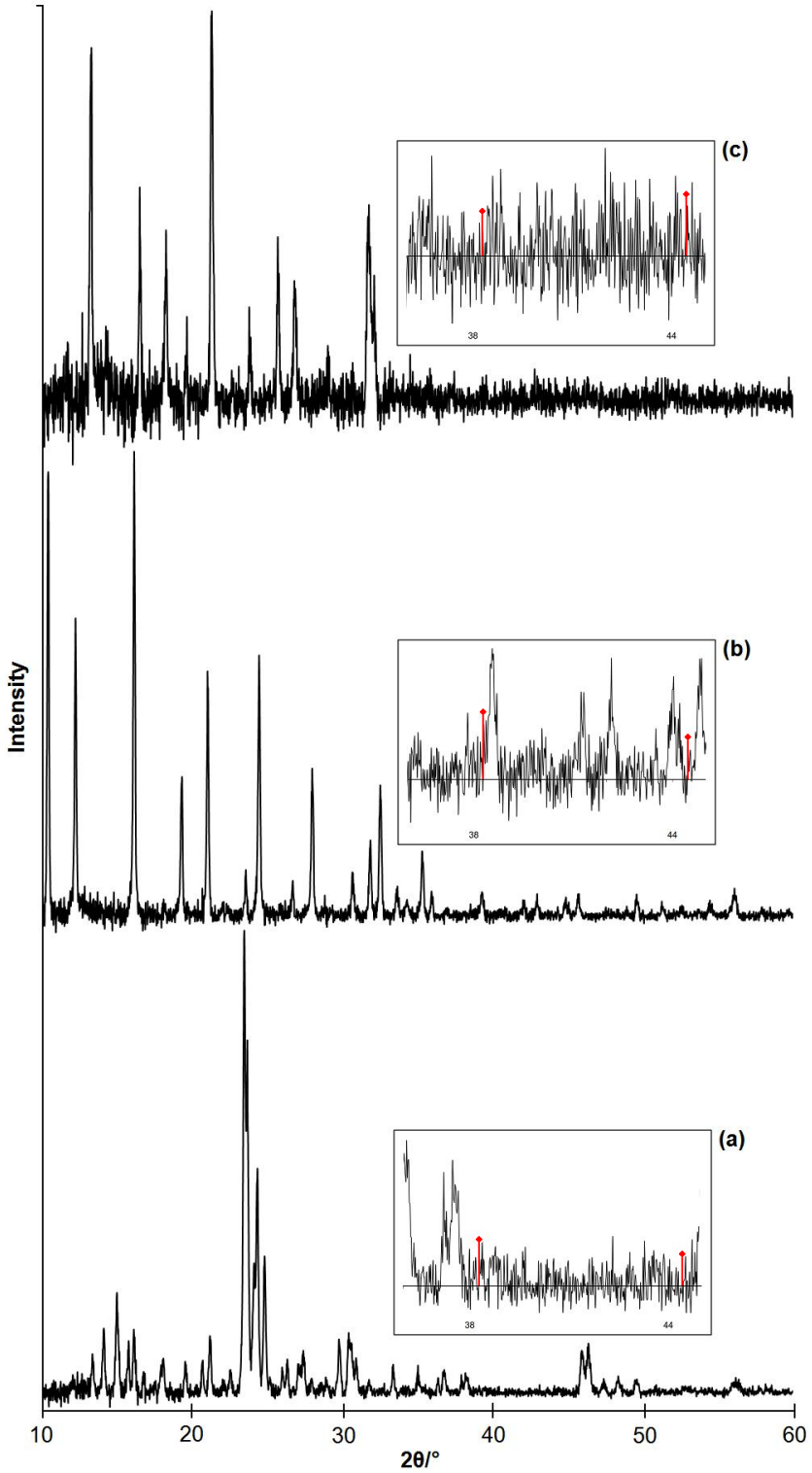

Figure 4.7: Diffraction pattern for (a) as-synthesized 0.05 wt% Au(III)/2:ZSM-5; (b) as-synthesized 0.09 wt% Au(III)/2:HY and (c) as-synthesized 0.06 wt% Au(III)/2:SAPO-34

4.5 X-ray Absorption Spectroscopy (XAS) analyses

4.5.1 Reference compounds

Gold foil, Au(I)Cl and as-synthesized 2.4 wt% tetraamminegold(III) nitrate (Au(III)/2) were used as reference compounds to analyze the synthesized and ion-exchanged Au samples. All data were collected at room temperature. Figure 4.8 represents the normalized XANES and the first derivatives of each compound. The spectra were normalized as described in Section 3.7.3. The normalized XANES are energy corrected against the gold L_{III}-edge value (11919.00 eV).

The spectrum of 2.4 wt% Au(III)/2, (e), show a prominent feature, called the white line, in the Au L_{III} near-edge region, centered at an energy 4 eV higher than that of the Au L_{III}-edge. Au(I)Cl, (b), have a small white line located 4 eV above the Au absorption edge. The white line is missing from the spectra of Au foils, (b), (c) and (d), due to the complete occupancy of the d states (the Au ground state electron configuration is $[Xe]4f^{14}5d^{10}6s^{1}$). Furthermore, the spectrum of Au(III)/2 shows a broad shoulder ranging from 30 eV to 60 eV above the Au L_{III}-edge. Note that the normalized XANES spectrum also has a shoulder located 15 eV above the Au absorption edge. According to results presented elsewhere[4,36,78] this shoulder should not be present in a normalized XANES spectrum of a pure trivalent gold compound (e.g. $HAuCl_4$). This indicates that the Au(III)/2 complex may not obtain a pure trivalent character. However, since there has not been reported any XANES spectra of divalent Au in the literature it is hard to determine the exact oxidation state for this Au complex. In addition, no other trivelent Au reference compound has been available for this work, hence the Au(III)/2 complex is assumed to be trivalent in this thesis.

The normalized spectra of the Au foil show distinct shoulders at 25 eV and 50 eV above the Au L_{III}-edge. These characteristic features clearly distinguishes the XANES of trivalent, monovalent and metallic Au from each other, and can be used fingerprints when determining the oxidation state of Au in the investi-

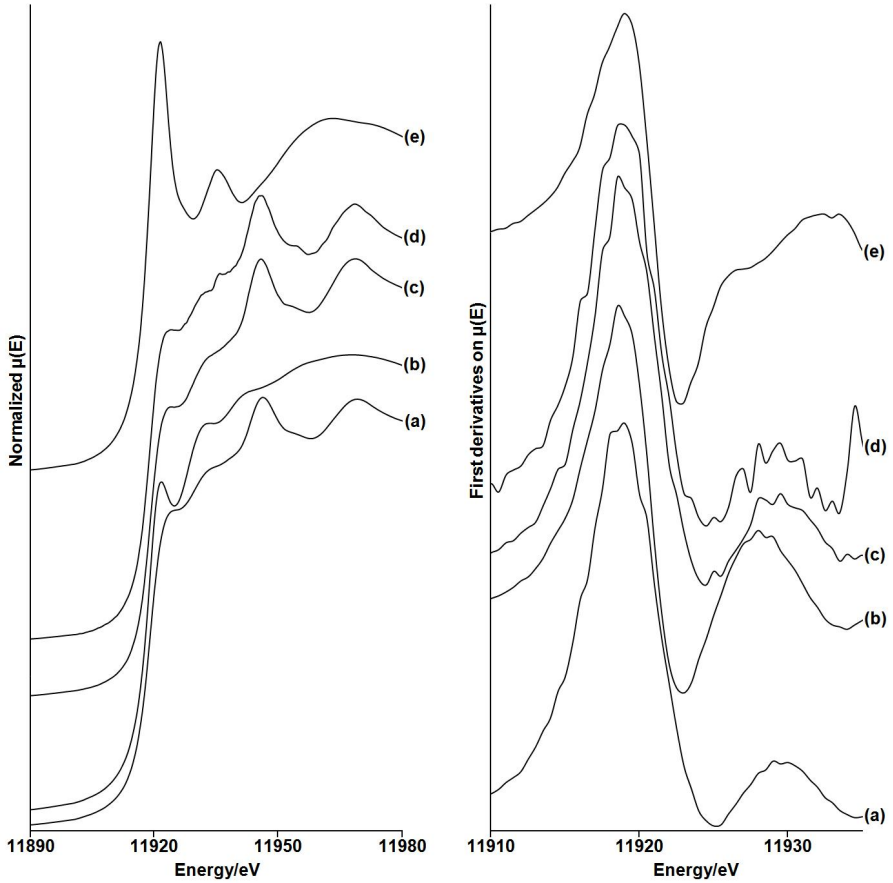

Figure 4.8: Normalized XANES and the first derivatives of (a) Au foil - detected in transmission mode at ESRF; (b) AuCl - detected in transmission mode at ESRF; (c) Au foil - detected in fluorescence mode at MAXlab; (d) Au foil - detected in fluorescence mode at ESRF and (e) 2.4 wt% tetraamminegold(III) nitrate (Au(III)/2) - detected in fluorescence mode at ESRF

gated Au zeotypic samples discussed later in this chapter. Excurve[71] was used to analyze the Au L_{III} data. The multiplicities were kept constant in accordance with crystallografic data[79], while the bonding distance (R, (Å)), thermal vibration (Debye-Waller factor, $2\sigma^2$) and amplitude reduction factor (AFAC) were determined through refining. Due to low signal to noise ratios, independent of the detection mode, the fit factors for the reference samples are somewhat higher than what would be desired. The EXAFS analyses result of the reference compounds are given in Table 4.6.

Table 4.6: Parameters from the least squares EXAFS analysis for the reference compound used for analysis of the Au L_{III}-edge data[a]

Sample	Detection mode	Shell	N	R (Å)	$2\sigma^2$ (Å^2)	R[a] (%)	AFAC
Au(I)Cl[b]	Trans.@ESRF	Au-Cl	2.0	2.291(4)	0.0066(6)	21.58	0.9851
		Au$\cdots$Au	2.0	3.10(4)	0.03(1)		
Au foil[b]	Trans.@ESRF	Au-Au	12.0	2.860(4)	0.0153(6)	29.81	0.8106
		Au$\cdots$Au	6.0	4.08(3)	0.024(3)		
Au foil[c]	Fluor.@MaxLab	Au-Au	12.0	2.888(7)	0.022(3)	53.40	1.0615
		Au$\cdots$Au	6.0	4.10(3)	0.024(8)		
Au foil[d]	Fluor.@ESRF	Au-Au	6.0	2.859(4)	0.0195(7)	47.71	1.0904
Au(III)/2[d]	Trans.@ESRF	Au-N	4.0	2.011(5)	0.004(1)	43.34	0.7363

[a] Analysis were preformed as described in Section 3.7.3
[b] $1.5 < k < 12.0$ Å^{-1}, $0.1 < r < 6.0$ Å
[c] $1.5 < k < 11.5$ Å^{-1}, $0.1 < r < 6.0$ Å
[d] $1.5 < k < 16.0$ Å^{-1}, $0.1 < r < 6.0$ Å

As a result of the various signal to noise ratios for the Au L_{III}-edge data collections, the reference compounds had to be fitted within different k-ranges in Excurve[71]. The r-values are the same for all refinements, ranging from 0.1 to 6.0 Å. The Au foil and Au(I)Cl detected in transmission mode, k-values from 1.5 to 12.0 Å^{-1} returned good fit factors (R (%)) and reasonable interatomic distances (R (Å)), according to literature[79]. Values for thermal vibration, the Debye-Waller factor, were also within an acceptable range.

Refinement of the Au L_{III}-edge data collected for the Au foil using fluorescence mode at MAXlab returned a high fitting factor of 53.40%. Due to a low signal to noise ratio a k-range not wider than 1.5-11.5 Å^{-1} was possible to refine. The refinement returned a higher first Au-Au interatomic distance R_{Au-Au} than what reported by Bailar *et al.*[79]. However, the refined interatomic distance (2.888 Å) is in accordance with values reported by Miller *et al.*[5], among others. The second Au-Au bonding distance is in accordance with literature[79]. For the Au foil detected in fluorescence mode at ESRF, it was only possible to fit the first Au shell. The refinement was preformed with k-values ranging from 1.5 to 16.0 Å^{-1}, returning a fit factor of 47.71%.

Analysis of the collected Au L_{III}-edge data for tetraamminegold(III) nitrate confirmed four neighboring nitrogen atoms located 2.011 Å from the core, in accor-

dance with the literature[79]. The refined AFAC values obtained from the analyses were used throughout the analyses of the synthesized and ion-exchanged Au zeotypic samples. The experimental and calculated k^3 weighted Au EXAFS and its Fourier Transform of the reference compounds are given in Figure 4.9.

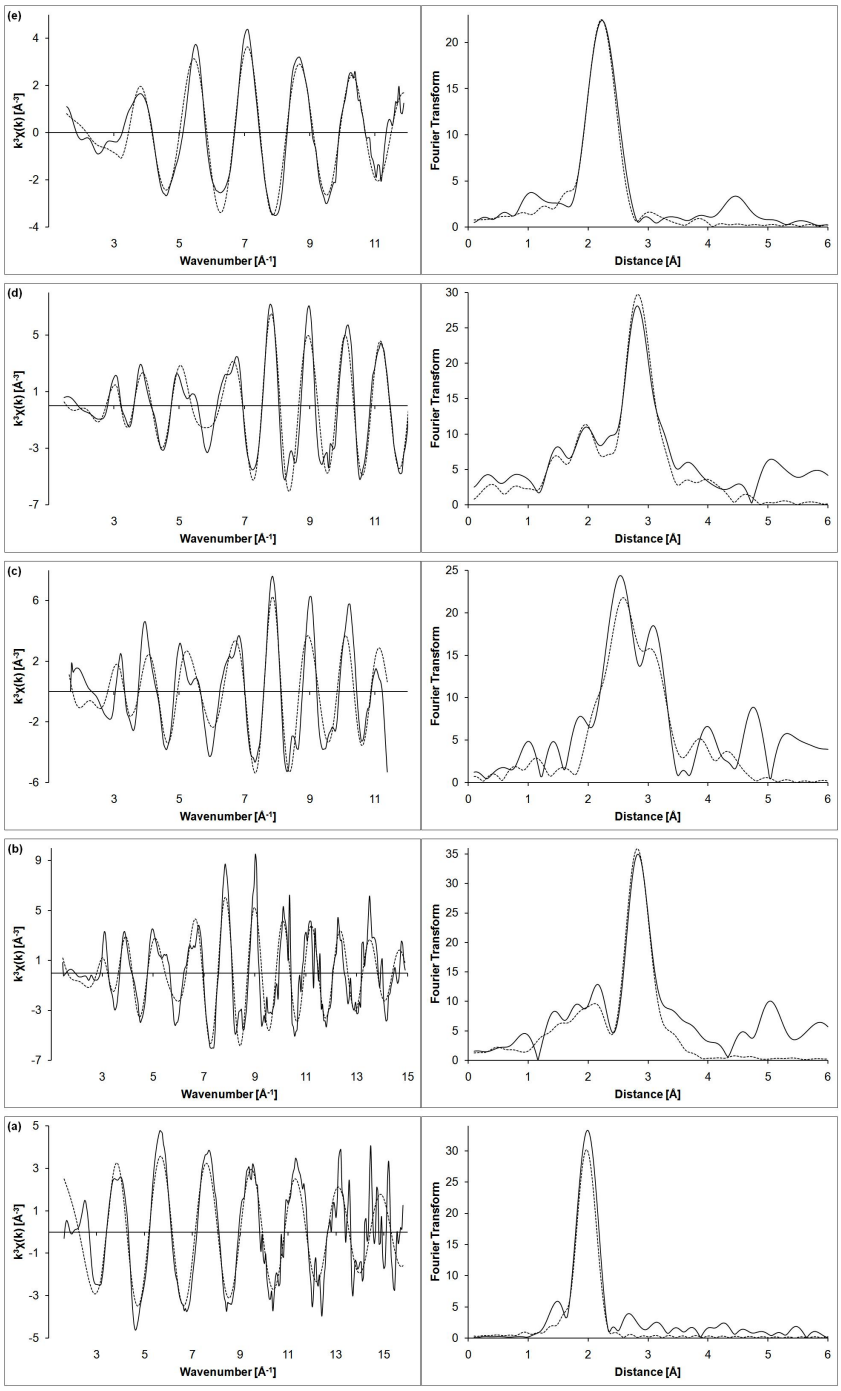

Figure 4.9: Experimental (-) and calcutalted ($\cdots$) k^3 weighted Au EXAFS and its Fourier Transform for (a) 2.4 wt% tetraamminegold(III) nitrate (Au(III)/2) - detected in fluorescence mode at ESRF; (b) Au foil - detected in fluorescence mode at ESRF; (c) Au foil - detected in fluorescence mode at MAXlab; (d) Au foil - detected in transmission mode at ESRF and (e) Au(I)Cl - detected in transmission mode at ESRF

4.5.2 Synthesized and hydrothermal ion-exchanged Au zeotypic samples

The normalized XANES and the first derivatives for the synthesized and hydrothermal ion-exchanged samples prepared by using a $1.16 \cdot 10^{-3}$ M Au solution are shown in Figure 4.10. The spectra were normalized and the threshold energy, E_0, were corrected as described in Section 3.7.3. The corrected threshold energies are given in Table 4.7. Note that Au:SAPO-34 is not analyzed. Due to an extreme low signal to noise ratio, it was not possible to obtain any information from the XANES and EXAFS data.

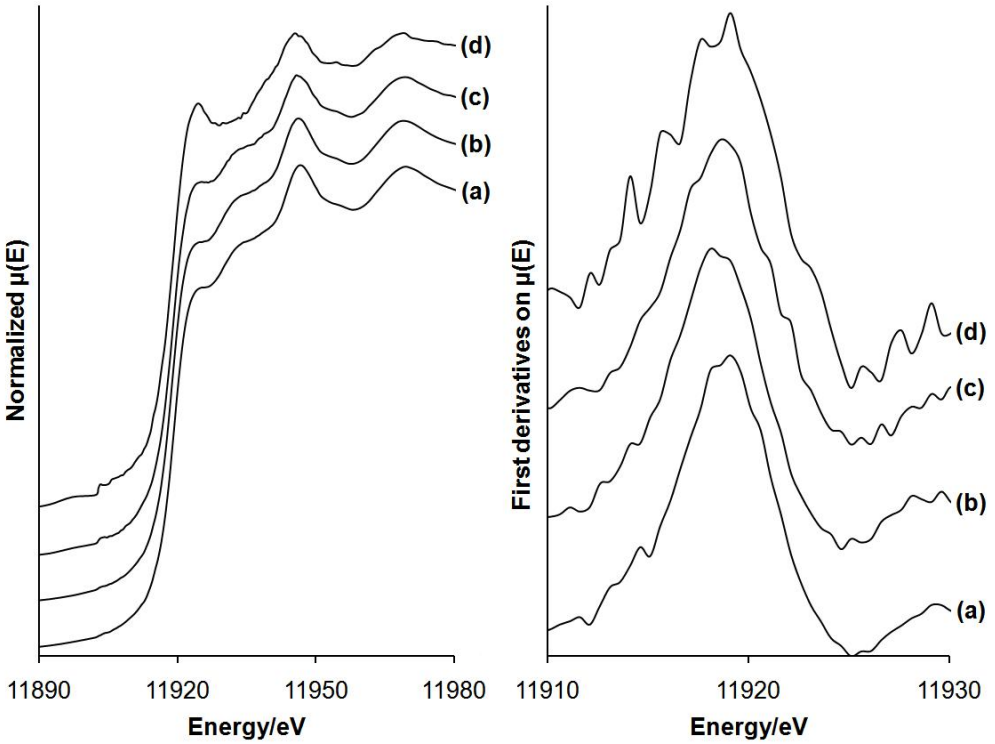

Figure 4.10: Normalized XANES and its first derivatives of (a) as-prepared 0.36 wt% AuSAPO-5; (b) calcined 0.45 wt% AuSAPO-5; (c) as-prepared 0.33 wt% Au:ZSM-5 and (d) as-prepared 0.24 wt% Au:HY. All samples are detected in transmission mode.

The normalized XANES for 0.36 wt% AuSAPO-5, calcined 0.45 wt% AuSAPO-5 and as-prepared 0.33 wt% Au:ZSM-5 show clear resemblance to the Au foil. The absence of a white line in addition to the two distinct sholders at 25 eV and 50 eV above the Au L_{III}-edge indicate a reduction of the cationic gold in samples

Table 4.7: Energy correlations for synthesized AuSAPO-5 and ion-exchanged Au samples prepared with $1.16{\cdot}10^{-3}$ M gold solution

Sample	**L_{III}-edge value** (eV)	**E_0 shift** (eV)
AuSAPO-5 as-prep.	11919.11	2.07
AuSAPO-5 calc.	11918.63	1.5
Au:ZSM-5 as-prep.	11918.96	2.0
Au:HY as-prep.	11918.96	1.7

to metallic gold atoms. The normalized XANES of as-prepared 0.24 wt% Au:HY showed a small white line located 4 eV above the Au L_{III} absorption edge, thus indicating that the gold cations in the sample may not have been fully reduced to its metallic gold atoms during the hydrothermal ion-exchange procedure. However, the spectrum show resemblance to the Au foil, having the same distinct shoulders located at 25 eV and 50 eV above the Au L_{III}-edge. For further XANES analyses, the normalized Au L_{III}-edge XANES were fitted with trivalent, monovalent and metallic gold reference compounds to determine the oxidation state of the gold present in the samples. As seen in Figure 4.11 Au:HY shows less metallic character than the other samples.

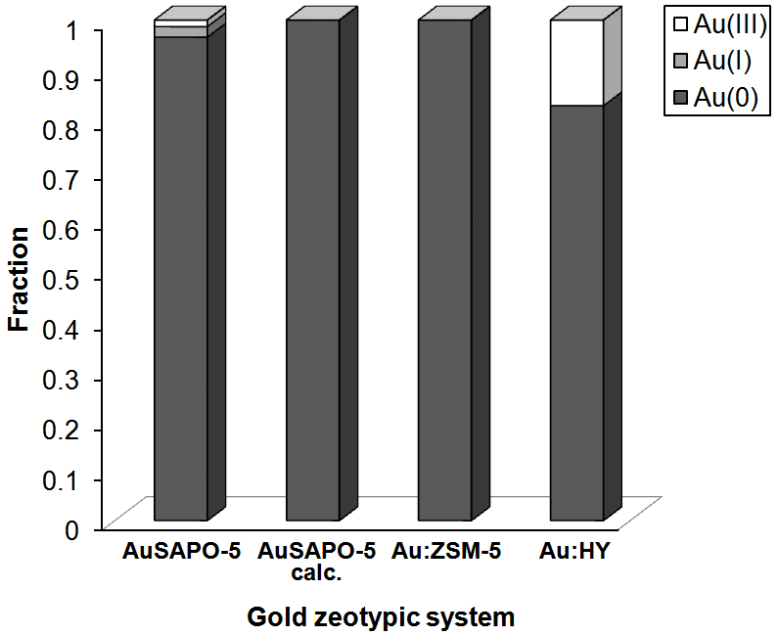

Figure 4.11: Linear combination of Au samples prepared with $1.16{\cdot}10^{-3}$ M Au solution

The linear combination indicates a reduction from trivalent to metallic character of the gold present in AuSAPO-5. The analysis returned a 96.6% fit to the Au foil, thus confirming an almost complete auto reduction of Au^{3+} during synthesis. In the calcined sample the Au^{3+} cations are fully reduced to metallic gold atoms, hence both the synthesis method and temperature treatment increases the reduction rate of the trivalent gold cations.

Analysis of the ion-exchanged sample Au:ZSM-5 also returned a 100% resemblance to the Au foil. This sample was prepared by hydrothermal ion-exchange, thus reducing the trivalent gold cations to metallic gold atoms during preparation in auto clave under relatively high temeratures and pressure. Au:HY were also prepared by hydrothermal ion-exchange, yet the gold in the sample do not show the same metallic character as Au:ZSM-5. Further analysis is nescessary to determine wether the trivalent gold cations in Au:HY is partially bonded to the acid sites of the zeolite, or if the cations have been reduced, i.e. agglomerated into gold nanoclusters (GNCs). For numerical result of the linear combination please see Appendix B.

Table 4.8: Parameters from the least squares EXAFS analysis for gold compound prepared with 0.0016 M Au solution used for analysis of the Au L_{III}-edge data[a]. AFAC is refined to be 0.8106 for the gold foil.

Sample	**Shell**	**N**	**R** (Å)	$\mathbf{2\sigma^2}$ (Å^2)	$\mathbf{R}$[a] (%)	$\mathbf{d_c}$[b] (nm)
AuSAPO-5 as-synth.[c]	Au-Au	10.9(7)	2.856(4)	0.0166(8)	43.00	6.31
AuSAPO-5 calc.[c]	Au-Au	11.3(7)	2.866(4)	0.0167(6)	41.26	12.18
Au:ZSM-5 as-synth.[d]	Au-Au	11.4(6)	2.866(3)	0.020(1)	48.49	16.82
Au:HY as synth.[d]	Au-Au	9.4(9)	2.866(7)	0.024(2)	57.63	2.35

[a] EXAFS analysis were preformed as described in Section 3.7.3
[b] Determined by modifying the calculations made by de Graaf *et. al*[39]
[c] $1.5 < k < 12.0$ Å^{-1}, $0.1 < r < 6.0$ Å
[d] $1.5 < k < 10.0$ Å^{-1}, $0.1 < r < 6.0$ Å

EXAFS analysis (Table 4.8) confirms a multiplicity very similar to the Au foil for the as-prepared AuSAPO-5. The sample has a multiplicity of 10.9 (versus 12.0 for the Au foil), ergo a complete reduction of the gold cations incorporated into the zeotype framework has occurred during synthesis. The bonding distance to the first Au shell is refined to be 2.856 Å, thus slightly shorter than what obtained for

the Au foil. Still, the gold atoms in the sample clearly has a metallic character. Calcined AuSAPO-5 has a multiplicity of 11.3 and a bonding distance of the first Au-Au shell similar to the Au foil. This confirms that calcination led to a agglomeration of the reduced gold atoms into fairly large GNCs (12.18 nm).

Analysis of Au:ZSM-5 also confirmed a high multiplicity (11.4) and the same bonding distance as the Au foil, thus confirming an reduction of the gold cations and a formation of large GNCs as the metallic gold atoms are assumed to have agglomerates. The GNC size is found to be 16.82 nm. EXAFS analysis of Au:HY states a multiplicity of 9.4 for the Au-Au shell. Since a Au-O shell was not possible to detect, the gold in the sample is present in its metallic character. The lower value of N_{Au-Au}, compared with the other samples, indicates formation of smaller gold nanoclusters (GNCs). The detection of a interatomic distance similar to the Au foil supports this assumption. The GNCs in Au:HY in found to be 2.35 nm. Experimental and calculated k^3 weighted Au EXAFS and its Fourier Transform for the samples is shown in Figure 4.12.

Table 4.9: Values of the nearest-neighbor distance ($R_{Fourier}$) of Au clusters and multiplicity (N) made by Balerna *et al.*[80]

D (Å)	$\mathbf{R}_{Fourier}$ (Å) (±0.02 Å)	**N** (±10%)
11.0	2.82	-
15.0	2.83	9.4
20.0	2.84	9.6
24.0	2.85	10.0
30.0	2.86	10.6
42.0	2.87	11.0
60.0	2.87	-
bulk	-	12.0

Calculations on GNC sizes of evaporated small Au clusters made by Balerna *et al.*[80] are represented in Table 4.9. Comparison of the obtained bonding distances for the gold zeotypic samples with those calculated by Balerna *et al.* clearly state that the GNC sizes in the samples are in the range from 4.2- 6.0 nm. As mentioned in Section 2.2.3, large GNC sizes gives rise to low dispersion, which lowers the activity and depreciate the catalytic ability. As represented in Table 4.8 measuring

the GNC size as described by Graaf *et al.*[39], using the multiplicity for the first Au-Au shell, gives rise to different GNC sizes. However, the GNC sizes obtained are too large in a catalytic perspective, with the exception of Au:HY. This sample may be interesting for activation measurements for CO oxidation.

Direct incorporation of gold(III)chloride hydrate during synthesis of SAPO-5 led to an auto reduction of the trivalent Au present in the precursor. In addition, other factors such as light and heat may have influenced the formation of metallic GNCs during synthesis. As mentioned earlier cationic gold is very sensitive to light and can easily auto reduce and agglomerate when exposed to light. After synthesis the obtained powder was dried at 100 °C for 24 hours. If not completely reduced during synthesis, the gold cations clearly lost their trivalent character at this point. The hydrothermal ion-exchange clearly auto reduced the Au^{3+} cations in Au:ZSM-5. All though analysis of Au:HY did not return a as high multiplicity as refined for Au:ZSM-5, it still had a bonding distance similar to what is known for the Au foil, thus confirming that the GNC size is smaller in this sample compared to AuSAPO-5 and Au:ZSM-5.

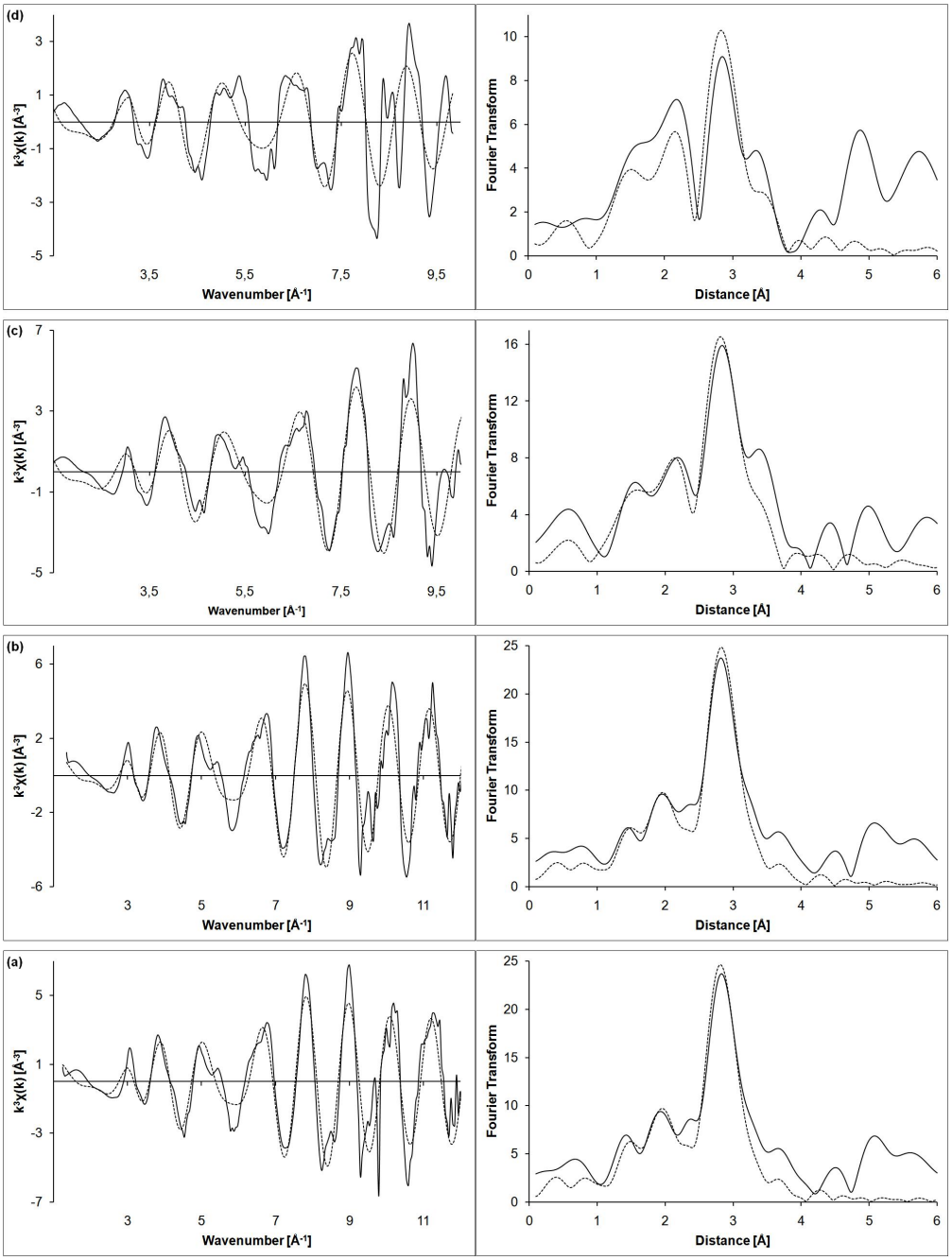

Figure 4.12: Experimental (-) and calcutalted ($\cdots$) k^3 weighted Au EXAFS and its Fourier Transform for (a) as-prepared 0.36 wt% AuSAPO-5; (b) calcined 0.45 wt% AuSAPO-5; (c) as-prepared 0.33 wt% Au:ZSM-5; (d) as-prepared 0.24 wt% Au:HY. All samples are detected in transmission mode at SNBL01 at ESRF

4.5.3 Conventional ion-exchanged Au(III)/1 zeotypic samples

XAS Au L_{III}-edge data for the as-prepared zeotypic samples 0.07 wt% Au(III)/1:ZSM-5, 0.17 wt% Au(III)/1:HY and 0.07 wt% Au(III)/1:SAPO-34 were detected in fluorescence mode at beamline I811 at MAXLab, Sweden. The normalized XANES and the first derivatives for the samples are shown in Figure 4.13. Athena[70] was used for normalization and threshold energy correction of the data as described in Section 3.7.3. Correction in the threshold energies, E_0, are listed in Table 4.10.

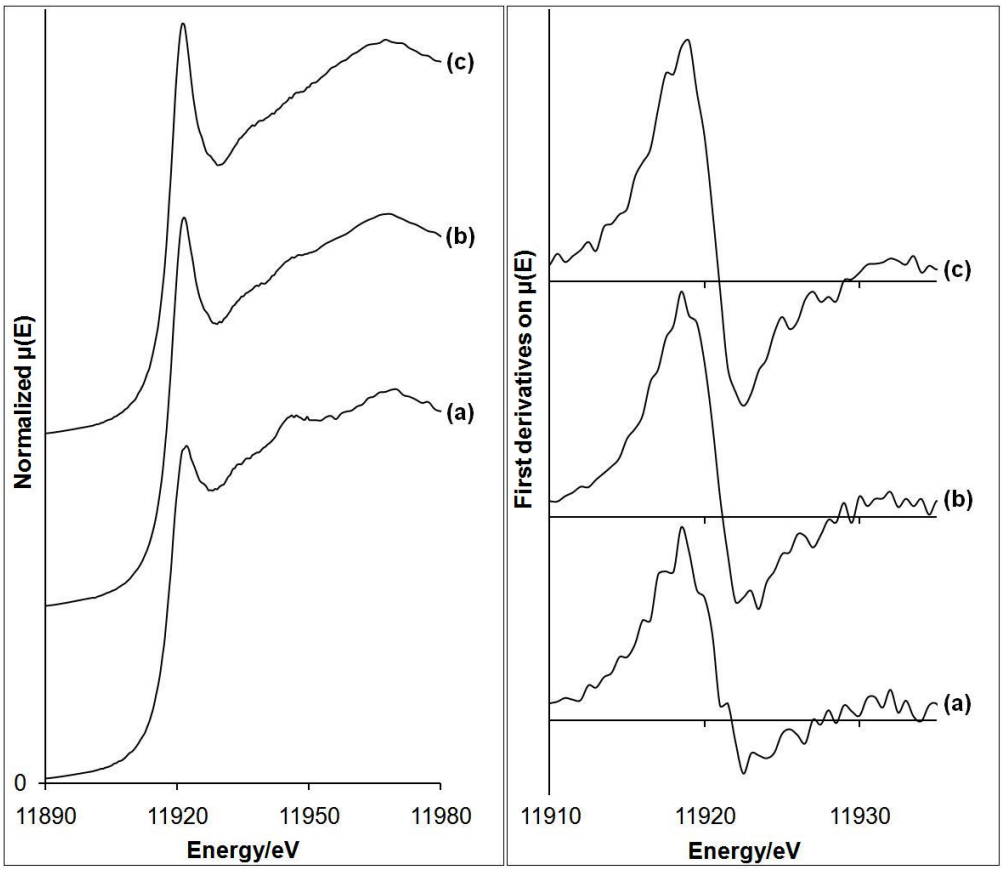

Figure 4.13: Normalized XANES and its first derivatives of (a) as-prepared Au(III)/ZSM-5; (b) as-prepared Au(III)/1:HY and (c) as-prepared AU(III)/1:SAPO-34

The normalized XANES spectra of Au(III)/1:SAPO-34 has an intense white line at $\approx$ 11923 eV. The white line is also present for the two other samples, though not as striking. The intensity of the white lines can be used as a indicator for the presence

Table 4.10: Energy correlations for ion-exchanged Au samples prepared with tetraammine-gold(III) nitrate (Au(III)/1) solution

Sample	**L_{III}-edge value** (eV)	**E_0 shift** (eV)
Au(III)/1:ZSM-5 as-prep.	11917.66	0.8
Au(III)/1:HY as-prep.	11918.70	1.0
Au(III)/1:SAPO-34 as-prep.	11918.37	0.8

of trivalent gold cations in the samples, as a high white line intensity represents the degree of unoccupied $5d$ orbitals, i.e. $5d^7$ having a higher white line intensity than $5d^8$, and so on. By peak fitting the white lines in Athena[70], a measure of the area under the peak, i.e. the presence of cationic gold in the samples, can be obtained. As illustrated in Figure 4.14 analysis concludes that Au(III)/1:SAPO-34's white line has the largest area, followed by Au(III)/1:HY, while Au(III)/1:ZSM-5 yields the smallest area, thus indicating the degree of trivalent gold in the following order: Au(III)/1:SAPO-34 > Au(III)/1:HY > > Au(III)/1:ZSM-5. Table 4.11 represents the result from the peak fitting.

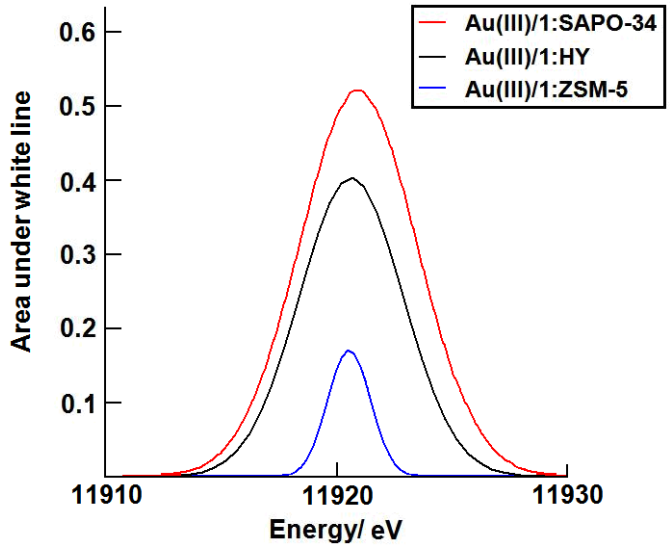

Figure 4.14: Peak fitting of ares under white line for the ion exchanged Au(III)/1 samples

The normalized XANES of both Au(III)/1:SAPO-34 and Au(III)/1:HY seems to have the same characteristic features as the Au(III) source. The normalized XANES of Au(III)/1:ZSM-5 shows a small white line similar to the trivalent Au

Table 4.11: Peak fitting of area under the white line for the ion-exchanged Au(III)/1 samples

Sample	Centroid	Function	Amplitude	Width	R factor (10^{-4})
Au(III)/1:ZSM-5 as-prep.	11921.1(3)	Gauss	0.87(9)	1.8(1)	6.2
Au(III)/1:HY as-prep.	11920.6(3)	Gauss	2.3(1)	2.24(7)	7.3
Au(III)/1:SAPO-34 as-prep.	11920.9(3)	Gauss	3.0(1)	2.30(7)	9.9

source. However, it also shows some similarities to the Au foil. Small, but still evident shoulders appear in the XANES spectrum at 25 eV and 50 eV above the Au L_{III}-edge. Since the normalized XANES show both features in accordance with both the Au(III) source and the Au foil, it is likely to believe that the gold in Au(III)/1:ZSM-5 is partially reduced from Au^{3+}. However, due to the low intensity of the white line it is likely to believe that Au(III)/1:ZSM-5 is the sample having the lowest oxidation state of the three investigated samples, yet having a somewhat cationic character. Linear combination of each of the three ion-exchanged samples with a trivalent, a monovalent and a metallic gold source gives an indication of the oxidation state for the gold present in the zeotypic samples. The results are shown in Figure 4.15. Numerical values are given in Appendix B.

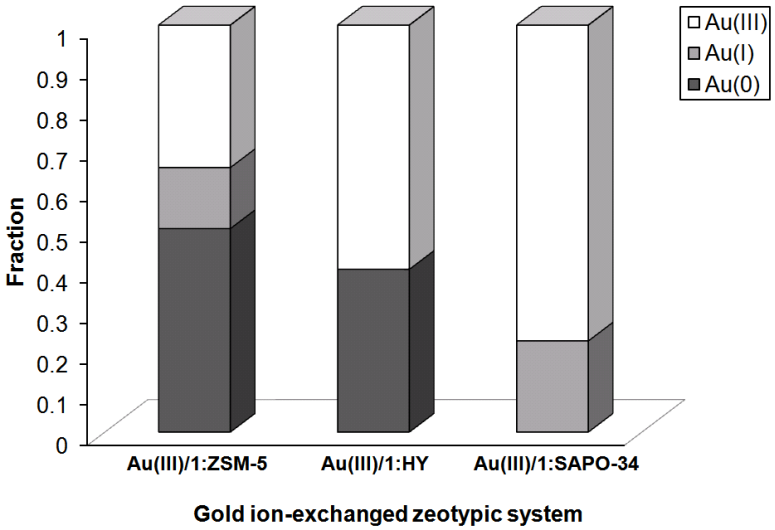

Figure 4.15: Linear combination of the ion-exchanged Au(III)/1 samples at room temperature

As suspected from the normalized XANES, the gold cations in Au(III)/1:ZSM-5 have been reduced from trivalent gold. The linear combination fit suggests a 50% fit with the Au foil, and a 15% and 35% fit with the Au(I) and Au(III) sources, respectively. It is hard to draw any conclusion regarding the exact oxidation state of the gold cations in Au(III)/1:ZSM-5 based on this analysis. However, the sample has clearly been reduced during the conventional ion-exchange procedure, although an auto reduction has not occoured as was the case for Au:ZSM-5 prepared by the hydrothermal ion-exchange method (Section 4.5.2). In addition, the partial reduction of the Au^{3+} indicates formation of small gold nanoclusters (GNCs) in the sample.

The trivalent gold cations in Au(III)/1:HY has also been reduced, yet not to the same extent as shown for Au(III)/1:ZSM-5. According to the linear combination, the gold in the sample show a 60% resemblance to the Au(III) source and 40% to the Au foil. The resemblance to trivalent Au for the sample is therefore higher than what detected for Au:HY prepared by hydrothermal ion-exchange. Based on the linear combination of Au(III)/1:HY it seems that 60% of the cationic gold atoms are still bonded to the acid sites of the zeolite, while the remaining 40% have agglomerated into small GNCs.

Au(III)/1:SAPO-34 is by far the sample who shows the greatest resemblance to the trivalent Au source having a 77.6% fit to the Au(III) source. However, the oxidation state for the cationc gold in the sample are not assumed to be trivelent as the sample also shows a 22.4% resemblance to the monovalent Au source. Still, the linear combination results did not conclude any metallic Au present in the samples since none of them returned a 100% fit to the Au foil. Based on the results from the linear combination the degree of reduction of Au^{3+} to Au^{0} is highest for Au(III)/1:ZSM-5, followed by Au(III)/1:HY and Au(III)/2:SAPO-34. However, further analyses are required to draw any conclusions. The numerical results of the linear combination are given in Appendix B.

Excurve[71] was used to determine the coordination number, hence the cluster size, for the gold clusters in the ion-exchanged zeotypic materials. Au(III)/1:SAPO-34

and Au(III)/1:ZSM-5 were fitted with k-values ranging from 1.5 to 11.0 Å^{-1} and Au(III)/1:HY in the k-range 1.5 to 10.0 Å^{-1}. The r-values range from 0.1 to 6.0 Å for each of the three samples. The results from the analysis is presented in Table 4.12 and Figure 4.17.

Table 4.12: Parameters from the least squares EXAFS analysis for ion-exchanged gold samples prepared with 0.05 M Au(III)/1 solution used for analysis of the Au L_{III}-edge data[a]. AFAC is refined to be 1.0615 for gold foil and 0.7363 for tetraamminegold(III)nitrate.

Sample	**Shell**	**N**	**R** (Å)	**$2\sigma^2$** (Å^2)	**R**[a] (%)	**d_c**[b] (nm)
Au(III)/1:ZSM-5[c]	Au-O	1.0(2)	1.97(1)	0.011(4)	55.04	
as-synth.	Au-Au	3.1(2)	2.795(4)	0.0098(9)		
Au(III)/1:HY[d]	Au-O	2.5(1)	2.010(4)	0.001(2)	32.58	0.66
as-synth.	Au-Au	4.4(6)	2.859(9)	0.020(2)		
Au(III)/1:SAPO-34[c]	Au-O	3.2(2)	2.023(6)	0.011(2)	47.73	
as-synth.						

[a] EXAFS analysis were preformed as described in Section 3.7.3
[b] Determined by modifying the calculations made by de Graaf *et al.*[39]
[c] $1.5 < k < 11.0$ Å^{-1}, $0.1 < r < 6.0$ Å
[d] $1.5 < k < 10.0$ Å^{-1}, $0.1 < r < 6.0$ Å

EXAFS analysis of as-synthesized Au(III)/1:ZSM-5 concludes one neighboring oxygen atoms located 1.97 Å from the core and ≈ 3 gold atoms at a bonding distance of 2.795 Å. The detection of an oxygen neighboring atoms confirms that a partial reduction of the Au^{3+} atoms have occurred. The sample clearly consists of small GNCs as both N_{Au-O} and Au_{Au-Au} have been detected. Due to the a low value of N_{Au-Au} is was not possible to determine the GNC size using the modeling and calculations prepared by de Graaf *et al.*[39], as described in Section 2.2.4. Two neighboring shells are also detected for Au(III)/1:HY; the first shell consisting of ≈ 2.5 oxygen atoms 2.01 Å from the core; the second a gold shell consisting of ≈ 4.4 gold atoms with a bonding distance of 2.859 Å. Both N_{Au-O} and N_{Au-Au} refined for Au(III)/1:HY is higher than what detected for Au(III)/1:ZSM-5. The size of the GNCs was found to be 0.66 nm for this sample.[39] Au(III)/1:SAPO-34 has only one neighboring shell with 3.2 oxygen atoms at 2.023 Å. The absence of a first Au-Au shell clearly indicates, if not a pure trivalent, then close to a trivalent character for the Au atoms in the sample.[4] In addition, the absence of a first Au-

Au shell indicates an atomic dispersion of Au cations on the surface. Figure 4.16 represent an assumption of how the Au^{3+} atoms are bonded to the acid sites of the zeolites ZSM-5 and HY, and the zeotype SAPO-34 at room temperature.

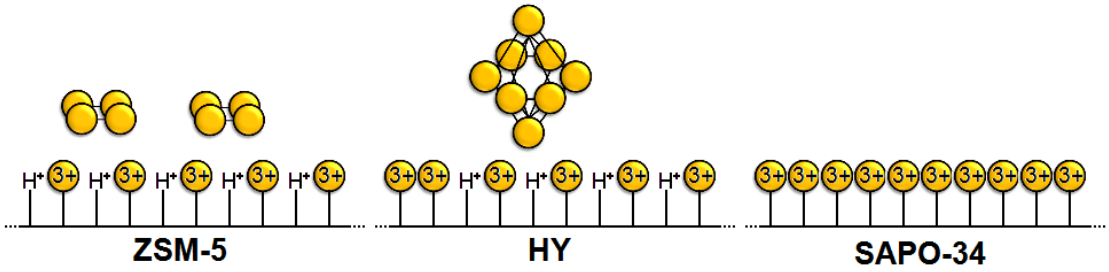

Figure 4.16: Au-support interactions for the samples Au(III)/1:ZSM-5, Au(III)/1:HY and Au(III)/2:SAPO-34 at room temperature

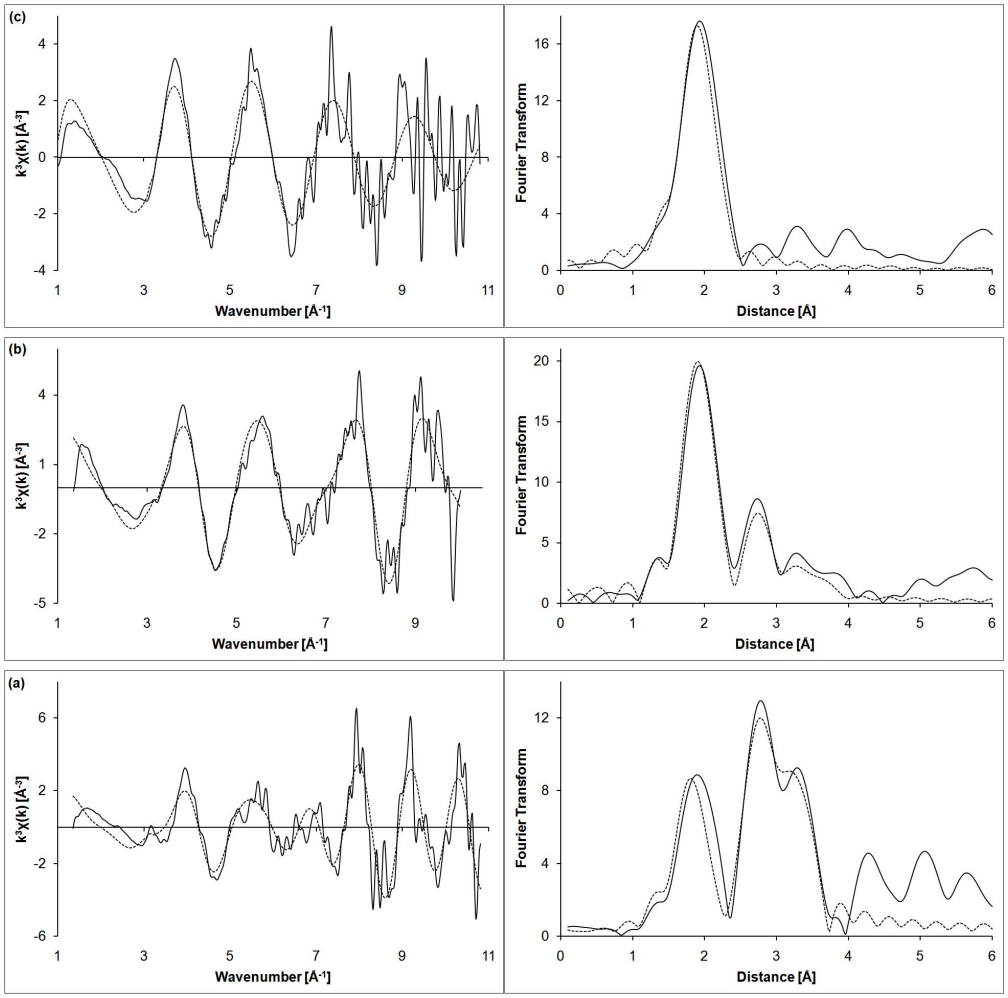

Figure 4.17: Experimental (-) and calcutalted ($\cdots$) k^3 weighted Au EXAFS and its Fourier Transform for (a) as-prepared Au(III):ZSM-5; (b) as-prepared Au(III)/1:HY and (c) as-prepared Au(III)/1:SAPO-34. All samples are detected in fluorescence mode at I811 at MAXlab

4.6 XAS in-situ studies

4.6.1 In-situ studies of Au(III)/1:ZSM-5

The in-situ XAS data were collected as described in Section 3.7.2. Figure 4.18a illustrates the Au L_{III}-edge XANES spectra of 2.4 wt% Tetraamminegold(III) nitrate (Au(III)/2, bold dashed line), the Au foil (dashed line), 0.07 wt% Au(III)/1:ZSM-5 at room temperature (bold solid line) and the heating process from 150 °C to 450 °C in a H_2 rich atmosphere (solid lines). The first dervivatives of the normalized XANES are given in Figure 4.18c. The XANES are normalized and energy corrected as described in Section 3.7.3.

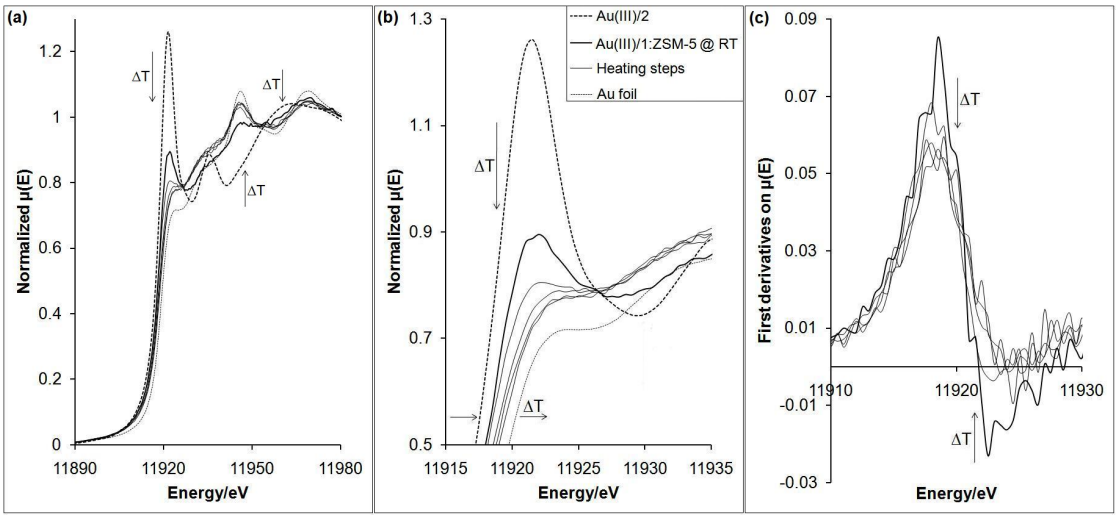

Figure 4.18: Normalized XANES and its derivatives for as-prepared 0.07 wt% AU(III)/1:ZSM-5 during the in-situ experiment

The XANES spectrum of Au(III)/1:ZSM-5 clearly indicates a reduction of oxidation state of the GNCs present in the sample already at room temperature. The presence of small, but still evident shoulders at 25 eV and 50 eV above the Au L_{III}-edge is similar to the Au foil. However, the appearance of a small white line at $\approx$ 11923 eV state that the Au^{3+} atoms have not undergone an auto reduction as was the case for the ion-exchanged samples discussed in Section 4.5.2. When heated from 150 °C to 450 °C in a hydrogen flow, the sample clearly differ from Au(III)/2 in three areas. At $\approx$ 11923 eV the white line intensity decreases; between $\approx$ 11943 eV and 11962 eV the normalized μ(E) increases and at $\approx$ 11962

Table 4.13: Correlations in the threshold energies for Au(III)/1:ZSM-5 during the in-situ measurement

Temperature (°C)	**Atmosphere**	**L_{III}-edge value** (eV)	**E_0 shift** (eV)
RT	Air	11917.66	0.8
150	100% He	11918.05	0.8
150	5% H_2 in He	11918.14	0.8
350	5% H_2 in He	11918.71	0.8
450	5% H_2 in He	11918.99	0.8
RT	0.6% NO in He	11919.00	0.8

eV the normalized μ(E) decreases. Although the shape of the XANES spectra for the heating steps are similar to the Au foil, it is still dubiously to conclude that a complete reduction of the Au^{3+} atoms present in the sample has occurred. An interesting point to stress is the shift in the threshold energies during the in-situ process. Normally, the threshold energy tend to decrease as the oxidation state decreases, due to the effective nuclear charge of the core. As listed in Table 4.13 and shown in Figure 4.18b the threshold energies increase as the oxidation states for gold decreases. The trend is also reported elsewhere,[4] however, no explanation to the trend has been given.

The Au L_{III}-edge XANES were fitted with the spectrum of the Au foil, Au(I)Cl and Au(III)/2 using a least-square method in Athena[70] to determine the oxidation state of the gold during the in-situ process. Results from the linear combination are given in Figure 4.19. The analysis points out that the Au atoms in Au(III)/1:ZSM-5 were far from trivalent even at room temperature, returning a 50% fit to the Au foil and 15% and 35% fit to the Au(I) and Au(III) source, respectively. At 150 °C in a helium flow the sample showed a 61% resemblance to the Au foil. The similarity to the Au(I) source increased to 23% while the samples showed less accordance with the Au(III) source as the analysis returned a fit of 16%. When the atmosphere was changed to 5% H_2 in He, the sample showed a even higher metallic character as the analysis returned a 68% fit to the Au foil, a 21% fit to the Au(I) source and 11% fit to the Au(III) source. These values were stable as the sample was further heated up to 450 °C in the hydrogen rich atmosphere.

The last linear comparison were carried out at room temperature in a 0.6% NO in helium atmosphere. The linear combination returned a 85% fit to the Au foil and 6% and 9% fit to the Au(I) and Au(III) source, repectively. Based on the linear combination, the Au zeolitic sample clearly show more resemblance to the Au foil than to the Au(III) source. However, the analysis only confirms a reduction of oxidation state of the gold atoms, hence more analyses are required to obtain the exact oxidation states of the gold present in the sample. For numerical values of the linear combination, please see Appendix B.

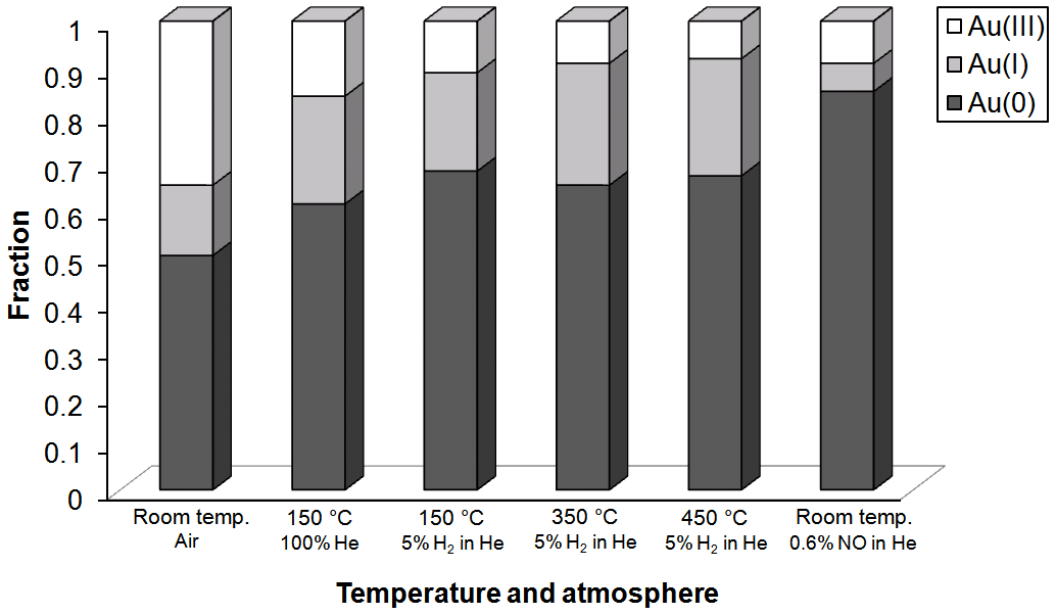

Figure 4.19: Fraction of metallic, cationic and trivalent gold present in Au(III)/1:ZSM-5 at varying temperatures and atmospheres determined by linear combination

The structural parameters obtained from the EXAFS analysis is given in Table 4.14. Due to low signal to noise ratios at 350 °C and 450 °C the data could only be fitted with k-values ranging from 1.5 to 9.0 $Å^{-1}$. Note that there was not performed any data collection at 250 °C due to beam problems during the in-situ experiment. The detection of both a oxygen and a gold neighboring shell at room temperature indicates a partial reduction of the trivalent gold atoms present in the sample. The detection of an oxygen shell confirms that some of the Au^{3+} atoms are bonded to the acid sites of the zeolite, while the detection of an Au-Au shell

confirms that some of the gold atoms have been reduced at room temperature and agglomerated into small gold nanoclusters (GNCs). The oxygen shell is refined to consist of one oxygen atom and is located 1.97 Å from the core. This bonding distance is in accordance with results reported by van Bokhoven *et al.*[4] on a investigated Au/Al_2O_3 sample. The neighboring gold shell consist of ≈ 3 gold atoms located 2.795 Å from the central atom. The bonding distance is much shorter than what expected for the Au foil (2.860 Å), hence the sample consists of Au^{3+} atoms bonded to the acid sites of the zeolite combined in addition to small GNCs.

Table 4.14: Parameters from the least squares EXAFS analysis for as-prepared 0.07 wt% Au(III)/1:ZSM-5 prepared with 0.05 M Au(III)/1 solution used for analysis of the Au L_{III}-edge data[a]. AFAC is refined to be 1.0615 for the Au foil and 0.7363 for tetraamminegold(III)nitrate (Au(III)/2).

Temp. (°C)	**Atm.**	**Shell**	**N**	**R** (Å)	**$2\sigma^2$** (Å²)	**R**[a] (%)	**d_c**[b] (nm)
RT[c]	Air	Au-O	1.0(2)	1.97(1)	0.011(4)	55.04	
		Au-Au	3.1(2)	2.795(4)	0.0098(9)		
150[c]	100% He	Au-O	0.4(1)	1.92(3)	0.009(9)	59.73	
		Au-Au	5.3(5)	2.839(5)	0.016(1)		0.74
150[c]	5% H_2 in He	Au-Au	7.6(7)	2.818(6)	0.021(1)	59.17	1.37
350[d]	5% H_2 in He	Au-Au	8.4(9)	2.833(8)	0.033(2)	65.78	1.67
450[d]	5% H_2 in He	Au-Au	10(1)	2.83(1)	0.043(3)	61.42	2.98
RT[c]	0.6% NO in He	Au-O	0.5(2)	2.0(1)	0.02(4)	49.23	
		Au-Au	8.4(5)	2.853(4)	0.01(1)		1.67

[a] EXAFS analysis were preformed as described in Section 3.7.3
[b] Determined by modifying the calculations made by de Graaf *et al.*[39]
[c] $1.5 < k < 11.0$ Å^{-1}, $0.1 < r < 6.0$ Å
[d] $1.5 < k < 9.0$ Å^{-1}, $0.1 < r < 6.0$ Å

When heated to 150 °C in a helium rich atmosphere, an oxygen shell is still possible to refine in addition to the first gold shell. Thus, some of the trivalent gold atoms are still bonded to the acid sites of the zeolite. The multiplicity of the oxygen shell has decreased as the analysis returns only 0.4 neighboring oxygen atoms located 1.92 Å from the central atom. At the same time the multiplicity of the gold shell increases, yielding 5.3 neighboring gold atoms located ≈ 2.84 Å from the core. The

decrease of N_{Au-O} and increase of N_{Au-Au} clearly indicates more of the trivalent Au atoms have been reduced and agglomerated into small GNCs. The GNC size is calculated to be 0.74 nm at this stage. When changing the atmosphere to 5% H_2 in He, the oxygen shell was no longer possible to refine, thus indicating that all the gold in the sample is present as small GNCs. The analysis confirmed a gold shell consiting of 7.6 gold atoms at a bonding distance $\approx$ 2.82 Å from the core. The decrease in bonding distance from 2.84 Å to 2.82 Å is probably a result of the missing oxygen shell in addition to some thermal vibration in the lattice, indicated by the increase in the Debye-Waller from 0.016 to 0.021. The GNC size is calculated to be 1.37 nm.

At 350 °C in the same atmosphere, both the multiplicity and the bonding distance to the neighboring gold shell increases as expected. The N_{Au-Au} was refined to be 8.4, thus confirming an additional agglomeration of the small GNCs. The gold shell is located $\approx$ 2.83 Å from the core. Both the values for N_{Au-Au} and R_{Au-Au} are smaller than what refined for the Au foil. Note that the Debye-Waller factor ($2\sigma^2$) is a somewhat high, yet, within an acceptable limit. At 450 °C the multiplicity is further increased as the refinement returns a N_{Au-Au} value of 10. The gold shell is located 2.83 Å from the core. As a result of the low signal to noise ratio the standard deviations in this value are higher than what would be desired. The Debye-Waller factor is also high due to thermal vibrations within the zeolite lattice. However, the refinement confirms that the GNCs have increased in size as the cluster diameter is found to be 2.98 nm.

As the zeolitic sample is cooled down to room temperature in an oxidizing atmosphere, a neighboring oxygen shell is possible to be detected in addition to the first Au-Au shell. The oxygen shell, consisting of 0.5 oxygen atoms, is located 2 Å from the central atom. This indicates that a fraction of the GNCs in the sample have been oxidized and formed bonds with some of the acid sites on the zeolite. The multiplicity of the refined gold shell sunk from 10 to 8.4 when the sample was cooled down from 450 °C to room temperature. R_{Au-Au} on the other hand, is refined to increase from 2.83 Å to 2.85 Å. The decrease in R_{Au-Au} is expected since the oxygen shell located closer to the core will lead to a longer bonding distance

between the central atom and the gold shell. The detection of an oxygen shell in this atmosphere indicates that the sample possesses some oxidizing capacity. The GNC size is found to be 1.67 nm. The experimental and calculated k^3 weighted Au EXAFS and its Fourier Transform for 0.07 wt% Au(III)/1:ZSM-5 at evaluated temperatures and atmospheres is given in Figure 4.20.

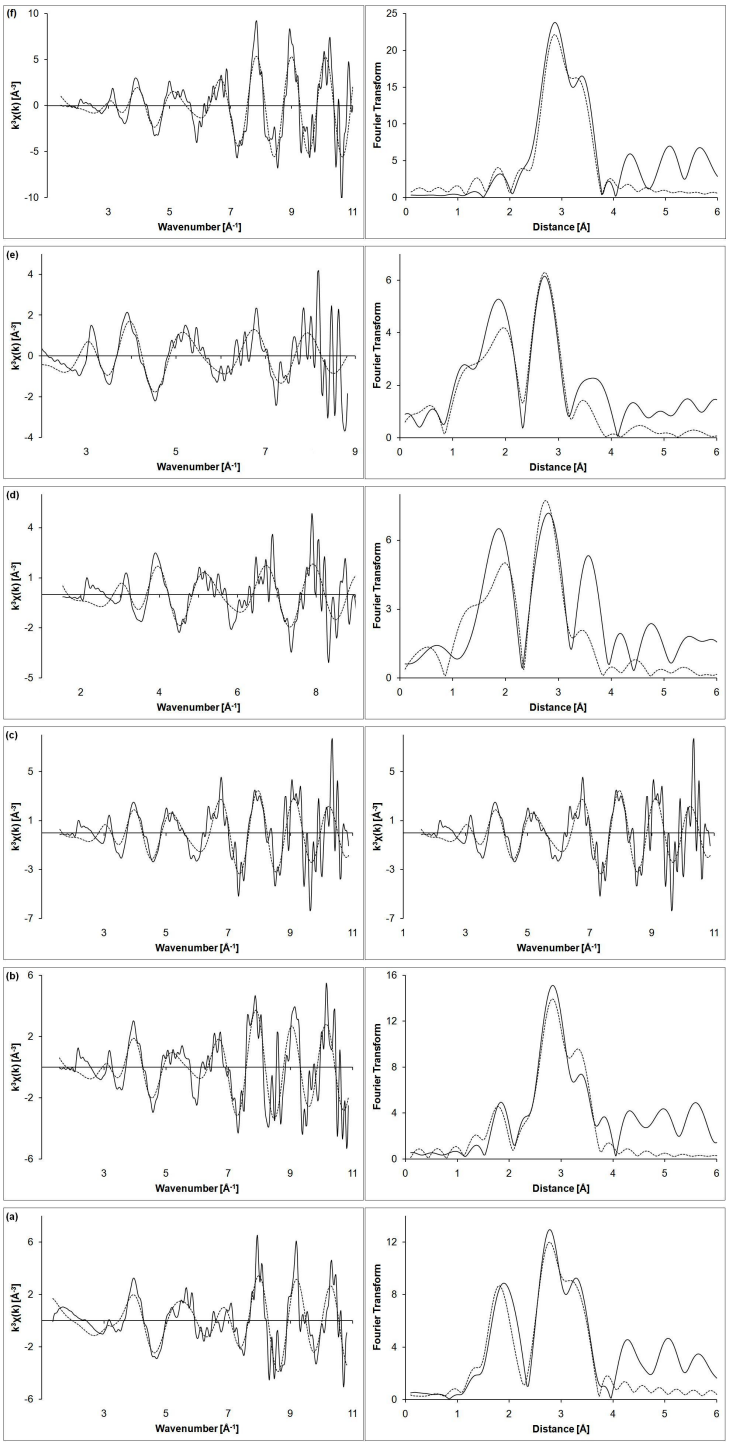

Figure 4.20: Experimental (-) and calculated ($\cdots$) k^3 weighted Au EXAFS and its Fourier Transform for 0.07 wt% Au(III)/1:ZSM-5 at (a) room temperature in air; (b) 150 °C in 100% He; (c) 150 °C in 5% H_2 in He; (d) 350 °C in 5% H_2 in He; (e) 450 °C in 5% H_2 in He and (f) room temperature in 0.6% NO in He

Based on the obtained first shell N_{Au-Au} and the GNC sizes throughout this EXAFS analysis and first shell N_{Au-Au} versus GNC sizes reported elsewhere,[3,4,5,6,35,36] a suggestion of possible numbers of Au atoms per GNC in Au(III)/1:ZSM-5 are presented in Figure 4.21. Please note that there has not been performed stability studies on the suggested Au_n (n being the number of Au atom(s)) and symmetries suggested. Take Au_{50} as an example. This agglomerate may have an infavourable symmetry compared to for instance Au_{52} with respect to energy stabilization and other structural variables. However, the figure gives an overview of which agglomerates that represents which first shell N_{Au-Au} and GNC sizes.

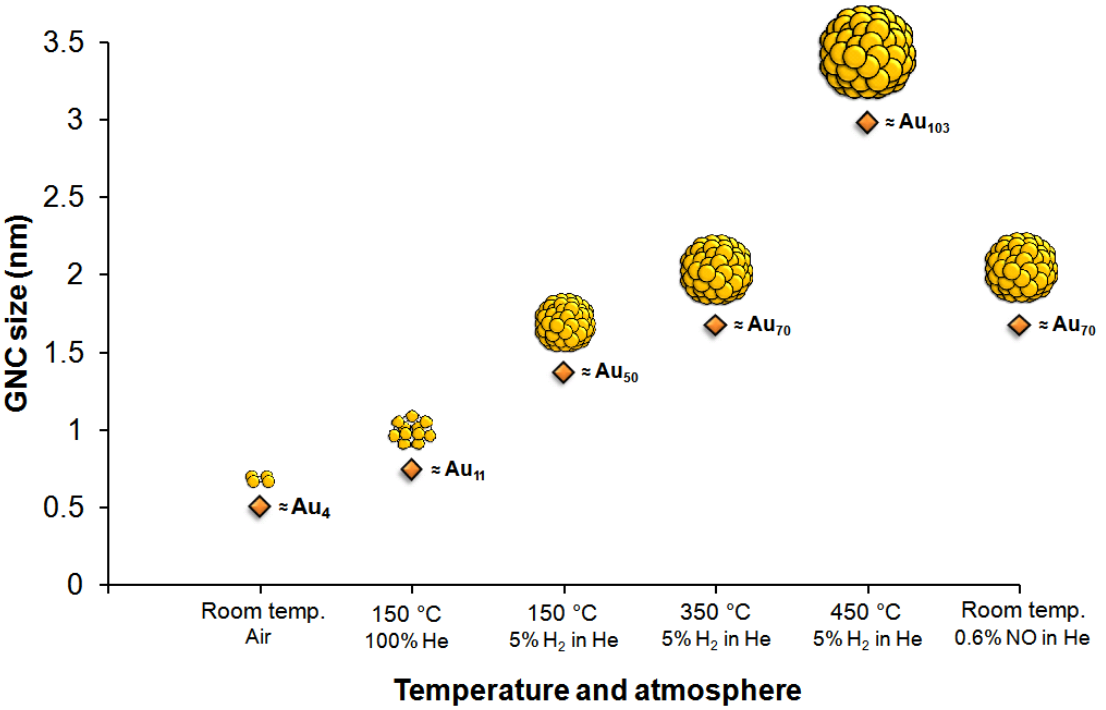

Figure 4.21: Suggested number of Au atoms per GNC and symmetries based on the obtained first N_{Au-Au} and GNC sizes for 0.07 wt% Au(III)/1:ZSM-5 throughout this in-situ study, and values reported elsewhere[3,4,5,6,35,36]

According to van Bokhoven *et al.*[4] a first shell N_{Au-Au} of 3.8 will correspond to Au_4-Au_6 nanoclusters. Since the obtained first shell N_{Au-Au} at room temperature is slightly lower (3.1), it is assumed that the GNCs consist of 2 Au atoms at this stage. As the temperature was increased and the atmosphere was changed to 5%

H_2 in He, the an agglomeration of the GNCs occurred since the forst shell N_{Au-Au} increased to 5.3. Based on Figure 2.11 in Section 2.2.4 the GNCs are assumed to exist as Au_{11} nanoclusters. At 150 °C in a hydrogen rich flow, the refined first shell N_{Au-Au} increased to 7.6. According to Okumura *et al.*[36] a first shell N_{Au-Au} equal to 7.8 correspond to Au_{55} clusters. The GNCs at this stage are therefore concidered to be a bit smaller, hence Au_{50} agglomerates is suggested. When the temperature reached 350 °C the first shell N_{Au-Au} was further increased (8.4) and according to Figure 2.11 it is assumed that the GNCs consist of $\approx$ 70 Au atoms. Au_{103} nanoclusters are proposed as the first shell N_{Au-Au} equals to 10 at 450 °C. Then Au(III)/1:ZSM-5 was cooled down in an oxidizing atmosphere, the first shell N_{Au-Au} was refined to be 8.4, i.e. the same as refined for the sample at 350 °C. Thus, the GNCs are assumed to exist as Au_{70} agglomerates.

4.6.2 In-situ studies of Au(III)/1:HY

Figure 4.22a illustrates the Au L_{III}-edge XANES spectra of 2.4 wt% Tetraamminegold(III) nitrate (Au(III)/2, bold dashed line), the Au foil (dashed line), 0.17 wt% Au(III)/1:HY at room temperature (bold solid line) and the heating process from 150 °C to 450 °C in a H_2 rich atmosphere (solid lines). The first derivatives of the normalized XANES are given in Figure 4.18c. The XANES are normalized and energy corrected as described in Section 3.7.3.

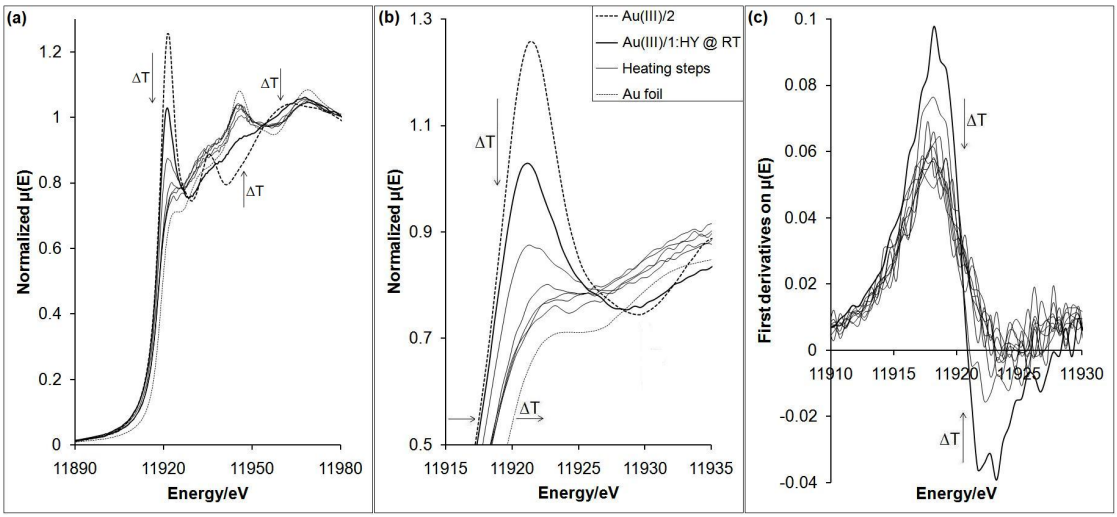

Figure 4.22: Normalized XANES and its derivatives for as-prepared 0.17 wt% AU(III)/1:HY during the in-situ experiment

The white line at ≈ 11923 eV has a higher intensity than what is detected for Au(III)/1:ZSM-5, thus indicating a more cationic character of the gold in this sample. However, the white line intensity is not as high as would be expected for trivalent gold, hence the Au^{3+} cations have been reduced to some extent during the preparation of the Au zeolytic sample. As the temperature increases the sample shows more similarity to the Au foil, indicated with a decreasing white line intensity and the appearance of shoulders similar to the Au foil located 25 eV and 50 eV above the Au L_{III}-edge. Still, it is hard to determine if the gold atoms have been fully reduced to a metallic character or not. As illustrated in Figure 4.22b and Table 4.15, the threshold energies shift towards higher energies as the oxidation state of the GNCs decreases. The trend is also reported elsewhere,[4] however, an explanation to the energy shift has not been given.

Table 4.15: Correlations in the threshold energies for Au(III)/1:HY during the in-situ measurement

Temperature (°C)	**Atmosphere**	**L_{III}-edge value** (eV)	**E_0 shift** (eV)
RT	Air	11918.70	1.0
150	100% He	11918.10	1.0
150	5% H_2 in He	11918.66	1.0
250	5% H_2 in He	11918.87	1.0
350	5% H_2 in He	11918.66	1.0
RT	0.6% NO in He	11918.21	1.0

The normalized Au L_{III} XANES spectra were fitted with the spectra of the Au foil, Au(I)Cl and Au(III)/2 using a least-square method in Athena[70] to get an indication of the gold atoms' oxidation states during the in-situ process. The results of the linear combination are given in Figure 4.23. At room temperature in air Au(III)/1:HY shows a 40% fit to the Au foil and a 60% fit to the Au(III) source, thus confirming a partial reduction of the Au^{3+} cations. When the sample is heated to 150 °C in He, the metallic character of the gold atoms seem to increase as the linear combination returns a 51 % fit to the Au foil and 16% and 33% fit to the Au(I) and Au(III) source, respectively. Changing the atmosphere to 5% H_2 in He does not affect the metallic character to any extent according to the linear combination. However, the monovalent Au contribution seems to increase at the expence of the trivalent character of the gold atoms. Based on these results it is likely to believe that some of the Au^{3+} cations, bonded to the acid sites on the zeolite, have been reduced and agglomerated into small gold nanoclusters (GNCs).

When further heated from 250 °C to 450 °C in an hydrogen rich atmosphere, the distribution of metallic, monovalent and trivalent gold seem to stabilize as the linear combination indicates a 61% fit to the Au foil and a 30% and 9% fit to the Au(I) and Au(III) source, respectively. At room temperature in a nitric oxide rich atmosphere, the linear combination returned a 69% fit to the Au foil, a 21% fit to the Au(I) source and a 10% fit to the Au(III) source. This indicates that most of the Au^{3+} cations have been reduced to Au^0 and agglomerates into small GNCs. However, it is not possible to determine the exact oxidation state of the gold atoms

based on this analysis. The numerical result are given in Appendix B.

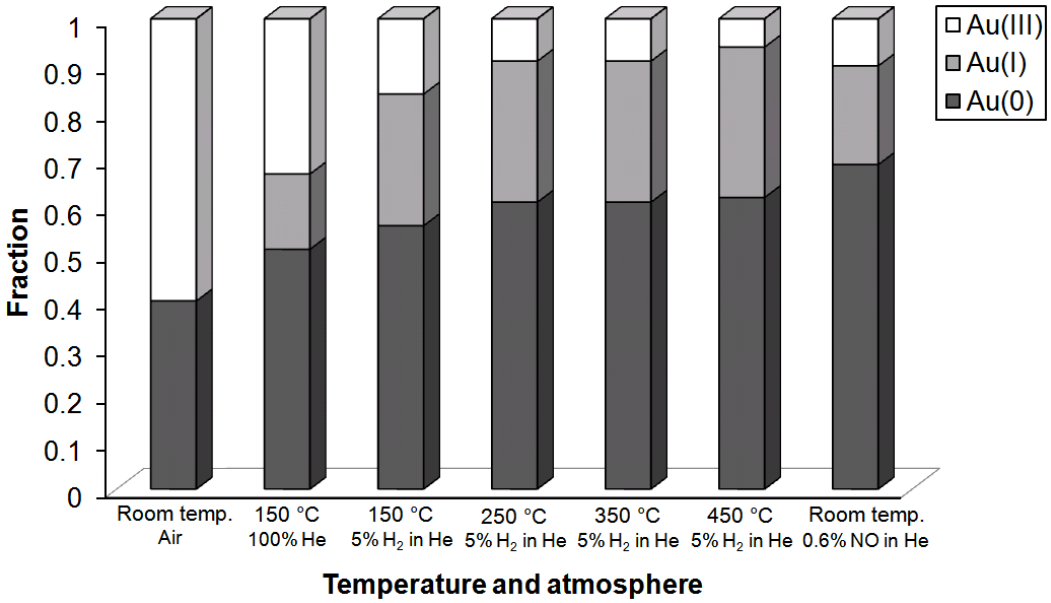

Figure 4.23: Fraction of metallic, cationic and trivalent gold present in Au(III)/1:HY at varying temperatures and atmospheres determined by linear combination

The structural parameters obtained from the EXAFS analysis is given in Table 4.16. Note that the scan carried out at 450 °C was not possible to refine due to an extremely low signal to noise ratio. As a consequence of the low signal to noise ratios, the data had to be fitted within different k-ranges. Analysis of Au(III)/1:HY at room temperature in air confirmed two neighboring shells to the Au central atom. A oxygen shell consisting of 2.5 oxygen atoms is refined to be located 2.01 Å from the core. The gold shell contains 4.4 gold atoms and the interatomic distance is refined to be 2.859 Å, i.e. shorter than what was refined for the Au foil (2.888 Å). This indicates that some of the Au^{3+} cations have been reduced, i.e. agglomerates into small GNCs. Note that the refinement was performed within k-values ranging from 1.5 to 10 $Å^{-1}$. With large central atoms, such as gold, a lot of structural information are located between 10 and 12 $Å^{-1}$. Since k-values above 10 $Å^{-1}$ was not possible to refine, some of the structural information regarding multiplicity and bonding distance might be somewhat incongruous. The size of the GNCs in the sample is found to be 0.66 nm at this stage.

Table 4.16: Parameters from the least squares EXAFS analysis for as-prepared 0.17 wt% Au(III)/1:HY prepared with 0.05 M Au(III)/1 solution used for analysis of the Au L_{III}-edge data[a]. AFAC is refined to be 1.0615 for the Au foil and 0.7363 for tetraamminegold(III)nitrate (Au(III)/2).

Temp. (°C)	**Atm.**	**Shell**	**N**	**R**[a] (Å)	**2σ^2** (Å^2)	**R**[b] (%)	**d$_c$**[b] (nm)
RT[c]	Air	Au-O	2.5(1)	2.010(4)	0.001(2)	32.58	
		Au-Au	4.4(6)	2.859(9)	0.020(2)		0.66
150[d]	100% He	Au-O	1.0(1)	2.03(3)	0.001(9)	57.86	
		Au-Au	3.0(4)	2.877(9)	0.013(2)		
150[e]	5% H_2 in He	Au-Au	6.8(5)	2.846(5)	0.017(1)	53.92	1.19
250[c]	5% H_2 in He	Au-Au	6.5(5)	2.830(5)	0.021(1)	54.98	1.10
350[f]	5% H_2 in He	Au-Au	7.9(7)	2.824(8)	0.031(2)	53.69	1.49
RT[e]	0.6% NO in He	Au-O	0.7(2)	1.86(2)	0.001(4)	47.18	
		Au-Au	8.1(6)	2.845(4)	0.0095(9)		1.50

[a] EXAFS analysis were preformed as described in Section 3.7.3
[b] Determined by modifying the calculations made by de Graaf *et al.*[39]
[c] $1.5 < k < 10.0$ Å^{-1}, $0.1 < r < 6.0$ Å
[d] $1.5 < k < 9.0$ Å^{-1}, $0.1 < r < 6.0$ Å
[e] $1.5 < k < 11.0$ Å^{-1}, $0.1 < r < 6.0$ Å
[f] $1.5 < k < 8.0$ Å^{-1}, $0.1 < r < 6.0$ Å

At 150 °C in a helium rich atmosphere, an oxygen shell was still possible to refine, hence indicating that gold cations are still present in the sample being bonded to the zeolite via the acid sites. The analysis confirms one oxygen atom 2.03 Å from the core. The gold shell consists of 3.0 gold atoms located 2.877 Å from the central atom. The decrease in N_{Au-Au} and the increase in R_{Au-Au} can be explained by the narrow k-range for the refinement. Due to a high signal to noise ratio, only k-values between 1.5 and 9 Å^{-1} were possible to refine. This has clearly influenced the refinement result as it would be expected that the N_{Au-Au} would increase when N_{Au-O} decreased. However, the structural values are within the standard deviations (given in parenthesis) of the refinement carried out at room temperature.

When the atmosphere is changed to 5% H_2 in He, the oxygen shell is no longer possible to refine, hence indicating that all the Au^{3+} cations have been reduced

and exist as small GNCs in the sample. A gold shell containing 6.8 gold atoms is detected at a bonding distance 2.846 Å from the central atom. The GNC size at this stage is found to be 1.19 nm. When heated to 250 °C in the same atmosphere, slightly lower N_{Au-Au} and R_{Au-Au} are detected for the sample. The data is refined from 1.5 to 10.0 $Å^{-1}$ which contributed to somewhat incongruous values for the mulitiplicity and the interatomic distance. The thermal vibrations, represented by the Debye-Waller factor ($2\sigma^2$), increased from 0.017 to 0.021 when the temperature was raised from 150 °C to 250 °C. This may also have influenced the result of the EXAFS analysis. Still, the obtained structural values are within the standard deviations.

As the temperature was raised to 350 °C the neighboring gold shell was refined to consist of 7.9 gold atoms located 2.824 Å from the core. Thus, the size of the GNCs have increased. The GNC diameter is found to be 1.49 nm at this temperature. When cooled down to room temperature, a neighboring oxygen shell, consisting of 0.7 oxygen atom, was possible to refine. The shell is located 1.86 Å from the central atom. Both N_{Au-Au} and R_{Au-Au} increased as the temperature was lowered in an nitric oxide rich atmosphere. The detection of an oxygen shell indicate some oxidizing capacity for the sample, although N_{Au-Au} is refined to increase. The experimental and calculated k^3 weighted Au EXAFS and its Fourier Transform for 0.17 wt% Au(III)/1:HY is given in Figure 4.24.

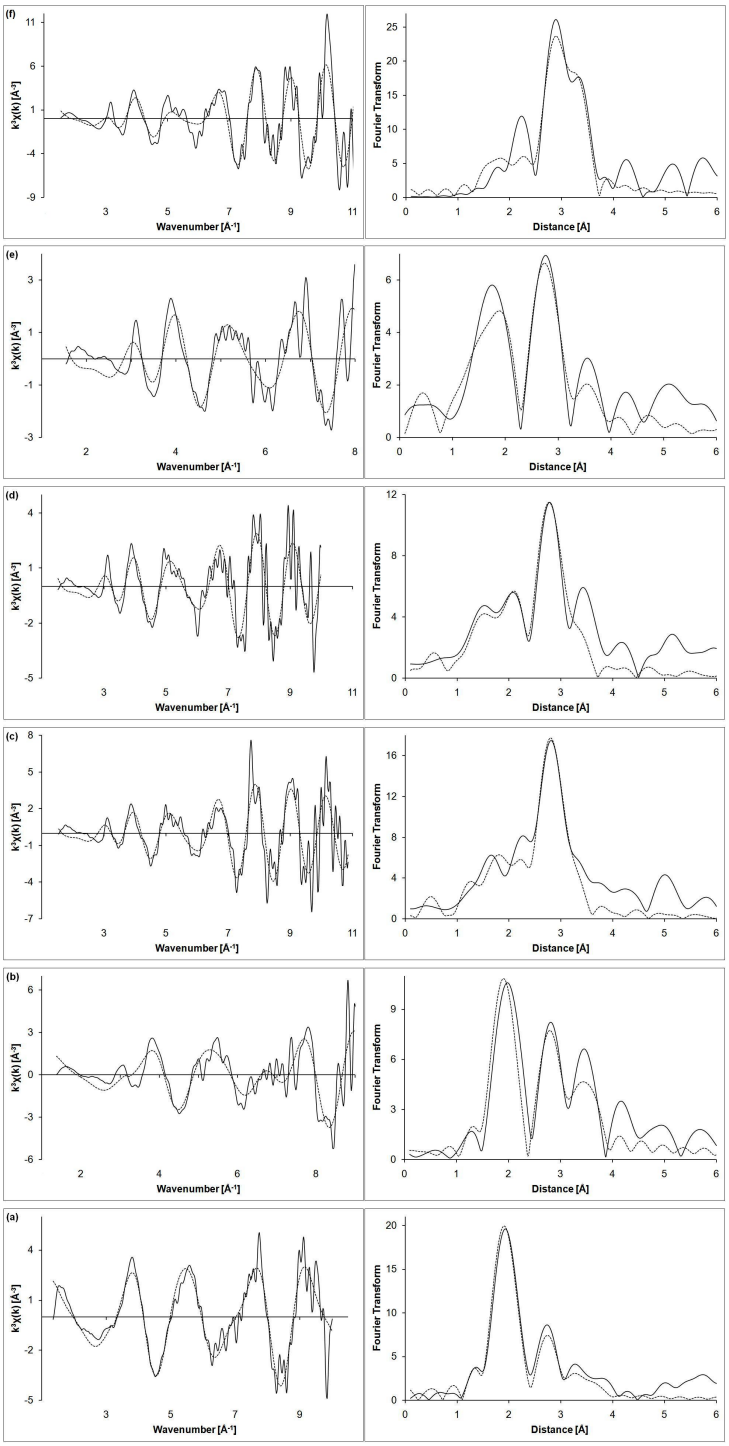

Figure 4.24: Experimental (-) and calculated ($\cdots$) k^3 weighted Au EXAFS and its Fourier Transform for 0.17 wt% Au(III)/1:HY at (a) room temperature in air; (b) 150 °C in helium; (c) 150 °C in hydrogen; (d) 250 °C in helium; (e) 350 °C in helium and (f) room temperature in nitric oxide

Suggested number of Au atoms per GNC and symmetries based on the obtained first N_{Au-Au} and GNC sizes throughout this EXAFS analysis, and values reported elsewhere[3,4,5,6,35,36] are illustrated in Figure 4.25. As mentioned in Section 4.6.1 there has not been performed any stability studies on the suggested Au_n agglomerates.

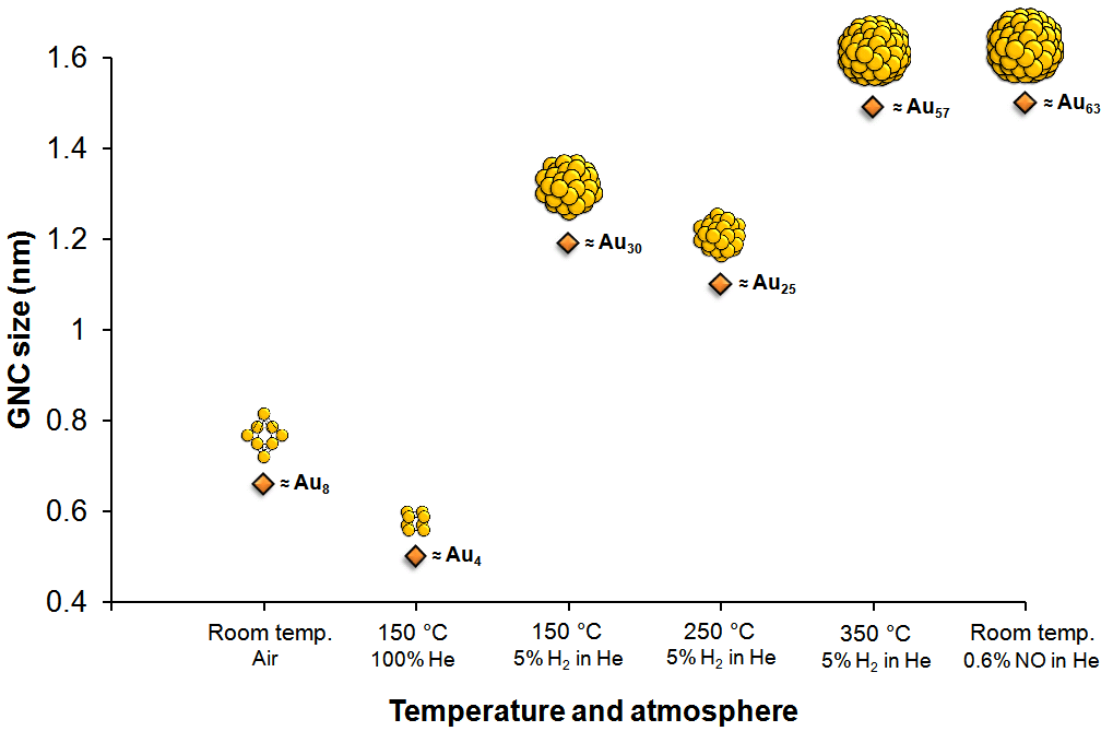

Figure 4.25: Suggested number of Au atoms per GNC and symmetries based on the refined first N_{Au-Au} and GNC sizes refined for 0.17 wt% Au(III)/1:HY, and values reported elsewhere[3,4,5,6,35,36]

The first shell N_{Au-Au} refined at room temperature correspond to Au_8 nanoclusters according to Fierro-Gonzalez *et al.*[3]. When the temperature was raised to 150 °C in a helium rich atmosphere, the first shell N_{Au-Au} was refined to decrease to 3.0. As discussed above, the refined N_{Au-Au} value is still within the standard deviation of the N_{Au-Au} refined at room temperature, hence a decrease in the GNC size has probably not occurred. Yet, a N_{Au-Au} equal to 3.0 will correspond to Au_4 nanoclusters according to van Bokhoven *et al.*[4]. When the atmosphere was changed to 5% H_2 in He, the first shell N_{Au-Au} was refined to be 6.8, hence

corresponding to GNCs consisting of ≈ 30 Au atoms, according to Figure 2.11 in Section 2.2.4. As the temperature was raised to 250 °C, the first shell N_{Au-Au} was refined to decrease from 6.8 to 6.5. Due to thermal vibration and a narrow k-range during refinement, the GNCs are not assumed to decrease. However a first shell N_{Au-Au} equal to 6.5 would correspond to ≈ Au_{25} agglomerates according to Figure 2.11. At 450 °C the refined first shell N_{Au-Au} was found to be 7.9, hence very close to the value Okumura *et al.*[36] have reported for Au_{55} nanoclusters (N_{Au-Au} = 7.8). It is therefore assumed that the GNCs exist as ≈ Au_{57} agglomerates. When the sample was cooled down to room temperature in an oxidizing atmosphere the first shell N_{Au-Au} was refined to increase to 8.1. This value is somewhere between the values repoted by Guzman *et al.*[35]and Okumura *et al.*[36]. Thus, it is assumed that the GNCs consist of ≈ 63 Au atoms at this stage.

4.6.3 In-situ studies of Au(III)/2:SAPO-34

The normalized Au L_{III}-edge XANES spectra of 2.4 wt% Tetraamminegold(III) nitrate (Au(III)/2, bold dashed line), the Au foil (dashed line), 0.06 wt% Au(III)/1:HY at room temperature (bold solid line) and the heating process from 150 °C to 450 °C in a H_2 rich atmosphere (solid lines) is shown in Figure 4.26. The first derivatives of the normalized XANES are given in Figure 4.26c. The XANES are normalized and energy corrected as described in Section 3.7.3.

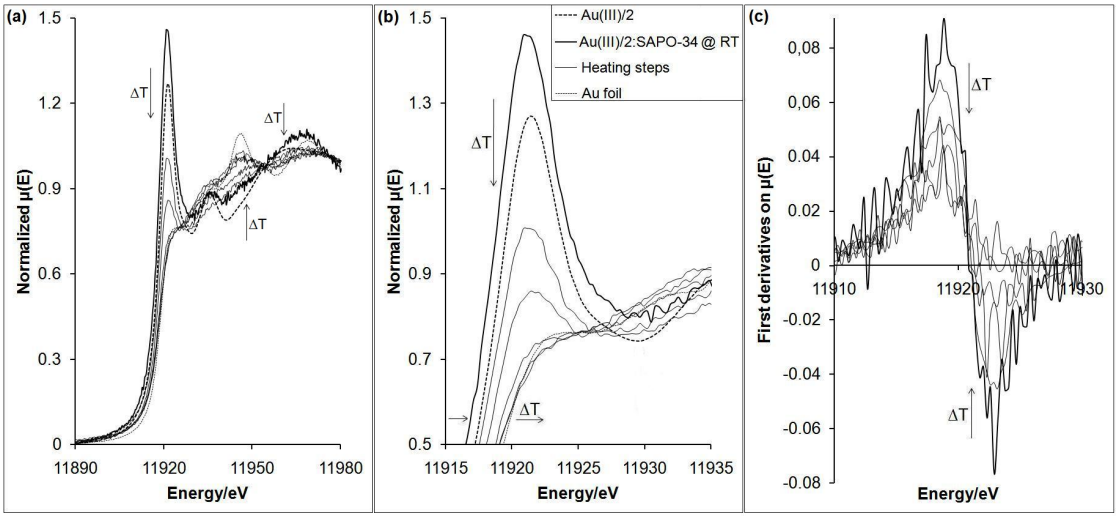

Figure 4.26: Normalized XANES and its derivatives for as-prepared 0.06 wt% AU(III)/2:SAPO-34 during the in-situ experiment

The normalized XANES spectra clearly indicates that Au(III)/2:SAPO-34 has the highest white line intensity of the three investigated samples, yielding a higher intensity than what was detected for the Au(III) source itself. This supports the assumption discussed in Section 4.5.1 regarding the incomplete trivalent character for 2.4 wt% tetraaminegold(III) nitrate (Au(III)/2). The intensity of the white line decreases as the temperature rises, yet at a slower rate than what observed for the two other investigated samples. The white line do not disappear completely before the temperature has reached 250 °C. In addition, the sample do not show resemblance with the characteristic Au foil shoulders located at 25 eV and 50 eV above the Au L_{III}-edge at lower temperatures. Based on these observations it is likely to believe that the gold in the sample has withheld its cationic character until this stage. When further heated in a hydrogen rich atmosphere the normalized XANES

Table 4.17: Correlations in the threshold energies for Au(III)/2:SAPO-34 during the in-situ measurement

Temperature (°C)	**Atmosphere**	**L_{III}-edge value** (eV)	**E_0 shift** (eV)
RT	Air	11917.57	-1.0
150	100% He	11918.26	-1.0
150	5% H_2 in He	11918.61	-1.0
250	5% H_2 in He	11918.72	-1.0
350	5% H_2 in He	11918.75	-1.0
450	5% H_2 in He	11918.89	-1.0
RT	0.6% NO in He	11918.76	-1.0

show resemblance to the Au foil, thus indicating a partial reduction of the Au^{3+} cations and an agglomeration of small gold nanoclusters (GNCs). As mentioned in the two previous in-situ studies, the threshold energies shifts towards higher energies as the oxidation state of the GNCs decreases, as shown in Figure 4.26b and Table 4.17.

The normalized Au L_{III}-edge XANES spectra of Au(III)/2:SAPO-34 at different temperatures were fitted with the XANES spectra of the Au foil, Au(I)Cl and Au(III)/2 to get an indication of the oxidation states of the gold atoms during the in-situ study. As seen in Figure 4.27 the normalized XANES carried out at room temperature in air shows a 100% fit with the Au(III) source, thus indicating that the gold is present as Au^{3+} cations, bonded to the acid sites of the zeotype. When helium was passed through the in-situ cell and the temperature was raised to 150 °C it seems like some of the Au^{3+} cations have been reduced as the linear combination returned a 61% fit to the Au(III) source. The resemblance with the Au foil and the Au(I) source was fitted to be 36% and 25%, respectively.

By changing the atmosphere to 5% H_2 in He the gold cations got further reduced. The linear combination returned a third fit to each of the reference compounds at this stage. When further heated the normalized XANES carried out at 250 °C, 350 °C and 450 °C showed low resemblance to the Au(III) source, hence indicating an additional reduction of the gold cations present in the zeotypic sample. Since

the resemblance to both the Au foil and Au(I) source is rougly equally divided, it is hard to predict the exact oxidation state of the gold atoms. However, it is clear that quite a large fraction of the Au^{3+} cations are no longer bonded to the zeotype, but present in the system as small GNCs.

As the sample was cooled down to room temperature in a nitric oxide rich atmosphere the linear contribution returned a 61% fit to the Au foil. This indicates an additional reduction of the gold cations as the temperature is let down and the atmosphere is changed. Although these results are too uncertain to conclude the final oxidation state of the gold atoms, one conclusion can be drawn from the linear combination. Au(III)/2:SAPO-34 is by far the sample who shows the highest degree of trivalent gold compared with the two other samples discussed in the previous sections. In addition, both the normalized XANES and the linear combination concludes that the reduction rate of the Au^{3+} cations is higher for the two other samples than what is shown for Au(III)/2:SAPO-34. For numerical results of the linear combination, please see Appendix B.

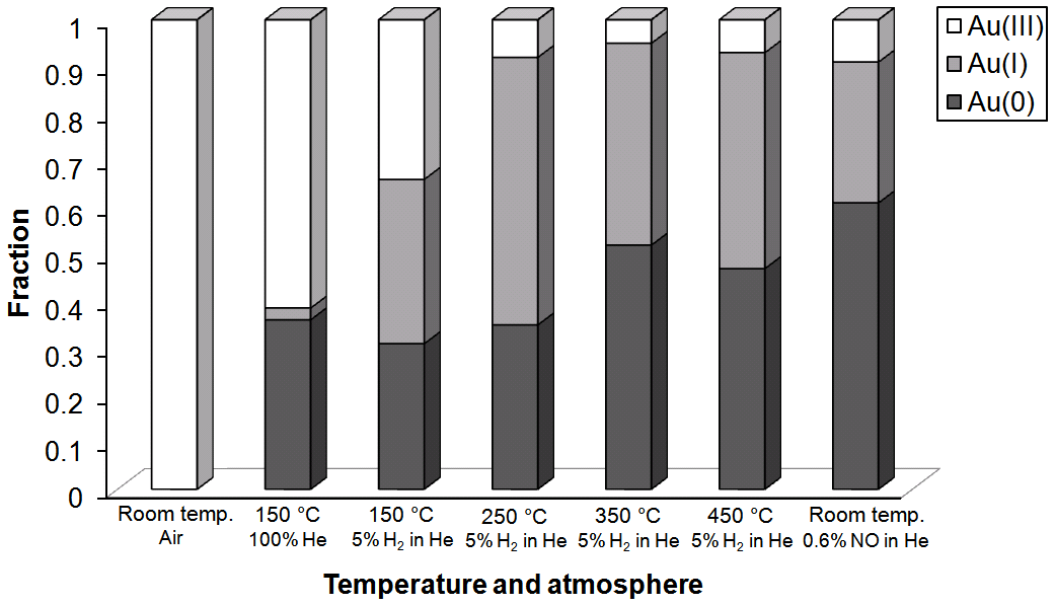

Figure 4.27: Fraction of metallic, cationic and trivalent gold present in Au(III)/2:SAPO-34 at varying temperatures and atmospheres determined by linear combination

The structural information obtained from the EXAFS analysis is given in Table 4.18. At room temperature in air only a neighboring oxygen shell, consisting of ≈ 5 oxygen atoms, was possible to detect. The oxygen shell is refined to be located 1.98 Å from the core, i.e. in accordance with values presented elsewhere[4]. The observation demonstrates that gold is present in the sample as cations bonded to the acid sites of the zeotype.[3]. The abcense of a Au-Au shell indicates an atmoic dispersion of the Au^{3+} cations on the zeotypic surface.

Table 4.18: Parameters from the least squares EXAFS analysis for as-prepared 0.06 wt% Au(III)/2:SAPO-34 prepared with 0.1 M Au(III)/2 solution used for analysis of the Au L_{III}-edge data[a]. AFAC is refined to be 1.0904 for the Au foil and 0.7363 for tetraamminegold(III)nitrate (Au(III)/2).

Temp. (°C)	**Atm.**	**Shell**	**N**	**R** (Å)	$\mathbf{2\sigma^2}$ (Å²)	**R**[a] (%)	$\mathbf{d_c}$[b] (nm)
RT[c]	Air	Au-O	4.9(4)	1.981(7)	0.008(2)	50.46	
150[c]	100% He	Au-O	4.1(4)	1.97(1)	0.019(3)	52.57	
150[c]	5% H_2	Au-O	2.1(3)	1.95(2)	0.030(6)	70.74	
	in He	Au-Au	1.3(7)	2.81(3)	0.020(7)		
250[c]	5% H_2	Au-O	0.28(8)	1.93(2)	0.001(5)	72.20	
	in He	Au-Au	3.9(6)	2.79(4)	0.027(3)		0.60
350[c]	5% H_2	Au-O	0.3(1)	1.98(2)	0.001(5)	72.84	
	in He	Au-Au	4.4(7)	2.80(1)	0.044(5)		0.66
450[d]	5% H_2	Au-O	0.9(3)	2.00(4)	0.05(2)	73.48	
	in He	Au-Au	6.0(9)	2.80(1)	0.044(5)		1.01
RT[c]	0.6% NO	Au-O	1.3(7)	1.98(8)	0.06(4)	60.97	
	in He	Au-Au	3.3(3)	2.823(5)	0.006(1)		

[a] EXAFS analysis were preformed as described in Section 3.7.3
[b] Determined by modifying the calculations made by de Graaf *et al.*[39]
[c] $1.5 < k < 11.0$ Å^{-1}, $0.1 < r < 6.0$ Å
[d] $1.5 < k < 9.0$ Å^{-1}, $0.1 < r < 6.0$ Å

At 150 °C in a helium flow, the lack of a Au-Au contribution maintained. This indicates that the gold cations most likely have a trivalent character. The neighboring oxygen shell was refined to contain ≈ 4 oxygen atoms located 1.97 Å from the core. When the atmosphere is changed to 5% H_2 in He, a neighboring gold shell was possible to be refined in addition to an oxygen shell. The multiplicity of the oxygen shell decreased from ≈ 4 to ≈ 2 when the atmosphere was changed. The interatomic distance decreased by 0.02 Å. The first Au-Au shell was located

2.81 Å from the core and contained 1.3 gold atoms. The detection of both a Au-O and an Au-Au shell indicates a partial reduction of the Au^{3+} cations. Although, due to the low value of N_{Au-Au} it is hard to determine wether the reduced Au atoms have agglomerates into small GNCs or not. According to Fierro-Gonzalenz *et al.*[3] metallic gold atoms start to aggolemate when N_{Au-Au} is found to be 2.7. It is therefore assumed that the metallic gold in the sample is still present as GNPs.

When the temperature was raised to 250 °C N_{Au-Au} was refined to be 3.9, hence a agglomeration of GNPs into small GNCs have occourred. The first Au-Au shell is refined to be located 2.79 Å from the core, while the oxygen shell, containing 28% of an oxygen atom, has a interatomic distance of 1.93 Å. The GNC size is found to be 0.60 nm at this stage.

At 350 °C the multiplicity of the oxygen shell did not change to any extent (increased from 0.28 to 0.3). However, the bonding distance to the core increased with 0.05 Å. The first Au-Au shell is refined to contain 4.4 gold atoms, hence an increase in N_{Au-Au}. The interatomic distance increased with 0.01 Å as a result of the increasing multiplicity. The Debye Waller factor ($2\sigma^2$) was high at this stage (0.044). This is probably due to the thermal vibration experienced by the zeotypic framework. The GNC size was found to be 0.66 nm, hence more of the Au^{3+} cations have been reduced and agglomerated into GNCs. The size of the GNCs are assumed to be low due to the low value of the refined N_{Au-Au}.

When the temperature reached 450 °C both N_{Au-O} and N_{Au-Au} increased, thus an additional reduction of the Au^{3+} cations and an increase in the GNC sizes. The interatomic distances, R_{Au-O} and R_{Au-Au}, were refined to be 2.00 Å and 2.80 Å, respectively. Based on the first shell N_{Au-Au} the GNC agglomerates was largest at 450 °C, yielding a diameter of 1.01 nm. When the sample was cooled down to room temperature in a nitric oxide rich atmosphere, the refinement concluded an increase in N_{Au-O} with decreasing R_{Au-O}, and a decrease in N_{Au-Au} with increasing R_{Au-Au}. It is therefore assumed that some of the small GNCs have been oxidized, thus gold cations have formed bonds with the acid sites on the zeotype. The experimental and calculated k^3 weighted Au EXAFS and its

Fourier Transform for 0.06 wt% Au(III)/2:SAPO-34 are illustrated in Figure 4.28 and Figure 4.29.

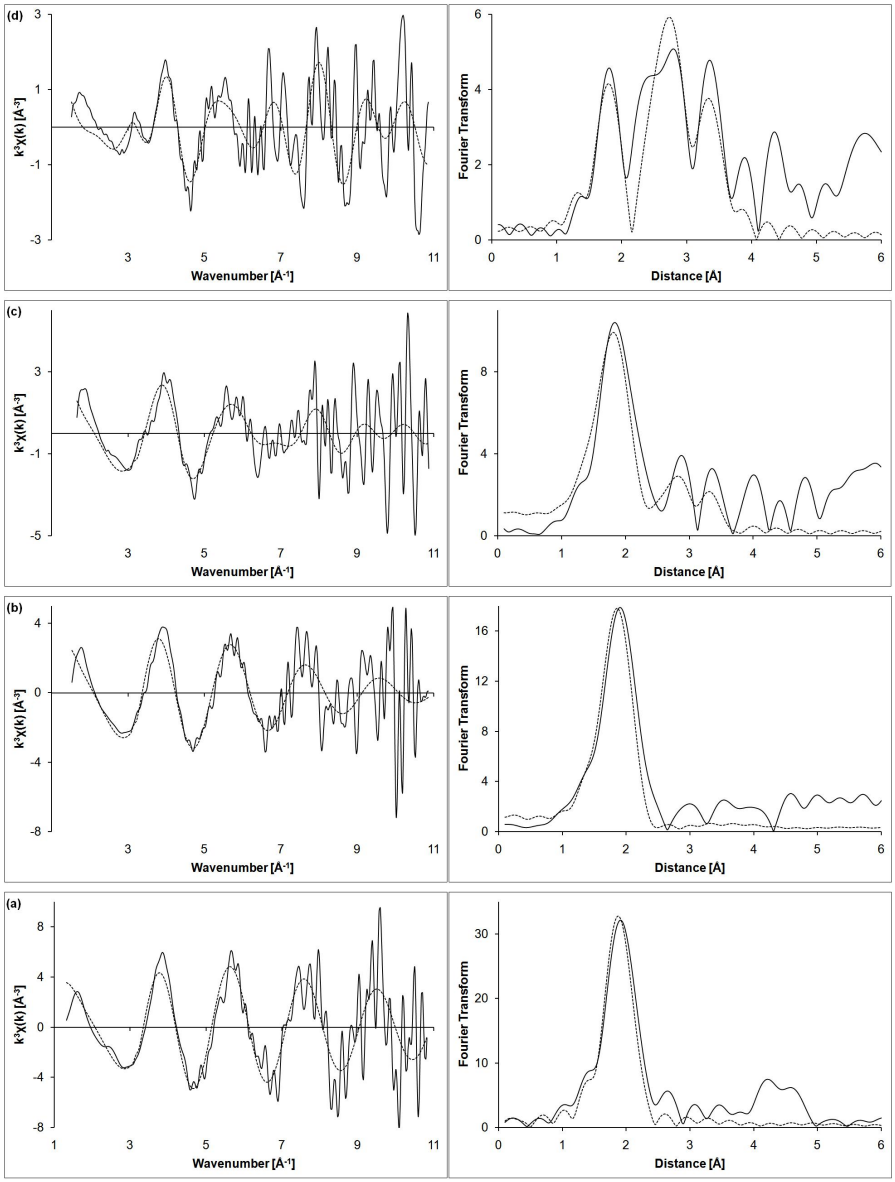

Figure 4.28: Experimental (-) and calculated ($\cdots$) k^3 weighted Au EXAFS and its Fourier Transform for 0.06 wt% Au(III)/2:SAPO-34 at (a) room temperature in air; (b) 150 °C in He; (c) 150 °C in 5% H_2 in He and (d) 250 °C in 5% H_2 in He

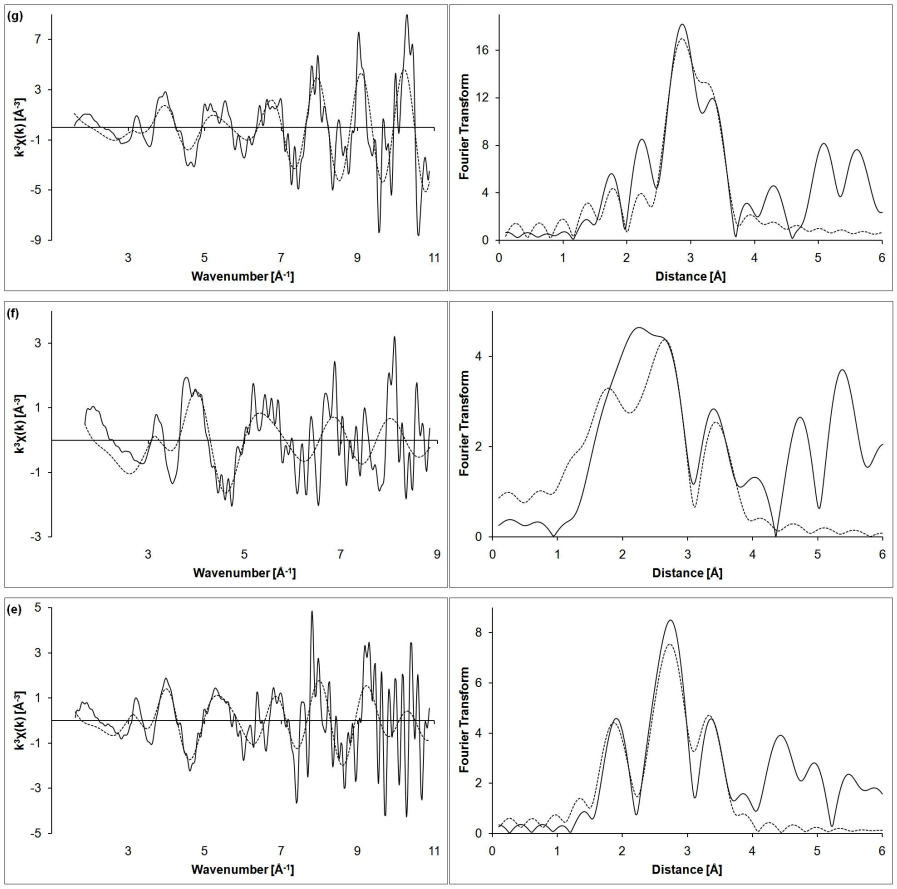

Figure 4.29: Experimental (-) and calculated ($\cdots$) k^3 weighted Au EXAFS and its Fourier Transform for 0.06 wt% Au(III)/2:SAPO-34 at (e) 350 °C in 5% H_2 in He; (f) 450 °C in 5% H_2 in He and (g) room temperature in 0.6% NO in He

The Suggested number of Au atoms per GNC and symmetries based on the first N_{Au-Au} and GNC sizes obtained during this EXAFS analysis, and values reported elsewhere[3,4,5,6,35,36]. Figure 4.30.

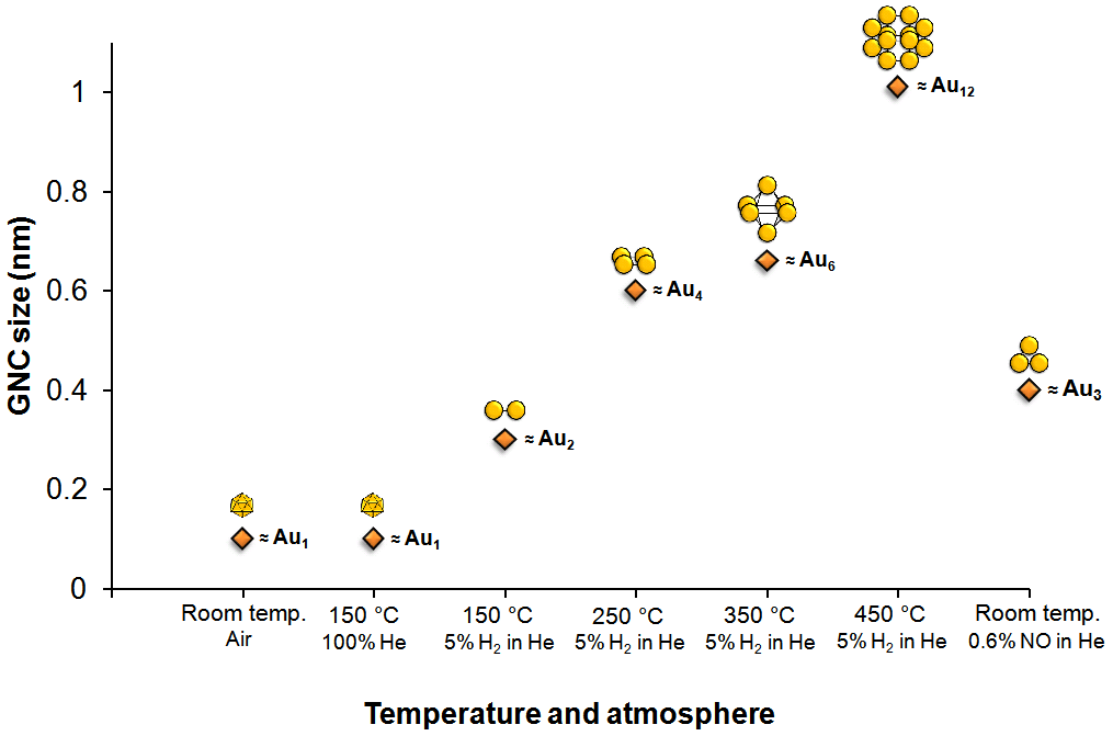

Figure 4.30: Suggested number of Au atoms per GNC and symmetries based on own first N_{Au-Au} and GNC sizes and values reported elsewhere[3,4,5,6,35,36]

A first shell N_{Au-Au} was not found for Au(III)/2:SAPO-34 at room temperature nor at 150 °C in He. This is evidently indicates that gold is present in the system as trivalent gold cations. When the atmosphere was changed to 5% H_2 in He, a small agglomeration of the GNPs occurred, giving rise to the formation of small Au_2 nanoclusters.[35] The first shell N_{Au-Au} for the sample at 250 °C and 350 °C were refined to be 3.9 and 4.4, respectively. According to van Bokhoven *et al.*[4] first shell N_{Au-Au} values in this range correspond to Au_4-Au_6 nanoclusters. It is therefore assumed that the GNCs at 250 °C consists of 4 Au atoms while an increase in the temperature led to an agglomeartion of the GNCs, thus a formation of Au_6 nanoclusters at 350 °C. When further heated the first shell N_{Au-Au} was

found to be 6.0 at 450 °C. According to Figure 2.11 presented in Section 2.2.4 the GNCs exists as $\approx Au_{12}$ nanoclusters at this temperature. When cooled down in an oxidizing atmosphere, the first shell N_{Au-Au} decreased, i.e. a reduction of the GNCs occurred. It is assumed that the GNCs at this stage consist of 3 Au atoms.[4]

During the in-situ experiment a mass spectrometer was connected to the exhaust gas to detect variations in the exhaust gas components as the atmosphere was changed from reducing (5% H_2 in He) to oxidizing (0.6% NO in He). The variation in the concentrations of the exhaust gas compounds is illustrated in Figure 4.31.

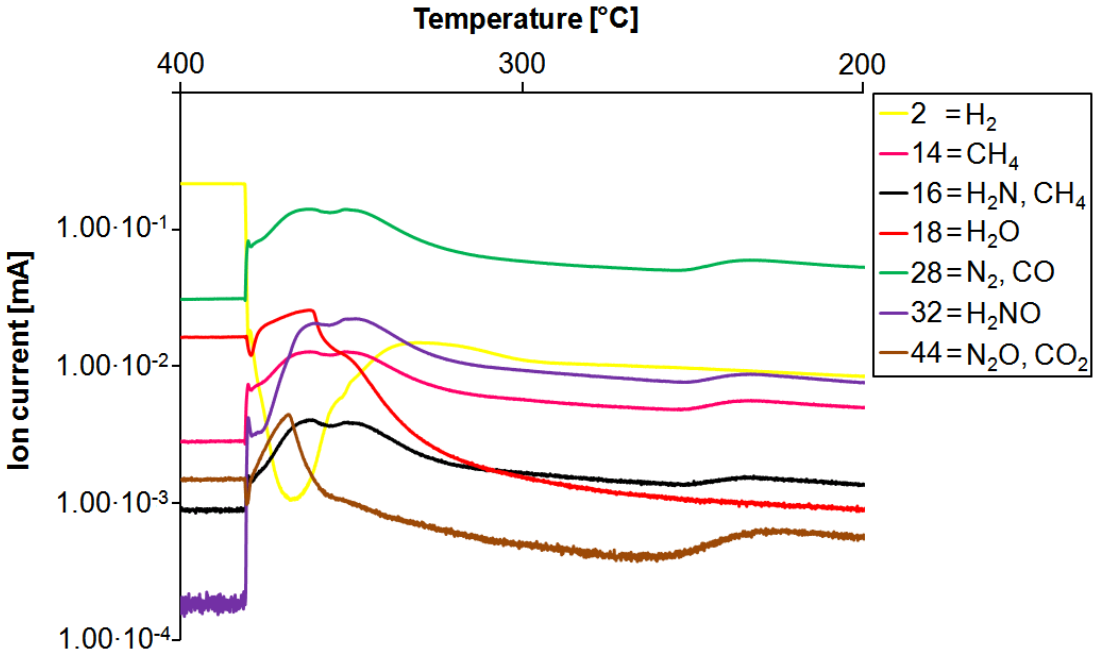

Figure 4.31: Mass spectroscopy of 0.06 wt% Au(III)/2:SAPO-34 in an oxidizing atmosphere

As seen in the figure, the exhaust gas concentration of what is believed to be nitrous compounds increased as the oxidizing flow is passed trough the in-situ cell. The gas concentration increased at $\approx$ 360 °C for the molecular weight 16 g/mole (corresponding to H_2N). This indicates that NO, having a oxidation state of +II, has been reduced since nitrogen in H_2N has the oxidation state -I. A increase in the exchast gas concentration is also observed for the molecular weight 28 g/mole (corresponding to N_2), thus indicating a reduction of nitrogen from oxidation state

+II to 0. The same reduction is observed for the compound corresponding to a molecular weight of 32 g/mole as this compound is belived to be H_2NO. A quite narrow and intense increase in the exhaust gas concentration is observed at ≈ 370 °C for the molecular mass 44 g/mole. Assuming that this compound is N_2O, a reduction of nitrogen from oxidation state +II to +I has occurred. In addition of the nitrous compounds mentioned above, compounds such as water (molecular weight equal to 18 g/mole) and methane (molecular weight equal to 14 g/mole) are also believed to evaporate from the sample.

The exact amount of NO reduced is impossible to predict based on these observation since the variations in the exhaust gas concentration is given in ion current (mA). However, the observations clearly indicates that Au(III)/2:SAPO-34 was able to reduce NO, hence making it a interessting catalyst with respect to selective catalytic reduction (SCR) of NO and SCR of NO_x.

4.6.4 A summary of the in-situ studies

The in-situ studies of 0.07 wt% Au(III)/1:ZSM-5, 0.17 wt% Au(III)/1:HY and 0.06 wt% Au(III)/2:SAPO-34 revealed great differences between the samples. In the XANES region the intensity of the white lines clearly separate the samples from each other. The intensity of the white lines is used as a indicator for the presence of trivalent gold cations in the samples, as a high white line intensity represents the degree of unoccupied $5d$ orbitals, i.e. $5d^7$ having a higher white line intensity than $5d^8$, and so on. At room temperature Au(III)/2:SAPO-34 had the highest intensity of the white line, followed by Au(III)/1:HY. Au(III)/1:ZSM-5 showed only a small white line at room temperature, hence indicating that a larger fraction of the Au^{3+} cations in this sample have been reduced, compared to the two the samples.

When the samples were heated to 150 °C in 100% He it was no longer possible to detect a white line for Au(III)/1:ZSM-5. The white line intensities of both Au(III)/1:HY and Au(III)/2:SAPO-34 also decreased as illustrated in Figure 4.32. Yet, the white line intensity of Au(III)/1:SAPO-34 was evidently more intense than Au(III)/1:HY's white line. The absence of a white line for Au(III)/1:ZSM-5 indicated that all the trivalent gold cations in the sample have been reduced to metallic gold. Gold cations are still believed to the present in the two other samples. However, due to the decrease in the white line intensities, a fraction of the Au^{3+} cations have been reduced. Since the white line of Au(III)/2:SAPO-34 has a higher intensity than what shown for Au(III)/1:HY, the fraction of metallic gold atoms is concidered to be larger in the latter sample.

As the atmosphere was changed to 5% H_2 in He, only a small white line for Au(III)/2:SAPO-34 was possible to detect. The observation indicated that all the Au^{3+} cations have been reduced to metallic gold atoms in the two other samples. Since the intensity of Au(III)/2:SAPO-34's white line was very small, only a small fraction of the gold cations are still bonded to the zeotype. The majority of the gold atoms are therefore assumed to be present in the samples as metallic gold atoms. When the temperature was further raised it was not possible to decet a

white line for neither of the samples. Results from the peak fitting procedure is listed in Table 4.19.

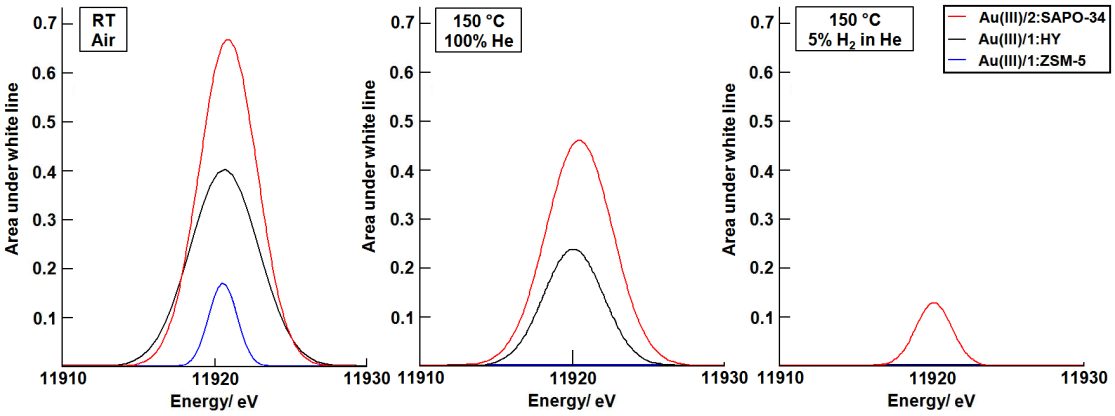

Figure 4.32: Area under white line for 0.07 wt% Au(III)/1:ZSM-5 (blue), 0.17 wt% Au(III)/1:HY (black) and 0.06 wt% Au(III)/2:SAPO-34 (red)

Table 4.19: Peak fitting of area under the white lines for 0.07 wt% Au(III)/1:ZSM-5, 0.17 wt% Au(III)/1:HY and 0.06 wt% Au(III)/2:SAPO-34 possible to detect throughout the in-situ experiments

Sample	Temp./Atm.	Centroid	Func.	Amp.	Width	R-factor (10^{-4})
Au(III)/1:ZSM-5	RT/Air	11921.1(3)	Gauss	0.87(9)	1.8(1)	6.2
Au(III)/1:HY	RT/Air	11920.6(3)	Gauss	2.3(1)	2.24(7)	7.3
Au(III)/2:SAPO-34	Rt/Air	11920.9(1)	Gauss	3.3(1)	2.10(7)	10.5
Au(III)/1:ZSM-5	150 °C/He	0	Gauss	0	0	-
Au(III)/1:HY	150 °C/He	11920.1(6)	Gauss	1.3(1)	2.4(1)	6.7
Au(III)/2:SAPO-34	150 °C/He	11920.4(2)	Gauss	2.62(9)	2.41(5)	10.6
Au(III)/1:ZSM-5	150 °C/5% H_2 in He	0	Gauss	0	0	-
Au(III)/1:HY	150 °C/5% H_2 in He	0	Gauss	0	0	-
Au(III)/2:SAPO-34	150 °C/5% H_2 in He	11920(1)	Gauss	0.37(7)	1.20(2)	18.9

The EXAFS analyses revealed great variations in the first shell N_{Au-Au} during the in-situ studies of the three samples. The refined first shell N_{Au-Au} values are shown in Figure 4.33. The refined first shell N_{Au-Au}s for both Au(III)/1:ZSM-5 and Au(III)/1:HY are higher than what refined for Au(III)/2:SAPO-34. Thus, the fraction of metallic gold atoms, compared to the fraction of Au^{3+} cations,

are assumed to be larger for these samples compared to Au(III)/2:SAPO-34. A possible explanation to these observations may be explained by the three different microporous structures the samples possess.

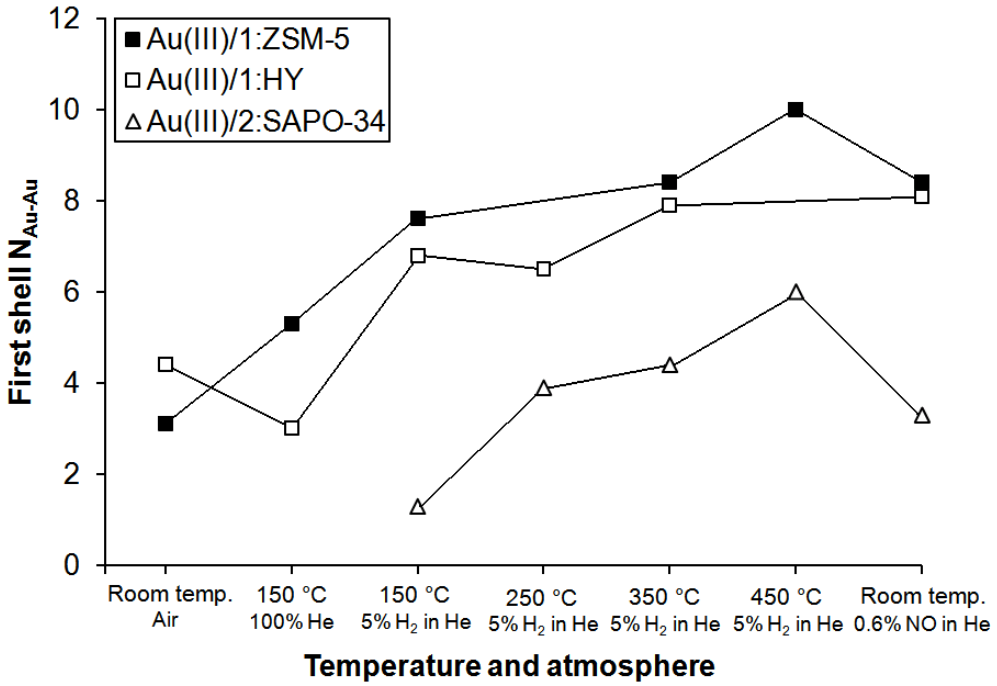

Figure 4.33: Variation in first shell N_{Au-Au} during the in-situ studies of 0.07 wt% Au(III)/1:ZSM-5, 0.17 wt% Au(III)/1:HY and 0.06 wt% Au(III)/2:SAPO-34

ZSM-5 is constructed by two types of intersecting channels consisting of pores that are approximately 0.55 nm in diameter. The linear combination (see Section 4.6.1) revealed a 50% resemblance between the gold in the sample and the Au foil at room temperature, thus inducating a partial reduction of the Au^{3+} cations. According to the EXAFS analysis the Au^{3+} cations were partially reduced at room temperature as it was possible to refine an Au-Au shell, in addition to a Au-O shell. The reduced gold atoms are assumed have agglomerated into small metallic gold nanoclusters (GNCs), each cluster found to consist of 4 Au atoms, as shown in Figure 4.21 in Section 4.6.1. The size of these metallic GNCs were found to be smaller than the pore diameter of ZSM-5 ($<$ 0.55 nm), hence it is possible that the GNCs are located inside the pore structure, as well as on the external surface

of the zeolite.

The refined value of R_{Au-O} at room temperature was found to be similar to values reported for other Au-oxygen support distances elsewhere.[4] Thus demonstrating that the fraction of gold still present as gold cations are chemisorbed to the acid sites on ZSM-5 surface.[3]

The small amount of small GNCs trapped inside the pores are assumed to be expelled from the linear pores when the GNC size is closely similar to the size of the pore diameters (≈ 0.55 nm). Based on the obtained GNCs sizes, this occurred when the temperature reached 150 °C in a helium flow. The process is illustrated in Figure 4.34. The absence of Au-O shells at higher temperatures showed a reduction of all gold cations in the sample. The increase in N_{Au-Au} throughout the experiments indicated that the metallic GNCs increases in size as the temperature is raised. During oxidizing conditions a fraction of the small GNCs was partially oxidized, thus bonds between the gold cations and some of the acid sites on the zeolite were formed.

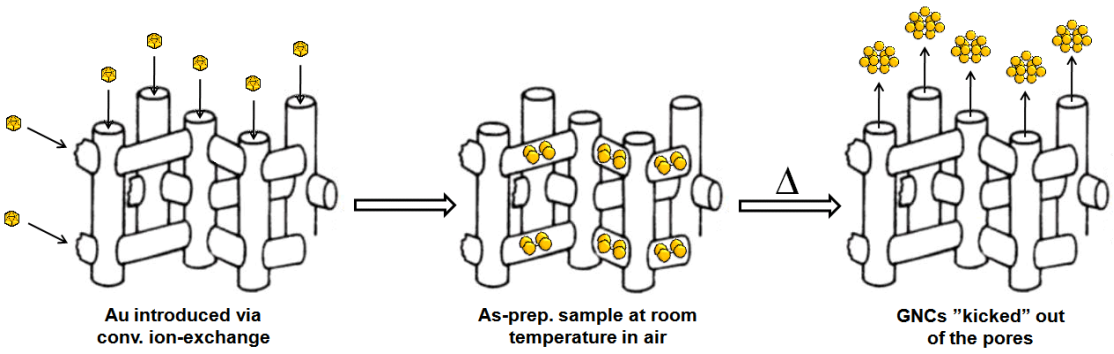

Figure 4.34: Suggested route for the introduction of Au into the pores of ZSM-5

The zeolite HY (FAU structure) consists of two types of large cages; the supercage having a diameter of 1.2 nm and the sodalite cages with diameters of 0.8 nm. EXAFS analysis carried out at room temperature showed a partial reduction of the Au^{3+} cations as both a Au-O and an Au-Au shell was detected. The reduced gold atoms are assumed to have agglomerated into GNCs, the size of these clusters

being smaller than the zeolite pores (0.66 nm). The GNCs can therefore be located both on the internal and external surface of the zeolite. The refined R_{Au-O} for the sample was refined to be similar to values reported elsewere,[3] hence confirming that the fraction of gold cations, still present in the sample, are bonded to the oxygen atoms on the zeolite surface.

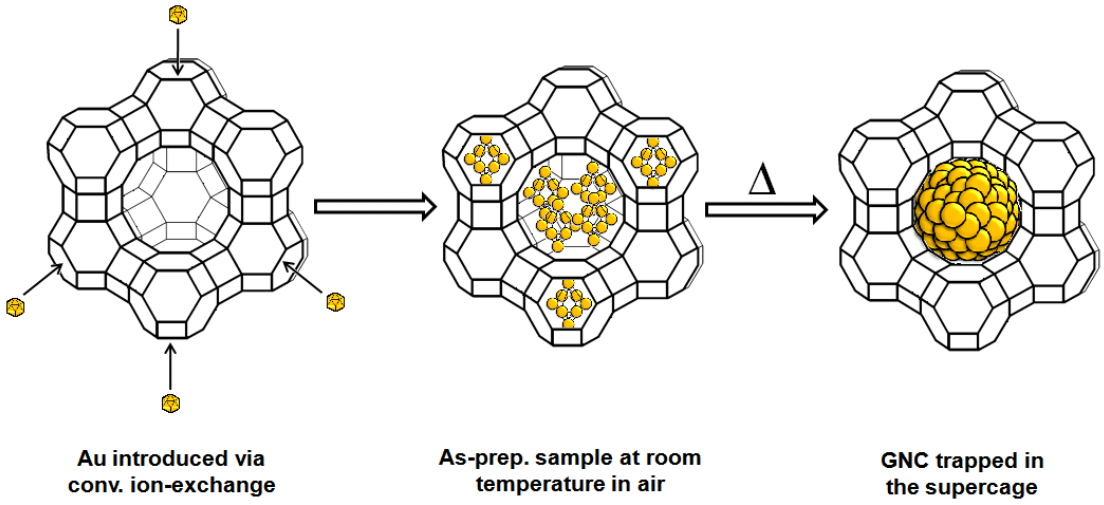

Figure 4.35: Suggested route for the introdution of Au into the pores of HY

At 150 °C in a helium flow a Au-O shell was still possible to detect, in addition to a Au-Au shell, thus indicating that a small fraction of the gold still exist as gold cations, bonded to the acid sites of the zeolite. When the atmosphere was changed to 5% H_2 in helium, the absence of a Au-O shell revealed a reduction of the gold cations into metallic gold atoms. These gold atoms are believed to have agglomerated into small GNCs with a diameter found to be 1.19 nm. Since the size of the GNCs are found to be smaller or equal to the diameter of the super cage, a portion of the GNCs may very well be located within this cage. As the temparature increased, the refined N_{Au-Au} values increased, thus indicating an agglomeration of the metallic GNCs. The refined first shell N_{Au-Au} values are therefore considered to be an average of the size distribution between GNCs located within the supercages ($<$ 1.2 nm) and the GNCs located on the external surface of the zeolite. An agglomeration of the latter ones can have lead to blockage of the pores, hence prevented the reaction gas from reaching the GNCs trapped in the supercages. The process is illustrated in Figure 4.35.

When an oxidizing flow was passed through the in-situ cell a Au-O shell was again possible to detect, thus indicating a partial oxidation of the small GNCs. This indicated that the sample possess a oxidizing character.

As seen in Figure 4.33 the EXAFS analyses show much lower values of the first shell N_{Au-Au} for Au(III)/2:SAPO-34 than what refined for the two other samples. The zeotype SAPO-34 (CHA structure) has pore diameters of 0.38 nm and an inner cage with a volume of 0.67 nm × 0.67 nm × 1 nm. Since no Au-Au shell were detected at room temperature and at 150 °C in a helium flow, all the gold cations are assumed to be atomically dispersed on the zeotype inner surface. As the atmosphere was changed from inert to reducing (hydrogen flow), a Au-Au shell was possible to detect, hence indicating a partial reduction of the gold cations. Whether the metallic atoms have agglomerated into gold nanoclusters (GNCs) or not is hard to determine due to the low value of N_{Au-Au}. According to Fierro-Gonzalez *et al.*[3] gold atoms tend to agglomerate when the first shell N_{Au-Au} is found to be ≈ 2, i.e. higher than the detected value of N_{Au-Au} at 150 °C in a helium flow.

When a reducing atmosphere was passed through the in-situ cell, more of the trivalent gold cations were reduced, indicated by a decrease in N_{Au-O} and an increase in N_{Au-Au}. The reduced portion of the gold atoms have most likely agglomerated into small gold nanoclusters (GNCs) with a diameter found to be 0.66 nm. Thus, the GNCs are smaller than the size of the pore diameter which allows them to be located both within the inner cage and on the external surface of the zeotype. When further heated in a reducting atmosphere, a larger fraction of the cationic gold was reduced, indicated with decreasing N_{Au-Au} values. However, a Au-O shell was detected throughout the experiment, thus confirming that the gold atoms are present in the sample as a mix between metallic gold and cationic gold. The metallic gold atoms are assumed to be present as small GNCs.

An explanation for why this zeotype show the formation of smaller GNCs than what detected for the two other Au samples explained by the volume of the inner

cage. When the diameter of the GNCs was found to be similar to the pore diameter (0.38 nm) it is likely that some of the GNCs were expelled through the pores and to the external surface of the zeolite. A fraction of the GNCs may have remained inside the 3 dimensional framework. As the temperature increased the GNCs within the inner cage of the zeotype will have agglomerated, i.e. been trapped inside the cage. The GNCs are therefore believed to be located both inside this cage and on the external surface of the zeotype. Thus, the detected N_{Au-Au} values will be an average of the metallic GNCs trapped in the inner cage, the somewhat larger metallic GNCs located on the external surface, in addition to the gold cations bonded to the acid sites of the zeotype. An illustration of the process is given in Figure 4.36.

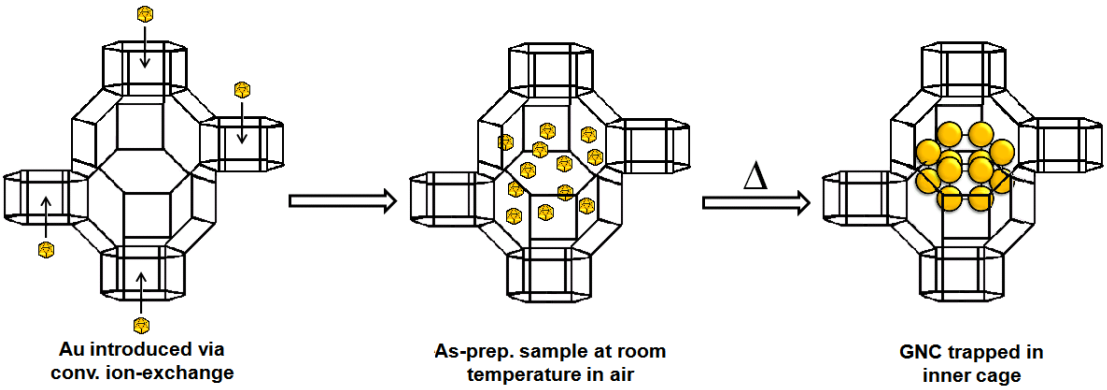

Figure 4.36: Suggested route for the introdution of Au into the pores of SAPO-34

In an oxidizing atmosphere the N_{Au-Au} value decreased, thus indicating a partial oxidation of the metallic GNCs. As discussed in Section 4.6.3 the mass spectrometer, connected to the outlet of the in-situ cell during experiment, revealed that the sample had reducing capacity with respect to NO. The exhaust gas concentration increased for nitrous compounds then a 0.6% NO in He flow was passed through the in-situ cell. An increase in gas concentration for molar masses equal to what for N_2O and N_2 clearly indicates a reduction of the nitrogen oxidation state from +II to +I and 0, respectively.

The detection of gold cations bonded to the acid sites of the zeotype throughout the enitre experiment clearly separates Au(III)/2:SAPO-34 from the two other samples. SAPO-34 was the only support of the three investigated who made it possible to obtain a homogeneous distribution of gold cations on the surface. Also, the metallic gold nanoclusters, formed by the reduced gold atoms, were found to be smaller than what detected for Au(III)/1:ZSM-5 and Au(III)/1:HY. Of the three structures, the three dimensional CHA structure has shown itself to be the optimal structure for size control of the metallic GNCs. In addition, mass spectroscopy revealed oxidizing properties for the sample as it was found to reduce NO to N_2O and N_2. This clearly makes the sample interesting with respect to selective catalytic reduction of NO_x.

4.7 Activity measurements for CO oxidation and PROX

Carbon monoxide oxidation and PROX measurements were performed as described in Section 3.8. Pre-treatment at 150 °C for 2 hours in an H_2/N_2 flow prior to the activation measurements did not activate the GNCs in neither Au(III)/2:HY nor Au(III)/2:SAPO-34, thus resulting in on conversion of CO to CO_2. Due to no conversion, Au(III)/2:HY was pre-treated at 300 °C for 2 hours prior to the reaction to test if a increase of the pre-treatment temperature would activate the sample. No conversion was measured when the CO oxidation conditions ($N_2/O_2/CO$) was applied. When H_2 was added to the gas mixture (PROX conditions), a small conversion was measured. The result is given in Figure 4.37.

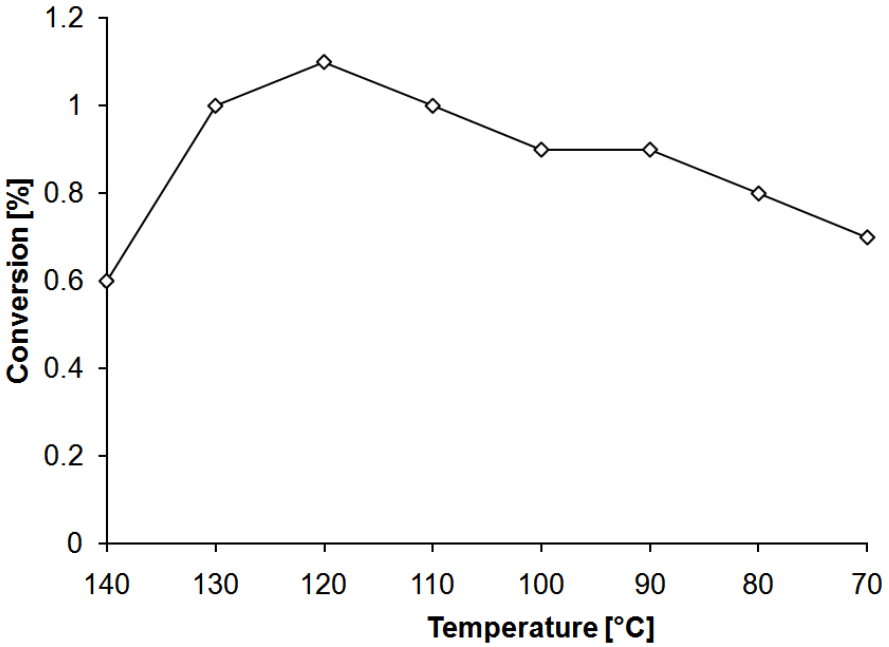

Figure 4.37: Conversion of CO to CO_2 (in %) at PROX conditions for 0.09 wt% Au(III)/2:HY

With such a small conversion it is reasonable to conclude that Au(III)/2:HY did not work as a catalyst for CO oxidation even at a higher pre-treatment temperature. There are several reasons why neither Au(III)/2:SAPO-34 nor Au(III)/2:HY did not convert carbon monoxide to carbon dioxide, some of them are discussed under.

The first obvoius reason for the low conversion is the low gold content in the samples. As mentioned in Section 4.1 ICP-MS measurements detected a gold content of 0.09 wt% for Au(III)/2:HY and 0.06 wt% for Au(III)/2:SAPO-34. Okumura *et al.*[36] reported of conversion with 5 wt% Au loaded on the zeolite HY, while other have reported of CO conversion with Au catalysts containing 1-3 wt%.[3,78,81] Although the in-situ studies revieled that conventional ion-exchange, using the Au(III)/2 complex as the precursor, led to formation of small GNCs in the size range reported as desirable with respect to CO oxidation, it seems that the amount of Au present in the samples are to small to acitvate the CO oxidation process.

The choice of zeolites or zeotypes as supports for Au catalysts for CO oxidation is highly debated among scientists. Normally a neutral metal oxide support would be desired, some of the most studied Au catalyst supports being Fe_2O_3, Al_2O_3 and MgO (inert supports) and active supports which can supply oxygen (e.g. TiO_2. Acidic supports, such as zeolites and zeotypes, tend to have a very low activation for CO oxidation. In addition, excessive Al may collapse the ordered microporous structure to some extent, resulting in a lower BET surface area as discussed in Section 3.5. This may have led to some blockage of the nanochannels. According to Chiang *et al.*[44] zeotypes with a Si/Al ratio > 20 tend to block the pores of the zeotypic material, thus decreasing the catalytic activity.

Chloride is, as mentioned in Section 2.2.5 a well known catalyst poison and is known to poison the catalytic performance of gold catalysts for CO oxidation.[47] Chloride weakens the absorption of O_2 and lowers the stability of the CO-O_2 intermediate complex. The Au(III)/2 complex, used as the precursor, was thoroughly washed with a supersaturated ammonium nitrate solution. However, it is still possible that the samples contained some traces of chloride as it was impossible to detect the chloride contents by ICP-MS.

Other factors such as the pre-treatment temperature and the preparation technique may have influenced the results to some extent. By raising the pre-treatment temperature from 150 °C to 300 °C, some conversion way shown by Au(III)/2:HY.

For Au(III)/2:SAPO-34 an increase in the pre-treatment temperature could lead to conversion as the EXAFS refinement confirmed cationic gold still present in the sample at 450 °C. By pre-treating the sample as higher temperatures (preferably above 500 °C), all the gold cations might be reduced, hence leading to catalytic activity.

As mentioned in Section 2.2.5 deposition-precipitation (DP) and incipient wetness impregnation (IWI) are known to the be the most used preparation techniques for Au catalysts for CO oxidation. These techniques are excellent for dispersing gold on a two dimensional surface. However, both HY and SAPO-34 possess a three dimensional structure, hence introducing gold into the structure by these methods instead of the conventional ion-exchange method, would most likely not have increased the gold content to any extent.

Chapter 5

CONCLUSIONS

Introduction of $HAuCl_4$ during synthesis of SAPO-5 led to an incorporation of 0.45 wt% gold in the zeotype framework after calcination. BET surface area measurements and PXRD confirmed no collapse of the zeotypic structure. XAS analysis confirmed an auto reduction of the gold cations. The metallic gold atoms have agglomerated into large gold nanoclusters during the synthesis or the calcination process. The size of these gold nanoclusters were found to be too large with respect to catalytic measurements.

Hydrothermal ion-exchange of the zeolites ZSM-5 and HY with $HAuCl_4$ led to an introduction of 0.33 wt% and 0.24 wt% gold, respectively. BET surface area measurements and XAS analyses confirmed a decrease in the surface area and formation of large gold nanoclusters. However, the gold nanoclusters in HY was found to be smaller than the gold nanoclusters in ZSM-5.

Conventional ion-exchange with Au(III)/1 solution led to an introduction of 0.07 wt% Au into ZSM-5, 0.17 wt% Au into HY and 0.07 wt% Au into SAPO-34. BET surface area measurements revealed a decrease in the surface area for the three samples, however PXRD showed no collapse of the zeotypic structures. XAS analysis confirmed fractions of cationic gold in Au(III)/1:ZSM-5 and Au(III)/1:HY, the fraction being smaller in Au(III)/1:ZSM-5. EXAFS refinements revealed that the gold cations were homogeneously dispersed on the Au(III)/1:SAPO-34 surface.

In-situ studies of Au(III)/1:ZSM-5 and Au(III)/1:HY confirmed a complete reduction of the gold cations at 150 °C in a reducing atmosphere. The reduced gold atoms have most likely agglomerated, thus formed small gold nanoclusters. The gold nanoclusters in ZSM-5 most likely located on the external surface of the zeolite. In zeolite HY, a fraction of the gold nanoclusters are believed to be trapped within the supercages. The remaining fraction is most likely located on the external surface. Both the samples showed some oxidizing capacity in an oxidizing atmosphere. This observation, in addition to detection of small gold nanocluster sizes ($<$ 3 nm) make the samples interesting with respect to the selective catalytic reduction (SCR) of NO and NO_x.

The conventional ion-exchange of SAPO-34 with the Au(III)/2 solution led to introduction of 0.06 wt% gold. The BET surface area measurement a decrease in the surface area to some extent. The in-situ study revealed structural information that truly separated the sample from the others investigated. EXAFS analysis revealed an homogenous dispersion of gold cations on the zeotypic surface throughout the experiment. The hydrogen flow reduced some of the gold cations, the gold atoms are assumed to have agglomerated into small gold nanoclusters. In an oxidizing atmosphere, the gold oxidized, thus reducing NO to N_2O and N_2. The three-dimensional CHA structure is considered to be the size limitating factor with respect to the formation of the small gold nanocluster in the sample. The oxidizing capacity combined with the presence of small gold nanocluster makes Au(III)/2:SAPO-34 a promising catalyst for the selective catalytic reduction (SCR) of NO and NO_x.

The low gold content, combined with the acid support, are assumed to be the main reasons for why Au(III)/1:HY and Au(III)/2:SAPO-34 did not convert carbon monoxide into carbon dioxide during the activity measurements. In addition, chloride is still believed to be present in the sample, thus acting as a catalyst poison and lower the activity of the metallic gold nanoclusters.

Chapter 6

FUTURE WORK

The work of this thesis has included a wide range of techniques for characterization of gold zeotypic materials. Going deeper into all the details of the most interesting features and results has not been possible, but would substantiate the work from this thesis and lead to a more comprehensive understanding of the factors controlling the catalytic activity of gold.

To investigate the size distribution of the gold nanoclusters some additional characterization analyses should be performed;

- Transmission Electron Microscope (TEM) to detect the exact size and shape of the gold nanoclusters
- Small Angle X-ray Scattering (SAXS) to fully determine the size distribution of the gold nanoclusters
- X-ray Absorption Spectroscopy (XAS) measurements of Au(III)/2:ZSM-5 and Au(III)/2:HY to determine whether the Au(III)/2 solution-precursor will increase the fraction of homogeneous dispersed gold cations on the zeolitic surfaces, compared to what detected for the Au(III)/1 solution-precursor

With respect to activation measurements, the samples should be further investigated with respect CO oxidation;

- It is suggested that Au(III)/2:SAPO-34 should be pre-treated at a higher temperature than what included in this thesis. By pre-treating the sample as higher temperatures (preferably above 500 °C), all the gold cations might be reduced, hence leading to catalytic activity.
- Au(III)/1:ZSM-5 was not tested as a catalyst for CO oxidation during the work of this thesis. The gold nanoclusters in the sample are found to be within the appropriate size range, hence the sample may possess some catalytic activity towards CO oxidation.
- A new ion-exchanged Au^{3+}/SAPO-34 sample should be prepared, this time with a higher gold content since this was found to be the inhibited factor. The support has shown itself to be well suited for the formation of small gold nanoclusters, hence a new activity measurement would be of interest.

In addition, activity measurements for the selective catalytic reduction (SCR) of NO_x are suggested;

- Au(III)/2:SAPO-34 has already proven itself to be a promising catalyst for the reduction of NO. It is therefore desirable to test the samples catalytic ability towards selective catalytic reduction of NO_x.
- Au(III)/1:ZSM-5 and Au(III)/1:HY both revealed some oxidizing capacity during the in-situ measurements, thus it is suggested that activity measurements should be carried out on these samples as well.

Bibliography

[1] M. Haruta *et al.* Novel Gold Catalysts for the Oxidation of Carbon-Monoxide at a Temperature far below 0-Degrees-C. *Chemistry Letters*, pages 405–408, 1987.

[2] M. Haruta *et al.* Gold Catalysts prepared by Coprecipitation for Low-Temperature Oxidation of Hydrogen and of Carbon-Monoxide. *Journal of Catalysis*, 115:301–309, 1989.

[3] J.C. Fierro-Gonzalez, Y. Hao, and B. Gates. Gold Nanoclusters Entrapped in the α-Cages of Y Zeolites: Structural Characterization by X-ray Absorption Spectroscopy. *The Journal of Physical Chemistry C*, 111:6645–6651, 2007.

[4] E. Bus, R. Prins, and J.A. van Bokhoven. Time Resolved in-situ XAS Study of the Preparation of Supported Gold Clusters. *Physical Chemistry Chemical Physics*, 9:3312–3320, 2007.

[5] J.T. Miller, A.J. Kropf, Y. Zha, J.R. Regalbuto, L. Delannoy, E. Bus, and J.A. van Bokhoven. The Effect of Gold Particle Size on Au-Au Bond Length and Reactivity toward Oxygen in Supported Catalysts. *Journal of Catalysis*, 240:222–234, 2006.

[6] D.A.H. Cunningham, W. Vogel, H. Kageyama, S. Tsubota, and M. Haruta. The Relationship between the Structure and Activity of Nanometer Size Gold When Supported on $Mg(OH)_2$. *Journal of Catalysis*, 177:1–10, 1998.

[7] R.M. Sanchez, T. Oshima, and M. Haruta. Reduction of Nitrogen Monoxide with Propene in the presence of Oxygen and Moisture over Gold Supported on Metal Oxidese. *Applied Catalysis*, 12:81–93, 1997.

[8] T. Hayashi, K. Tanaka, and M. Haruta. Selective Vapor-Phase Epoxidation of Propylene over Au/TiO_2 Catalysts in the presence of Oxygen and Hydrogen. *Journal of Catalysis*, 178:566–575, 1998.

[9] S. Tsubota, D.A.H. Cunningham, Y. Band, and M. Haruta. Preparation of Nanometer Gold strongly interacted with TiO_2 and the Structure Sensitivity in Low-Temperature Oxidation of CO. *Studies in Surface Science and Catalysis*, 91:227–235, 1995.

[10] N.A. Hodge *et al.* Microstructural Comparison of Calcined and Uncalcined Gold/Iron-Oxide Catalysts for Low-Temperature CO Oxidation. *Catalysis Today*, 72:133–144, 2002.

[11] N. Hammer, I. Kvande, and X. Xu *et al.* $Au\text{-}TiO_2$ Catalysts on Carbon Nanofibres prepared by Deposition-Precipitation and from Colloid Solutions. *Catalysis Today*, 123:245–256, 2007.

[12] N. Hammer, I. Kvande, and D. Chen *et al.* $Au\text{-}TiO_2$ Catalysts stabilised by Carbon Nanofibres. *Catalysis Today*, 122:365–369, 2007.

[13] J.-N. Lin and B.Z. Wan. Effects of Preparation Conditions on Gold/Y-Type Zeolite for CO Oxidation. *Applied Catalysis*, 41:83–95, 2003.

[14] A. Corma. State of the Art and future Challenges of Zeolites as Catalysts. *Journal of Catalysis*, 216:298–312, 2003.

[15] K. Mathisen, G. Nicholson, D, and A.M. Beale *et al.* Comparing Cuapo-5 with Cu : ZSM-5 in the Selective Catalytic Reduction of NOx: An In situ Study. *Journal of Physical Chemistry*, 111:3130–3138, 2007.

[16] K. Mathisen, M. Stockenhuber, and D.G. Nicholson. *In situ* XAS and IR studies on Cu:SAPO-5 and Cu:SAPO-11: the contributory role of monomeric linear copper(i) species in the selective catalytic reduction of NOx by propene. *Physical Chemistry Chemical Physics*, 2009.

[17] M.J. Fay, A. Proctor, and D.P. Hoffmann. Unraveling EXAFS. *Analytical Chemistry*, 60:1225A–1243A, 1988.

[18] J.H. Clark and C.N. Rhodes. *Clean Synthesis using Porous Inorganic Solid Catalysts and Supported Reagents.* Royal Society of Chemistry, 2000.

[19] A. Dyer. *An Introduction to Zeolite Molecular Sieves.* John Wiley, 1988.

[20] K. Byrappa and M. Yoshimura. *Handbook of Hydrothermal Technology - Technology for Crystal Growth and Materials Processing.* William Andrew Publishing/Noyes, 2001.

[21] L.E. Smart and E.A. Moore. *Solid State Chemistry - An Introduction.* CRC Press, 2005.

[22] P. Somasundaran. *Encyclopedia of Surface and Colloid Science.* CRC Press, 2006.

[23] R. Szostak. *Molecular Sieves: Principles of Synthesis and Identification.* Springer, 1998.

[24] N.Y. Chen *et al. Shape Selective Catalysis in Industrial Applications.* CRC Press, 1996.

[25] A. Holmen. *Heterogen Katalyse.* Institutt for kjemisk prosessteknologi, NTNU, 2006.

[26] IZA Synthesis Commission. Database of Zeolite Structures. Available at `http://www.iza-online.org`, February 2009.

[27] S. Bhatia. *Zeolite Catalysis: Principles and Applications.* CRC Press, 1990.

[28] H. Klein, C. Kirschhock, and H. Fuess. Adsorption and Diffusion of Aromatic Hydrocarbons in Zeolite Y by Molecular Mechanics Calculation and X-ray Powder Diffraction. *The Journal of Physical Chemistry*, 98:12345–12360, 1994.

[29] J.A. Rabo. *Zeolite Chemistry and Catalysis.* American Chemical Society, 1976.

[30] H.O. Pastore, S. Coluccia, and L. Marchese. Porous Aluminophosphates: From Molecular Sieves to Designed Acid Catalysts. *Annual Review of Materials Research*, 35:351–395, 2005.

[31] B.M. Lok *et al.* Silicoaluminophosphate Molecular-Sieves - Another new Class of Microporous Crystalline Inorganic Solids. *Journal of the American Chemical Society*, 106:6092–6093, 1984.

[32] J.W. Park, J.Y. Lee, K.S. Kin, S.B. Hong, and G. Seo. Effects of Cage Shape and Size of 8-membered Ring Molecular Sieves on their Deactivation in Methanol-to-Olefin (MTO) Reactions. *Applied Catalysis A:General*, 339:36–44, 2008.

[33] S. Wilson and P. Barger. The Characteristics of SAPO-34 which Influence the Conversion of Methanol to Light Olefins. *Microporous and mesoporous materials*, 29:117–126, 1999.

[34] G.C Bond, C. Louis, and D. Thompson. *Catalysis by Gold (and references therein)*. Imperial College Press, 2006.

[35] J. Guzman and C.G. Gates. Gold Nanoclusters Supported on MgO: Synthesis, Characterization, and Evidence of Au. *NANO Letters*, 1:689–692, 2001.

[36] K. Okumura, K. Yoshino, K. Kato, and M. Niwa. Quick XAFS Studies on the Y-Type Zeolite Supported Au Catalysts for CO-O Reaction. *The Journal of Physical Chemistry*, 109:12380–12386, 2005.

[37] P.P. Edwards and J.M. Thomas. Gold in Metallic Divided States - From Faraday to Day-Present Nanoscience. *Angew. Chem. Int.*, 46:5480–5486, 2007.

[38] T. Biggs *et al.* Webexhibits - causes of color. Available at `http://www.webexhibits.org/causesofcolor/`, April 2009.

[39] J. de Graaf, A.J. van Dillen, K.P. de Jong, and D.C. Koningsberger. Preparation of Highly Dispersed Pt Particles in Zeolite Y with a Narrow Particle Size Distribution: Characterization by Hydrogen Chemisorption, TEM, EXAFS Spectroscopy, and Particle Modeling. *Journal of Catalysis*, 203:307–321, 2001.

[40] M. Haruta. Size- and Support-Dependency in the Catalysis of Gold. *Catalysis Today*, 36:153–166, 1997.

[41] A.A. Herzing, C.J Kiely, A.F. Carley, P. Landon, and G.J. Hutchings. Identification of Active Gold Nanoclusters on Iron Oxide Supports for CO Oxidation. *Science*, 321:1331–1335, 2008.

[42] S. Veprek, D.L. Cocke, S. Kehl, and H.R. Oswald. Mechanism of the Deactivation of Hopcalite Catalysts Studied by XPS, ISS, and Other Techniques. *Journal of Catalysis*, 100:250–263, 1986.

[43] J.M.C. Soares, P. Morrall, A. Crossley, P. Harris, and M. Bowker. Catalytic and Noncatalytic CO Oxidation on Au/TiO_2 Catalysts. *Journal of Catalysis*, 219:17–24, 2003.

[44] C-W. Chiang, A. Wang, and C-Y. Mou. CO Oxidation catalyzed by Gold Nanoparticles confined in Mesoporous Aluminosilicate Al-SBA-15: Pretreatment Methods. *Catalysis Today*, 117:220–227, 2006.

[45] M. Haruta *et al.* Fine Structure of Novel Gold Catalysts Prepared by Coprecipitation. *Studies in Surface Science and Catalysis*, 44:33–42, 1989.

[46] M. Bowker, A. Nuhu, and J. Soares. High Activity Supported Gold Catalysts by Incipient Wetness Impregnation. *Catalysis Today*, 122:245–247, 2007.

[47] I. Dobrosz, K. Jiratova, V. Pitchon, and J.M. Rynkowski. Effect of the Preparation of Supported Gold Particles on the Catalytic Activity in CO Oxidation Reaction. *Journal of Molecular Catalysis. A*, 234:187–197, 2005.

[48] H.-S. Oh, J.H. Yang, C.K. Castello, Y.M. Wang, S.R. Bare, H.H. Kung, and M.C. Kung. Selective Catalytic Oxidation of CO: Effect of Chloride on Supported Au Catalysts. *Journal of Catalysis*, 210:375–386, 2002.

[49] P. Broqvist, L.M. Molia, H. Grönbeck, and B. Hammer. Promoting and Poisoning Effects of Na and Cl Coadsorption on CO Oxidation over MgO-supported Au Nanoparticles. *Journal of Catalysis*, 227:217–226, 2004.

[50] S.T. Daniells, M. Makkee, and J.A. Moulijn. The Effect of High-Temperature Pre-treatment and Water on the Low Temperature CO Oxidation with Au/Fe_2O_3 Catalysts. *Catalysis Letters*, 100:39–47, 2005.

[51] M. Mavrikakis, P. Stoltze, and J.K. Norskov. Making Gold less Noble. *Catalysis Letters*, 64:101–106, 2000.

[52] A.H.S. Kootenaei, M. Kazemeini, and H. Kazemian. Effect of Catalyst Preparation Conditions on Nano-Gold Deposited on ZSM-5 for CO Oxidation. *International Journal of Modern Physics B*, 22:3278–3288, 2008.

[53] G.J. Hutchings. Catalysis by Gold. *Catalysis Today*, 100:55–61, 2005.

[54] N. Lopez and J.K. Nørskov. Catalytic CO Oxidation by a Gold Nanoparticle: A Density Functional Study. *Journal of the American Chemical Society*, 124:11262–11263, 2002.

[55] N. Lopez, T.V.W. Janssens, B.S. Clausen, Y. Xu, M. Mavrikakis, T. Bligaard, and J.K. Nørskov. On the Origin of the Catalytic Activity of Gold Nanoparticles for Low-Temperature CO Oxidation. *Journal of Catalysis*, 223:232–235, 2004.

[56] R. Kohli and K.L. Mittal. *Developments in Surface Contamination and Cleaning - Fundamentals and Applied Aspects*. William Andrew Publishing, 2008.

[57] V.S. Ramachandran and J.J. Beaudoin. *Handbook of Analytical Techniques in Concrete Science and Technology*. William Andrew Publishing/Noyes, 2001.

[58] P. Atkins, T. Overton, J. Rourke, M. Weller, and F. Armstrong. *Inorganic Chemistry*. Oxford University Press, 2006.

[59] D. Stirling. *Sulfur Problem - Cleaning up Industrial Feedstocks*. Royal Society of Chemistry, 2000.

[60] D.C. Koningberger and R. Prins. *X-ray absorption: Principles, Applications, Techniques of EXAFS, SEXAFS and XANES*. John Wiley, 1988.

[61] B.K. Teo. *EXAFS: Basic Principles and Data Analysis.* Springer Verlag, Berlin, 1986.

[62] Y. Iwasawa. *X-ray Absorption Fine Structure for Catalysts and Surfaces.* World Scientific, 1996.

[63] M. Brown, R.E. Peierls, and E.A. Stern. White Line in X-ray Absorption. *Physical Review B*, 15:738–744, 1977.

[64] D.E. Sayers, E.A. Stern, and F.W. Lytle. New Technique for Investigating Noncrystalline Structures - Fourier Analysis of Extended X-ray - Absorption Fine Structure. *Physical Review Letters*, 27:1204–1207, 1971.

[65] E.A. Stern. Theory of the Extended X-ray-Absorption Fine Structure. *Physical Review B*, 10:3027–3037, 1974.

[66] B.K. Teo and P.A. Lee. Ab Initio Calculations of Amplitude and Phase Functions for Extended X-ray Absorption Fine Structure Spectroscopy. *Journal of the American Chemical Society*, 101:2815–2832, 1979.

[67] E.A. Stern, B.A. Bunker, and S.M. Heald. Many-Body Effects on EXAFS Amplitudes. *Bulletin of the American Physical Society*, 25:440, 1980.

[68] ESFR European Synchrotron Radiation Facility. European synchrotron radiation facility, esfr. Available at `http://www.esrf.eu`, April 2009.

[69] U. Johansson, S. Werin, and A. Nyberg. Max-lab. Available at `http://www.maxlab.lu.se`, April 2009.

[70] B. Ravel and M. Newville. Athena, ARTEMIS, HEPHAESTUS: Data Analysis for X-ray Absorption Spectroscopy using IFEFFIT. *Journal of Synchrotron Radiation*, 12:537–541, 2005.

[71] N. Binsted, J.W. Campbell, and P.C Stephenson. *EXCURV98: CCLRC Daresbury Laboratory Computer Program.* SERC Daresbury Program Library, 1998.

[72] M. Newville *et al.* Near-Edge X-ray-Absorption Fine Structure of Pb: A Comparison of Theory and Experiment. *Physical Review B*, 47:14126–14131, 1993.

[73] L.H. Skibsted and J. Bjerrum. Studies on Gold Complexes. I. Robustness, Stability and Acid Dissociation of Tetramminegold(iii) Ion. *Acta Chemica Scandinavica Series A - Physical and Inorganic Chemistry*, A28:740–746, 1974.

[74] Zeolyst International. Zeolyst International. Available at `http://www.zeolyst.com/`, April 2009.

[75] J.W. Yoon, S.H. Jhung, Y.H. Kim, S-E. Park, and J-S. Chang. Selective Crystallization of SAPO-5 and SAPO-34 Molecular Sieves in Alkaline Condition: Effect of Heating Method. *Bulletin of the Korean Chemical Society*, 26:558–562, 2005.

[76] N. Kumar, J.I. Villegas, T. Salmi, D. Yu Murzin, and T. Heikkilä. Isomerization of *n*-butane to isobutane over Pt-SAPO-5, SAPO-5, Pt-H-mordenite and H-mordenite catalysts. *Catalysis Today*, 100:355–361, 2005.

[77] C-W. Chiang, A. Wand, B-Z. Wan, and C-Y. Mou. High Catalytic Activity for CO Oxidation of Gold Nanoparticles Confined in Acidic Support Al-SBA-15 at Low Temperatures. *The Journal of Physical Chemistry B*, 109:18042–18047, 2005.

[78] J. Guzman, S. Kuba, J.C. Fierro-Gonzalez, and B.C. Gates. Formation of Gold Clusters on TiO_2 from adsorbed $Au(CH_3)_2(C_5H_7O_2)$: Charaterization by X-ray Absorption Spectroscopy. *Catalysis Letters*, 1–2:77–86, 2004.

[79] J.C. Bailar, H.J. Emelèus, R. Nyholm, and A.F. Trotman-Dickenson. *Comprehensive Inorganic Chemistry, Volume 3*. Pergamon Press Ltd., 1973.

[80] A. Balerna *et al.* Extended X-ray Absorption Fine-Structure and Near-Edge-Structure Studies on Evaporated Small Clusters of Au. *Physical Review B*, 31:5058–5065, 1985.

[81] G. Riahi, D. Guillemot, M. Polisset-Thfoin, A.A. Khodadadi, and J. Fraissard. Preparation, Characterization and Catalytic Activity of Gold-based Nanoparticles on HY Zeolites. *Catalysis Today*, 72:115–121, 2002.

Appendix A

Calculation of cluster sizes from the Scherrer equation

- Calculation of cluster size in as-synthesized AuSAPO-5 using equation 2.6:

$$d = \frac{0.9 \cdot 1.5406nm}{0.276 \cos(\frac{44.417}{2})} = 5.426nm \tag{A.1}$$

- Calculation of cluster size in calcined AuSAPO-5 using equation 2.6:

$$d = \frac{0.9 \cdot 1.5406nm}{0.170 \cos(\frac{44.591}{2})} = 8.815nm \tag{A.2}$$

Appendix B

Results for linear combination

Table B.1 represents the result of the normalized Au L_{III}-edge XANES linear combined with the normalized XANES spectra for the Au foil (Au(0)), Au(I)Cl (Au(I)) and Tetraaminegold(III) nitrate (Au(III)).

Table B.1: Linear combination of Au zeotypic systems at room temperature

Sample	**Au(0)**	**Au(I)**	**Au(III)**	**R-factor**(10^{-4})
AuSAPO-5 as-prep.	0.966(1)	0.021(1)	0.013(1)	0.04
AuSAPO-5 calc.	1(0)	0(0)	0(0)	2.04
Au:ZSM-5 as-prep.	1(0)	0(0)	0(0)	3.90
Au:HY as-prep.	0.829(1)	0(0)	0.171(1)	7.39
Au(III)/1:ZSM-5 as-prep.	0.50(2)	0.15(3)	0.35(7)	2.11
Au(III)/1:HY as-prep.	0.40(1)	0(0)	0.60(1)	3.70
Au(III)/1:SAPO-34 as-prep.	0(0)	0.224(1)	0.776(1)	3.65
Au(III)/2:SAPO-34 as-prep.	0(0)	0(0)	1(0)	25.02

The Tables B.2, B.3 and B.4 represents the results for the linear combination of Au(III)/1:ZSM-5, Au(III)/1:HY and Au(III)/2:SAPO-34 at evaluated temperatures and atmospheres.

Table B.2: Linear combination of Au(III)/1:ZSM-5 at evaluated temperatures and atmospheres

Temp. (°C)	**Atmosphere**	**Au(0)**	**Au(I)**	**Au(III)**	**R-factor**(10^{-4})
RT	Air	0.50(2)	0.15(3)	0.35(1)	2.11
150	100% He	0.61(4)	0.23(4)	0.16(1)	4.98
150	5% H_2 in He	0.68(4)	0.21(5)	0.11(1)	7.11
350	5% H_2 in He	0.65(4)	0.26(5)	0.09(1)	7.00
450	5% H_2 in He	0.67(5)	0.25(5)	0.08(1)	7.96
RT	0.6% NO in He	0.85(2)	0.06(2)	0.09(1)	7.08

Table B.3: Linear combination of Au(III)/1:HY at evaluated temperatures and atmospheres

Temp. (°C)	**Atmosphere**	**Au(0)**	**Au(I)**	**Au(III)**	**R-factor**(10^{-4})
RT	Air	0.40(1)	0(0)	0.60(1)	3.70
150	100% He	0.51(4)	0.16(4)	0.33(1)	4.43
150	5% H_2 in He	0.53(3)	0.28(3)	0.16(3)	3.85
250	5% H_2 in He	0.61(4)	0.30(4)	0.09(1)	6.61
350	5% H_2 in He	0.61(3)	0.30(5)	0.09(1)	9.90
450	5% H_2 in He	0.62(3)	0.32(4)	0.06(1)	4.26
RT	0.6% NO in He	0.69(4)	0.21(4)	0.10(1)	7.04

Table B.4: Linear combination of Au(III)/2:SAPO-34 at evaluated temperatures and atmospheres

Temp. (°C)	**Atmosphere**	**Au(0)**	**Au(I)**	**Au(III)**	**R-factor**(10^{-4})
RT	Air	0(0)	0(0)	1(0)	25.02
150	100% He	0.361(7)	0.025(3)	0.614(8)	4.30
150	5% H_2 in He	0.31(2)	0.35(3)	0.34(3)	2.17
250	5% H_2 in He	0.35(2)	0.57(2)	0.08(3)	3.13
350	5% H_2 in He	0.52(3)	0.43(2)	0.05(3)	5.16
450	5% H_2 in He	0.47(3)	0.46(3)	0.07(8)	5.82
RT	0.6% NO in He	0.61(2)	0.30(2)	0.09(3)	3.64